Structural performance assessment of RC members by incorporating the spatial steel corrosion

鉄筋腐食の空間変動性を考慮したRC部材の構造性能評価

February 2018

Sopokhem LIM

リム　ソーポーケム

Structural performance assessment of RC members by incorporating the spatial steel corrosion

鉄筋腐食の空間変動性を考慮したRC部材の構造性能評価

February 2018

Waseda University

Graduate School of Creative Science and Engineering

Department of Civil and Environmental Engineering,

Research on Concrete Structure

Sopokhem LIM

リム　ソーポーケム

Acknowledgement

laboratory staff in Material Engineering laboratory for their kind supports during the concrete experimental tests.

Last but not least, I would love to say a million thanks to my beloved wife Sophy as well as my and her families to whom I am in debt for their constant care and motivation during my busy studying time in Japan.

Sopokhem LIM

Summary

Steel corrosion is well recognized as a dominant cause of deteriorating RC structures. It represents enormous economic loss to nations around the world for the cost of maintenance, repair, and replacement of the corroded structures. Therefore, the establishment of reliable models for the long-term structural performance assessment of corroding RC structures is important to assist the government and structure asset owners in decision-making on remedial repair and maintenance action plan to extend their service life and prevent the economic loss.

Finite element and probabilistic approaches have been used for the structural performance assessment of corroding RC structures. However, the difficulty in quantifying the spatial steel corrosion along the RC structures has been reported as the primary challenge in conducting the computational methods more objectively and precisely. In addition to improving computation methods, it is more important to adequately assess and incorporate the level and location of reinforcement corrosion into the computational methods in order to obtain more objective prediction results. To model the spatial steel corrosion, there is a need to experimentally investigate how the steel corrosion increases or changes at different corrosion times. This dissertation aims to experimentally study the spatial growth of steel corrosion in RC members using X-ray and digital image processing technique and develop a procedure to assess the structural performance of corroding RC structures by incorporating the spatial steel corrosion. It is composed of six chapters.

Chapter 1 explains the research background and motivation for the study of spatial variability associated with steel corrosion in order to evaluate the structural performance of corroding RC structures, and some specific objectives of the research are provided.

Chapter 2 provides systematic literature review on the fundamental concepts of steel corrosion in RC structures, effects of corrosion damages on the RC materials and structural performance, and recent trend of experimental studies on the spatial steel corrosion of corrosion-accelerated beams by means of destructive and non-destructive methods.

Chapter 3 describes the experimental tests and procedure to estimate the spatial steel corrosion and corrosion crack width using digital image processing technique. Corrosion of the embedded longitudinal rebar in the RC beams was accelerated via the electrochemical technique. At specific time intervals, the crack widths were recorded by taking photos of surface cracking on the bottom of the beams. X-ray radiography was performed once before the steel corrosion initiated and several times during the corrosion process to capture the non-corroded and corroded rebars embedded in the RC beam from different viewing angles. The X-ray images of steel rebar and photos of cracking were used in the digital image processing to estimate the steel weight loss and crack width per 5 mm along the RC beam for the total length of 840 mm.

Chapter 4 reports and discusses the key findings of experimental results. The estimated rebar weight loss calculated using the digital image analysis was found to be only 3% higher than that of the actual measured steel weight loss. This demonstrated the good accuracy of the present technique for investigating the spatial growth of steel corrosion. The distributions of the steel weight loss and crack width are spatially non-uniform, and their degree of non-uniformity significantly increases with the global mean steel weight loss (MRw) and corrosion cracking (MCw). Nevertheless, there also appears a consistent trend of the erratic shapes of spatial steel corrosion as the values of MRw exceed 5%. The effect of W/C ratio on the increased steel weight loss is not obvious. Meanwhile, the crack width of the specimens with low W/C ratios increased faster than those with high W/C ratios. The crack width and steel corrosion of the specimen without

stirrups increased more quickly than those of specimens with stirrups. For a small variability in the steel weight loss (i.e., a standard deviation below 4.3%), the mean steel weight loss has a dominant effect on the loading capacity of the corroded beams. As the dispersion in the steel corrosion increases, the influence of the pitting corrosion on the loading capacity becomes more significant than the mean steel weight loss.

Chapter 5 presents finite element method and probabilistic approach used to evaluate the structural performance of corroded RC members. For the finite element method, the effects of two different inputs (i.e., uniform and non-uniform cross-sections along the reinforcement) on the computational accuracy were studied. For the probabilistic methods, the Gumbel statistic of the maximum steel weigh loss ratios per 50-mm-long rebar was established. The relationships between the Gumbel parameters and global mean steel weight loss are then developed; and an example is illustrated for the application of Gumble statistics of the maximum of steel weigh loss ratios to study the effects of the spatial and non-spatial steel corrosion on the failure probability of a corroded RC beam under flexure. Both of the results from FE and probabilistic methods indicate that an assumption of uniform steel cross-section loss over the RC beam provides an overestimation of structural performance of corroding RC structures in comparison to the other assumption with non-uniform cross-section.

Chapter 6 provides the concluding remarks and the limitations to be explored in the future works. The experimental data of spatial steel corrosion is very valuable and important since it provides the statistical data for facilitating the life-cycle assessment and management of deteriorated RC structures. The experimental data of steel weight loss was also used in the FE method to study the effects of two different inputs (i.e., uniform and non-uniform cross-sections) on its accuracy. Moreover, in an illustrative example, the relationships between Gumbel parameters and global mean steel weight loss has been incorporated into a probabilistic model to study the effects of non-spatial and spatial steel

corrosion on the reliability assessment of corroding RC structures. Both the FE and probabilistic methods suggest an assumption of the uniform steel corrosion is not conservative; it is necessary to consider the spatial steel corrosion when evaluating the structural performance of corrosion-affected RC structures. The limitations and future works are also given herein for further improvements. The RC specimens shall be reinforced with multiple rebars to study the effects of the potentials of neighboring bars on other rebars. The accelerated corrosion test shall be conducted using smaller current densities than the present value of 1000 $\mu A/cm^2$ to study the effects of different current densities on spatial variability of steel weight loss. Constitutive model associated with the bond behavior in the FE method needs to be improved to simulate bond deterioration effect more precisely. Moreover, the method of integrated approach using the FE and probabilistic method might be a better option for considering the corrosion effects on bond performance and material properties of concrete on the long-term structural performance assessment of corroding RC structures.

List of Figures

List of Tables

Table of Contents

Chapter 1: Introduction

1.1 Background and motivation of research

Since the early twentieth century, reinforced concrete (RC) has been used all over the world for a wide variety of structures such as residential and industrial buildings, transportation infrastructures (e.g., bridges, tunnels, and high ways), water system and retaining structures (e.g., water pipe lines, reservoir tanks, and irrigation dams), and offshore structures (e.g., harbors, light houses, and offshore platforms). Due to various applications of RC structures, they are exposed to different environments, some of which can be severe such as marine environments, intensified industrial zones, and other severe weathering or natural-hazard areas. Initially, it was believed reinforced concrete was made of such durable materials (i.e., concrete and steel reinforcement) that RC structures would perform their functions well under various conditions of environmental exposure. However, from the second half of the twentieth century, there has been increasing deterioration and durability problems of RC structures, and their service life and safety are notably decreased primarily due to reinforcement corrosion.

Presently, steel corrosion attracts considerable attentions worldwide due to the tremendous economic loss it has brought upon all nations. Through times, corrosion inflicts damages on RC structures (e.g., concrete cover cracking and spalling) and leads to decrease in performance and safety, which demands costly maintenance or replacement action plans. In the United States, about 15% of the total 586,000 highway bridges in 1997 was categorized as structurally deficient primarily due to steel corrosion; and the annual direct cost of corrosion for the bridges was estimated to be $8.3 billion, according to the Federal Highway Administration, FHWA (2002). In 2012, FHWA estimates that the U.S. government is required to increase their annual spending from the $12.8 to $20.5 billion in order to eliminate the structurally deficient bridge backlog across the U.S. by

2028 (ASCE report card, 2013). Meanwhile, the corrosion cost of bridges in Japan in 1997 was estimated to be JYP 34.71 billion according to Committee on cost of corrosion in Japan (1997). In 2004, the annual cost of maintenance, management, renewal of public infrastructure and restoration from natural disasters in Japan rose to JPY 5 trillion, as reported in Watanabe et al. (2014).

Therefore, the establishment of a reliable model to assess the performance of corrosion-affected RC structures is an important task for structural engineers and researchers in assisting the government, infrastructure asset owners, and occupants in decision-making on remedial repair and maintenance action plan to extend their service life and prevent considerable economic loss. The deterioration process of steel corrosion that results in performance degradation of RC structures is a complex phenomenon. It involves multiple main parameters (i.e., the loss of concrete-bond interface and reductions in geometry and mechanical properties of concrete and reinforcement). Moreover, some of these parameters also have coupling of single effects (i.e., the coupling effect of the reduced steel cross-section and concrete-steel bond as reported by Castel et al. (2000a) and (2000b). Therefore, the performance assessment of corrosion-affected RC structures demands for a numerical analysis that can consider the damage level of rebar and concrete, and their interactions.

Recently, the finite element (FE) analysis has been employed to assess the effects of corrosion damage on the structural performance of corroded RC members, and its validation was also verified by comparing the numerical results to those of experimental test (e.g., Kallias and Rafiq, 2010; Coronelli and Gambarova, 2004; Lee et al. 1999). Despite of the differences in FE modelling and material constitutive used, these studies focus on the damages as reductions in the effective material properties and geometry of the RC members by modifying the geometry of the steel and concrete elements and the constitutive laws of steel, concrete, and their bond interface. However, Coronelli and

Gambarova (2004) highlighted one of the main challenges is the difficulty in quantifying of steel cross-section loss along the length of RC member which serves as an important parameter for modeling local damages on steel and concrete as well as their interaction. In addition to the improved constitutive models, Akiyama et al. (2014) and Shimomura et al. (2011) suggest the more important tasks in numerical modelling of corroding structures are how to accurately estimate location and level of reinforcement corrosion and how to adequately represent their damages as the input data in the FE models. Hence, the location and degree of reinforcement corrosion of the corroded RC structures shall be adequately evaluated or estimated if their performance is to be reliably assessed by the numerical methods.

Moreover, the probabilistic method has been widely used to assess the long-term performance of corrosion-affected RC structures (Marsh and Frangopol, 2008; Mori and Ellingwood, 1993; Stewart and Mullard, 2007). Stewart (2004) emphasizes it is necessary to consider the spatial variability of steel corrosion in the probabilistic models. Ignoring the spatial variability of corrosion leads to an error of failure probability. However, the limited experimental data on the evaluation of the spatial variability in steel weight loss through the corrosion time has been reported to hinder the improvement of the accuracy of the prediction models (Akiyama and Frangopol, 2014; Akiyama et al., 2010). The scarcity of experimental data is due to the difficulty in continuously observing the non-uniform spatial corrosion of steel weight loss during various stages of corrosion.

As stated above, it is essential to assess the spatial variability of steel corrosion along the corroded RC structures for their structural performance evaluation. However, in practice, it is very difficult to assess adequate data of steel corrosion from the real RC structures. Corrosion of steel reinforcements is not uniform over the RC structures; it is found to be varied through time and space due to various factors that are hardly controlled including the variability in material properties of concrete, workmanships, exposure

conditions, and concrete covers (Fazio and Mirza, 1999; Akiyama et al. 2017). Consequently, it is subjective to extract or assess only some samples of corroded bars at particular locations for the inspection data to best represent the spatial variability associated steel corrosion for the whole large-scale structure.

Hence, it is anticipated that the data of spatial steel corrosion obtained from experimental studies of corrosion-accelerated RC members in the laboratories can be used as complimentary data to that of in-situ inspection to help improve the degree of accuracy in estimating the spatial variability associated with steel corrosion in the RC structures. This can provide better results of spatial steel corrosion estimation for assessing the remaining service life of existing corroded RC structures. In the absence of inspection data, the statistical data from the experiment can also be incorporated with numerical and probabilistic models to predict the long-term performance of new-built structures in an anticipated aggressive marine environment with some proper assumptions.

To achieve this goal, there is a need to experimentally investigate how the steel corrosion increases or changes at different corrosion times. In the literatures, several researches have been conducted to investigate the spatial variability associated with steel corrosion for attempts to model steel corrosion using statistical data from experimental tests. The destructive method is commonly used by breaking some corroded specimens at different corrosion times and retrieve the corroded rebar samples for measuring their weights (e.g., Kashani et al. 2013a; Vidal et al. 2004) or for scanning their morphology using an advanced 3D optical scanning device (e.g., Kashani et al. 2013b). However, since these methods require some different specimens to be demolished at various corrosion times, they can suffer from errors due to the difficulty in making the same experimental conditions repeatable and other uncertainties (e.g., different corrosion cracking patterns and locations of steel corrosion).

To avoid the above-mentioned problems, a monitoring method of steel corrosion

using a non-destructive X-ray technique can be a better option since it enables a continuous study of the spatial growth of steel corrosion throughout the corrosion process. Akiyama et al. (2013) employed the X-ray and digital image processing techniques to study and quantify the spatial variability of steel weight losses along the corroded bars inside the RC specimens. The merits of this method are of great interests since the evolution of spatial distribution of steel corrosion and its relationship with the corrosion cracking can be studied at various corrosion times and also a good accuracy of estimated steel weight loss can be obtained. In this research, a similar method to that of Akiyama et al. (2013) is used for the investigation and estimation of the spatial growth of steel corrosion of corroded beams at different corrosion process. Larger specimens with longer length of corroded steel bars are used in this study. Moreover, by using a new upgraded X-ray apparatus and image intensifier, X-ray photograms can be acquired with a higher resolution that can detect corrosion products. The more advanced digital image analyzer also improves the accuracy of estimating the steel weight loss. As a result, better estimated results of steel weight loss can be obtained.

1.2 Objectives of the research

The objectives of this research are to:

(a) Establish a procedure to visualize and estimate the spatial variability associated with steel weight loss using X-ray and digital image processing;

(b) experimentally investigate the effects of water-to-cement ratios and stirrups on the spatial variability associated with the steel corrosion and crack width;

(c) experimentally study the effects of spatial variability associated with steel corrosion on the structural behavior of corroded RC beams;

(d) establish a procedure to assess their deteriorated structural performances using experimental data and FE analysis;

(e) develop the Gumbel statistics of extreme values using the experimental data of steel weight loss to model the spatial steel corrosion;

(f) and establish a probabilistic method to evaluate the effect of spatial steel corrosion on structural reliability of corroded RC beams using Gumbel statistics of extreme values.

In the experimental section, the spatial variability of the steel weight loss was quantified using X-ray and digital image processing techniques (Lim et al. 2017). In the FE method, the experimental data of the steel weight loss is used to model the residual geometry of the reinforcement, reduced concrete strength, and deteriorated bond-slip relations, and the effect of modeling on the steel weight loss distribution of longitudinal rebar over the RC beam (i.e., non-uniform or uniform distribution) on the computational accuracy of the FE analysis is investigated (Lim et al. 2016). The accuracy of the FE model is also verified by comparing the numerical results to those measured in the experimental test. Furthermore, this research also presents a method to develop the Gumbel distribution parameters for a maximum steel weight loss ratio. The relationship between the Gumbel distribution parameters and corrosion amounts is also established. This relationship can be incorporated within a probabilistic model to assess the long-term performance of corroded RC structures. An illustrative example is provided for application of Gumble statistic of maximum steel weight loss ratio in order to assess a long-term performance of a corroded RC beam. The data of the spatial variability associated with the steel corrosion that is obtained from this experiment will contribute to enhancing the accuracy of life-cycle assessment of aging RC structures in an aggressive environment (Frangopol et al., 2011; Akiyama et al., 2016).

Chapter 2: Literature review

2.1 Fundamental concepts of steel corrosion

Corrosion process of steel in concrete is dynamic and complex. It involves the penetration and concentration of aggressive iron or gas (i.e., chloride from sea water or deicing salts and carbon dioxide from atmosphere) into the concrete medium and gradually causes corrosion damages on steel reinforcing bar in terms of cross-section loss. However, it is difficult to imagine under what mechanisms the aggressive agents can penetrate into a dense barrier of concrete cover and cause corrosion at the depth of rebars. In order to comprehend the corrosion phenomena, it is necessary to have a basic understanding on the properties of RC materials, steel reinforcement and concrete (especially microstructure of concrete which plays an important role in determining its mechanical properties and durability including permeability, diffusivity, and transportation of aggressive liquids and gas).

2.1.1 Steel reinforcement

Steel is an alloy which is mainly composed of iron and small percentage of other chemical elements which includes carbon. Carbon is the most important element. Increasing the carbon content increases the strength and hardness, but decreases the toughness and ductility of steel. The other chemical components are manganese, silicon, copper, chromium, columbium, nickel, phosphorus, aluminum etc. Structural steels may be classified as carbon steel, high-strength low-alloy steel, and alloy steel (Smith 1996).

Carbon steel contains maximum percentage of elements other than iron such as 1.7% carbon, 1.65% manganese, 0.60% silicon, and 0.60% copper. Carbon steels are divided into four categories: (1) low carbon (less than 0.15%); (2) mild carbon (0.15% ~ 0.29%); (3) medium carbon (0.30% ~ 0.59%); and (4) high carbon (0.6% ~ 1.70%) (Smith

1996). Mild carbon steel, also known as mild steel, is the most common type of steel used in building construction which has a yield point of 250MPa. High-strength low-alloy steels have a distinct yield point ranging from 275 to 485 MPa. Alloy elements such as chromium, columbium, copper, manganese, molybdenum, nickel, phosphorus, vanadium, and zirconium are added to improve some of the mechanical properties of steel. Alloy steels do not have a distinct yield point. Their yield strength is defined as the stress at an offset strain of 0.002 with yield strengths ranging from 550 to 750 MPa. The high-strength low-alloy and alloy steels generally used for constructing bridges (Kanno 2016). Fig. 1 represents the typical stress-strain relationships for different types of steel.
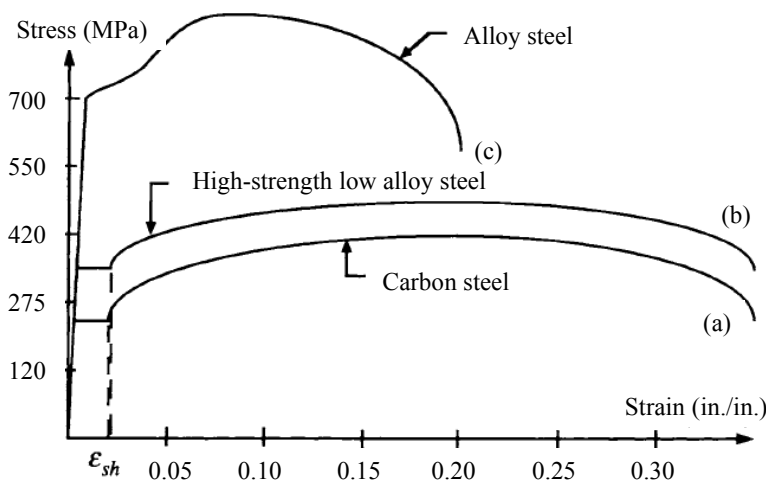
Fig. 1 Typical Stress-Strain curves for steel (Smith 1996).

In nature, iron or steel does not exist; it is originally found in terms of iron ore in a stable state such as Fe_3O_4 and Fe_2O_3. In the ironmaking process, a large amount of heating energy is needed to smelt iron from iron ore. When subjected oxygen and water in the atmosphere, iron or steel that is a production material tends to convert itself back to the original state through an electrochemical process by passing electrons and producing rust such as oxides or hydroxides. In nature, this conversion process of iron to its original state is well known as metallic or steel corrosion (Angst, 2011).

2.1.2 Concrete and its microstructure

Concrete is a composite material principally made of aggregates, portland or blended cement, and water, and possibly contain other cementitious materials and/or chemical admixtures (ACI 211.1-91, 2002). The most important constituent of concrete is cement binder, commonly portland cement. According to Mehta and Monteiro (2006), portland cement is produced by pulverizing a clinker with a small amount of calcium sulfate. The clinker is a heterogeneous mixture of various compounds that is made by reactions among calcium oxide CaO (customarily denoted as C in cement chemistry) and silica SiO_2 (S), alumina Al_2O_3 (A), and iron oxide Fe_2O_3 (F) under high temperature. Portland cement is composed of four principal clinker compounds: $3CaO•SiO_2$ (denoted as C_3S in cement chemistry), $2CaO•SiO_2$ (C_2S), $3CaO•Al_2O_3$ (C_3A), and $4CaO•Al_2O_3•Fe_2O_3$ (C_4AF). During the concrete mixing, when portland cement comes into contacts with water, its constituents have hydration reactions with water and result in a hydrated cement paste which cohesively bind the aggregate particles. Aggregates (sand and stone) of different sizes and shapes suspended in the glue-like cement paste renders this composite with dimensional stability, strength, and cost efficiency.

On a polished section of concrete, without any eye-aided instrument, one can identify only two phases of concrete from its macrostructure: aggregate (scattering of various shapes and sizes of aggregate particles) and hydrated cement paste. However, the studies on macrostructure of concrete are limited in providing insufficient responses to some durability and deterioration problems of concrete which is relevant to steel corrosion aspect such as permeability (internal porous structures), changes in internal structure due to chemical attacks and reactions (hydration reaction), transportation of aggressive liquids or gases (absorption and diffusion of concrete) and others. In responses to the above-mentioned durability and deterioration problems of concrete, the studies on the microstructure of concrete (Mehta and Monteiro, 2006; Scrivener, 2004; Diamond,

2004; Ollivier et al. 1995) provide more comprehensive explanations. On the level of microstructure, concrete is divided into three principal phases: aggregate, cement paste, and the interfacial transition zone between them.

Solids of hydrated cement paste: solids of cement paste are the hydrated cement products of the hydration reactions between cement and water. Among the hydration reactions, the most important ones are those involving the conversion of C_3S and C_2S into a not-well-defined C-S-H gel (calcium silicate hydrate) and portlandite crystals (calcium hydroxides, CH). In a completely hydrated cement paste, the solid volume of hydrated cement paste is filled up by C-S-H gel of 50% ~ 60%, calcium hydroxide of 20% ~ 25%, calcium sulfoaluminates hydrates of 15% ~ 20%, and other unhydrated clinker grains (Mehta and Monteiro, 2006). Since C-S-H gel and calcium hydroxide occupied most volume of cement paste, they are the two important phases determining the strength properties of the cement paste.

Porous structure (voids of hydrated cement paste): in addition to solids of hydrated products, cement paste is also composed of a few types of void. According to Mehta and Monteiro (2006), the smallest voids in the hydrated cement paste are interlayer spaces or gel pores of C-S-H structure since C-H-S is an ill-defined compound with morphology varying from poorly crystalline fibers to reticular network. Another type is called capillary void that represents the space initially occupied by water but not filled up by hydrated cement products. When portland cement is blended with water, its compounds undergo a sequence of hydration reactions which result in increasing hydrated products of cement to gradually fill up the space initially occupied by water. Since the water is either evaporated or consumed in hydration reactions, hydrated cement products
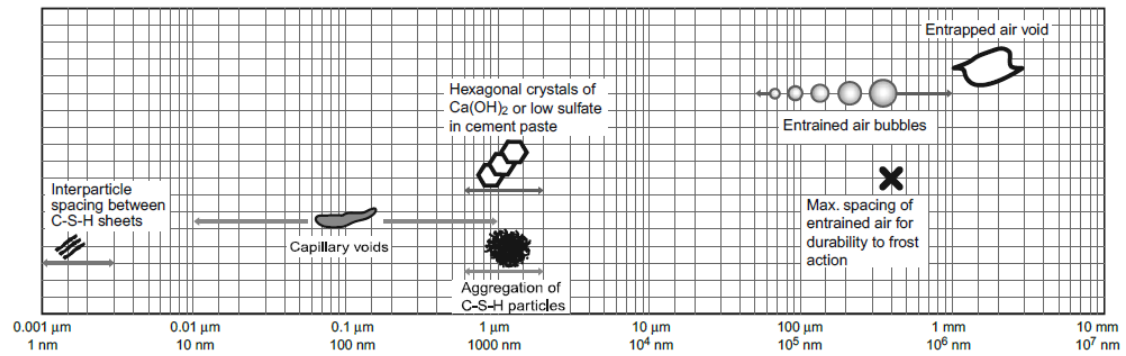
Fig. 2 Size of solids and voids in a hydrated cement paste (Mehta and Monteiro, 2006).

basically have a volume smaller than the substances before hydration. Eventually, the space of water can be completely filled up and capillary voids remain. Moreover, the cement paste also contains unintentionally entrapped air voids during concrete mixing or incomplete compaction and possibly the other intentionally entrained air voids for freeze-thaw resistance. Fig. 2 illustrates the dimension of pore and solids in the hydrated cement paste. The interlayer space of C-S-H structure ranges from 5 to 25 Å (1 Ångström = 0.1 nm). On the other hand, the capillary voids have irregular shapes and a wide range of size from 10 nm to 1 μm since their sizes depend on water-to-cement ratios and degree of hydration, see Figs. 3(a) and (b). Entrapped air voids can be as large as a few millimeters while entrained air voids usually range from 50 to 200 μm. It is worth noting that the pore size distribution is a better indicator for determining the characteristics of a hydrated cement paste. The interspace layer of C-S-H structure is too small to have an effect on strength and permeability of the paste but might contribute to the drying shrinkage and creep. For capillary voids, the size of voids larger than 50 nm probably have more influences on the strength and impermeability of the hardened cement paste; however, the smaller voids than 50 nm can have more adverse effects on drying shrinkage and creep.

Water in cement paste: According to Mehta and Monteiro (2006), depending on the pore structure of a cement paste and humidity in the environment, water can
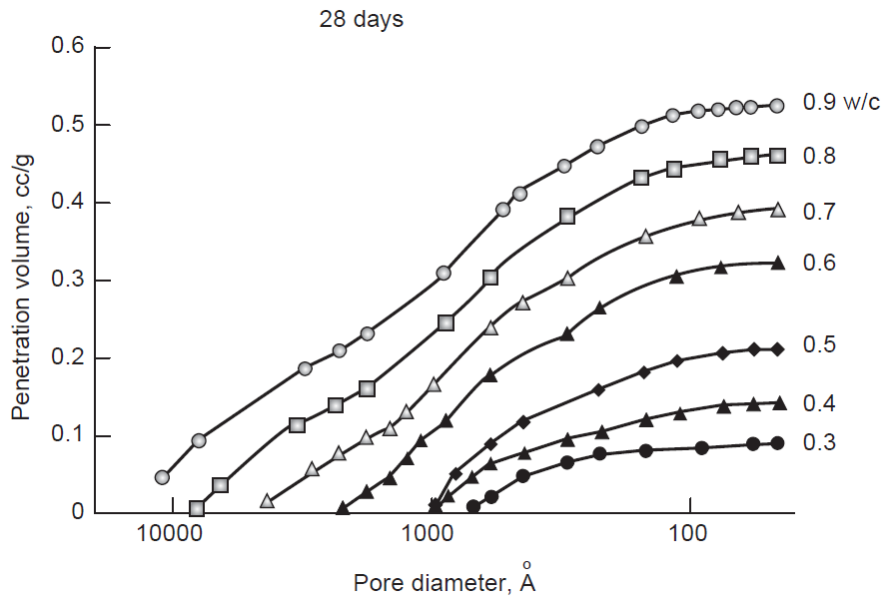
(a) Effects of W/C ratios on the distribution of pore diameters
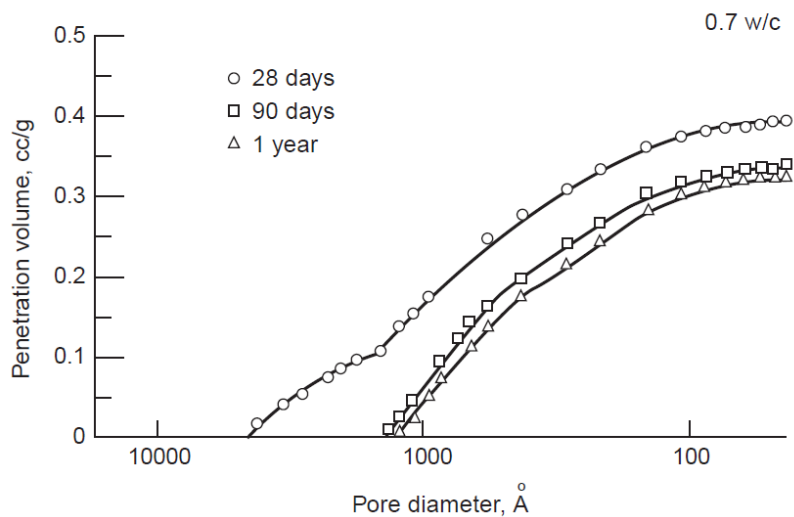
(b) Effects of the age (degree) of hydration on the distribution of pore diameters.

Fig. 3 (a) effects of W/C ratios and (b) effects of the age (degree) of hydration on the size distribution (Mehta and Monteiro, 2006).

manifest itself in the paste in different forms. Types of water in cement paste are classified via the degree of difficulty at which it can be removed from the paste. Capillary water is the water in capillary voids in the cement paste. The removal of water in capillary voids larger than 0.05 μm (i.e., free water) does not lead to any changing volume; however, the removal of water in small capillary voids ranging from (5 to 0.05 nm) might lead to

12

shrinkage of cement paste. Another category of water in cement paste is called absorbed water that is physically absorbed onto the surface of solids by attractive forces. Its large amount can be lost when cement paste is dried to 30 percent relative humidity, causing shrinkage of cement paste. Another form of water is the interlayer water contains in C-H-S gel which can be only lost due to strong dry below 11 percent relative humidity. Lastly, chemically combined water is an integral part of the microstructure of various cement hydration products. It cannot be removed from the cement paste by drying but by the hydrates decomposed on heating.

Interface transition zone of concrete: Unlike the plain cement paste, mortar and concrete have aggregates. The presence of aggregates makes a few significant differences and produce a so-called interfacial transition zone between aggregate and the bulk hydrated cement paste as indicated in Fig4(a). Firstly, due to wall effects of large aggregates, the spatial distribution of cement particles might become more dispersed at local boundaries closed to aggregate particles (Ollivier et al. 1995; Scrivener, 2004). With respect to this behavior, it can be seen from Fig.4(b) that there is an interfacial transition zone which is represented by the line appear after the coarse aggregate (in the left side of the image), and it has more porosity comparing the bulk cement paste in the further right part of the image. This might be inferred that, after the casting the concrete, there was a higher water- to-cement ratio (more dispersed cement grains with so much water) in the region of ITZ (Secrivener, 2004). Secondly, aggregates introduce a high level of heterogeneity of cement particles since it disrupts the pack of cement grains. There is not always ITZ appearing around the boundary of aggregates; there is a large variation of microstructure in ITZ. It is evident that, during the concrete compacting, a higher water-to-cement ratio will move up and attach to the underside of aggregates. This creates a micro bleeding or ITZ at the bottom region of the aggregate rather than on the top. Since ITZ has more volume and bigger size of voids than aggregates and the bulk cement paste,
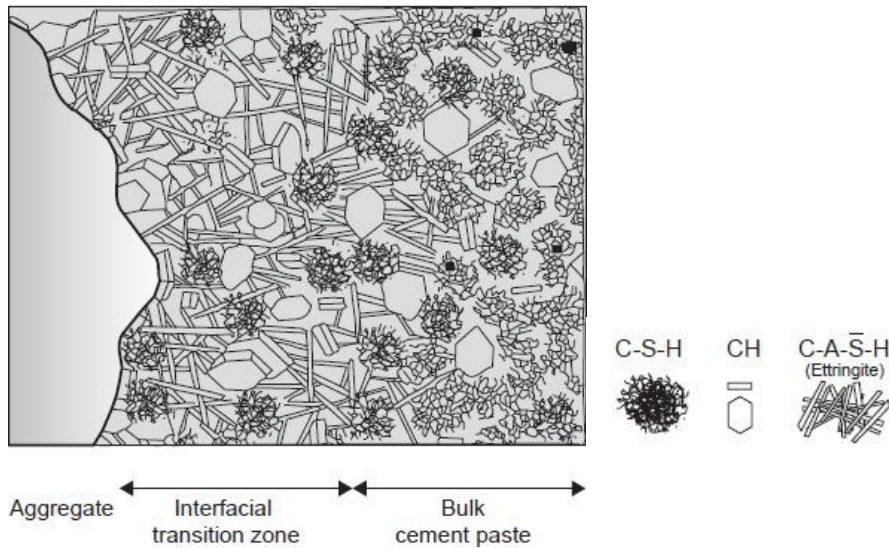
(a) Diagram representing the interfacial transition zone and bulk cement paste of concrete (Mehta and Monteiro, 2006)
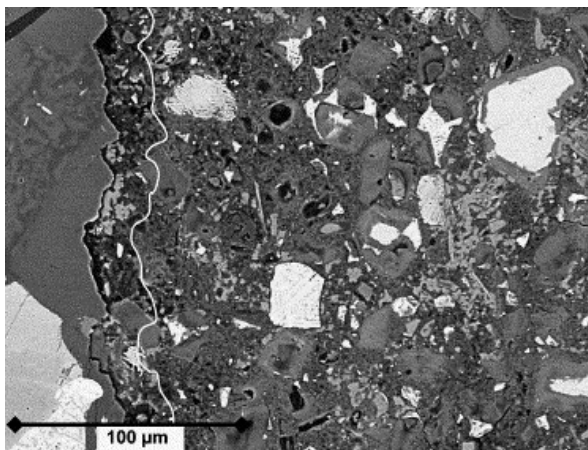
(b) image of interfacial transition zone of concrete (Scrivener, 2004)

Fig. 4 (a) Image of interfacial transition zone of concrete and (b) Diagram representing the interfacial transition zone and bulk cement paste

ITZ represents the weakest link of chain between the two components, and especially at the early hydration it is prone to cracking due to shrinkage or thermal invariants. The strength of ITZ depends on water-to-cement ratios, size and grading of aggregate, compaction degree, curing condition, humidity of environment.

Permeability of concrete: permeability is defined as the extent to which interfacial transition zone, leading to weaker and more permeable concrete. Although the
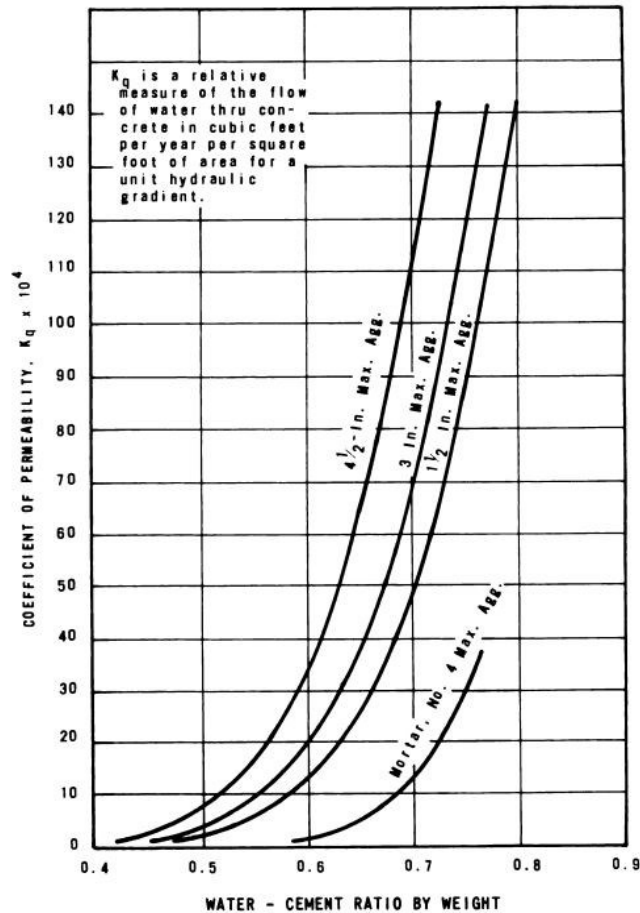
Fig. 5 Effects of water-cement ratios and maximum aggregate size on concrete permeability
(U.S. Bureau of Reclamation, 1975).

Concrete is a dense material, the size distribution and continuity of capillary voids in cement paste (that are dependent on water-cement ratios and degree of hydration) and microcracks in ITZ are indisputably permeable, which allows the transportation of aggressive liquids and gases through its solid structure.

Alkaline-environment of concrete: Cement paste of concrete contains hydrates of calcium (e.g., C-S-H, CH, and ettringite, C-A-$\bar{\text{S}}$-H) in a stable equilibrium with a high-pH pore fluid. Depending on the concentration of ions Na^+, K^+, and OH^-, the pH value of concrete ranges from 12.5 to 13.5. Due to its alkaline-rich cement paste, exposure of concrete to certain environments that has acidic liquids causes detrimental effects to its durability. It should be noted that the rate of chemical attacks depends on the degree of

permeability and pH of the aggressive fluid. For instance, free CO_2 in soft or stagnant water, acidic ions such as SO_4^{2-} and Cl^- in groundwater and seawater, and H^+ irons in industrial waters are attributed to lowering the pH below 6 and causing harmful effects to concrete. If the pH of the aggressive agent is over 6 and permeability of concrete is low, the rate of attack cannot be taken as serious (Mehta and Monteiro, 2006). Therefore, the durability of concrete is determined by its permeability (e.g., capillary voids, ITZ, and internal microcracks) and ability to keep the pH value over magnitude of 12.5.

2.1.3 Corrosion of steel rebars embedded in concrete

The embedded steel bars in sound concrete are initially passivated in the high-alkaline concrete environment (pH over 12.5). Alkaline containing in the pore solution of concrete promotes a passivative film (i.e., a thin protective oxide film on the rebar surface) that keeps steel rebar free from corrosion activity. Under this condition, although concrete is permeated by oxygen and water, the corrosion rate is still negligible (Bertolini, 2008). However, corrosion on the embedded reinforcements in RC structures can occur when the passivative film is removed and broken down. The two primary causes that lead to a removal or break-down of the passivative film are: carbonation of concrete and chloride penetration. The next two Sections will look into more details of these two causes of corrosion.

Steel corrosion is an electrochemical process in nature which involves the passage of electronic charge. According to Ahmard (2003), without an external electrical source, an electrochemical reaction can occur in concrete medium since the steel rebar itself functions as a mixed electrode (i.e., an area of the steel can serve as anode while another adjacent area as a cathode simultaneously) upon which coupled anodic and cathodic reactions can occur; whereas the porous concrete which is permeated by water and oxygen functions as an aqueous medium for electrical conductivity (see Fig. 6).
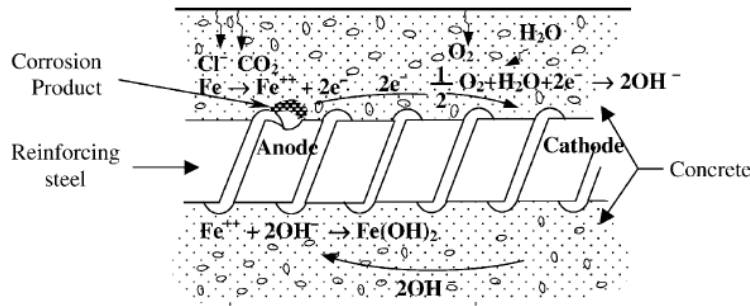
Fig. 6 Schematic illustration of the corrosion of reinforcement steel in concrete (Ahmad, 2003).

After the passive film on rebar surface is removed, the two half-cell reactions that occur in the corrosion process are widely known as anodic and cathodic half-cell reactions. The anodic half-cell reaction refers to the oxidation (dissolution of iron) to form ferrous ions (Fe^{2+}):

$$Fe \rightarrow Fe^{2+} + 2e^- \tag{1}$$

The above reaction is balanced by cathodic reaction of oxygen (O_2) reduction and then forms hydroxyl ions (OH^-):

$$1/2 O_2 + H_2O + 2e^- \rightarrow 2OH^- \tag{2}$$

$Fe(OH)_2$ can be generated through the combination between hydroxyl ions and ferrous hydroxide:

$$Fe^{2+} + 2OH^- \rightarrow Fe(OH)_2 \tag{3}$$

$Fe(OH)_2$ will be then oxidized to $Fe(OH)_3$ if there is sufficient oxygen:

$$4Fe(OH)_2 + O_2 + 2H_2O \rightarrow 4Fe(OH)_3 \tag{4}$$

From the above equations, it can be seen the diffusion of oxygen and water into the concrete means is the main cause of steel corrosion. Therefore, permeability of the concrete plays an important role in the electrochemical reaction of steel corrosion in concrete.

17

2.1.4 Carbonation-induced corrosion

Carbonation of concrete is a neutralization of the alkalinity of concrete. It involves a process in which carbon from carbon dioxide (CO_2) in the atmosphere gradually penetrates into concrete medium and decreases its normal pH value over 12.5 to below a magnitude of 9. In such an environment, the protective passivative layer is unstable and can be removed, allowing corrosion to take place on rebar surface if oxygen and water are available at the rebar depth (Heiyantuduwa et al. 2006). It was observed that carbonation occurs in RC structures naturally in a relatively slow pace and induces a rather uninform corrosion; however, it can inflict damages in an enormous scale. According to Papadakis et al. (1989), carbonation of concrete process is presented as chemical reactions in the equations below:

$$Ca(OH)_2 \ \rightarrow \ Ca^{2+} + 2OH^- \tag{5}$$

$$Ca^{2+} + 2OH^- + CO_2 \ \rightarrow \ CaCO_3 + H_2O \tag{6}$$

$$3CaO \cdot 2SiO_2 \cdot 3H_2O + 3CO_2 \ \rightarrow \ 3CaCO_3 \cdot 2SiO_2 \cdot 3H_2O \tag{7}$$

The reactions of the primary interest are in Eqs. (5)–(6) where alkaline constituent of concrete $Ca(OH)_2$ that is a solid of hydrated cement products reacts with CO_2. The reaction of C-S-H in Eq. (7) might happen after $Ca(OH)_2$ is depleted (e.g., by pozzolanic reaction in concrete made of blended cement). Several factors affect the carbonation depth in concrete (e.g., concrete cover, resistivity of concrete, effective diffusion coefficient and binding capacity for CO_2, curing condition, age, cement type, temperature variation, and relative humidity), and different conditions of environmental exposure (sheltered versus outdoor and underground versus atmospheric) play an important role in concrete carbonation process, Zhou et al. (2015).

2.1.5 Chloride-induced corrosion

Chloride can come from the internal source of concrete itself whose practice is now discouraged by the building codes; chloride is used as part of admixture to accelerate hydration at early age or as part of mixing sea water under certain unavoidable circumstances of limited local resources (Page 1982). However, Chloride-induced corrosion from the external source (i.e., sea water and deicing salt) is well recognized as a dominant concern for deteriorating RC structures exposed to marine and heavily-snowing environments. Through times, chloride from sea water or deicing salt gradually ingresses into the concrete through its continuity of pore and microcracks in the interfacial transition zone. When its centration reaches a critical threshold value, chloride iron induces local break downs of the passive oxide film (Gonzalez et al. 1995; Glass et al. 1997; Ann and Song 2007; Angst et al. 2011). In this way, it is observed chloride generates non-uniform corrosion on the steel reinforcement. According to Bentur et al. (1997), the process of chloride-induced corrosion can be explained by means of reactions below:

$$Fe^{2+} + 2Cl^- \rightarrow FeCl_2 \tag{8}$$

$$Fe \rightarrow Fe^{2+} + 2e^- \tag{9}$$

$$O_2 + 2H_2O + 4\,e^- \rightarrow 4\,OH^- \tag{10}$$

$$Fe^{2+} + 2\,OH^- \rightarrow Fe(OH)_2 \tag{11}$$

$$2\,Fe(OH)_2 + 1/2O_2 + H_2O \rightarrow Fe(OH)_3 \rightarrow Fe_2O_3.3\,H_2O \tag{12}$$
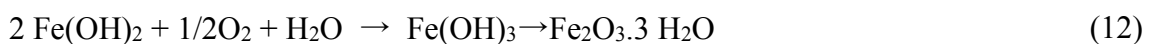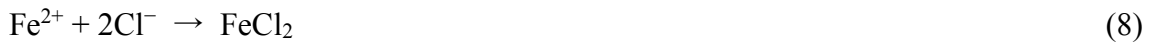
2.2 Corrosion effects on material mechanical properties of RC members

A number of studies have focused on the corrosion effects on the deteriorating mechanical

properties of RC. Several studies (Almusallam 2001; Palsson and Mirza 2002; Zhang et al. 2010) reported that the mechanical properties of the corroded rebar are affected by the corrosion levels and corrosion pits along the reinforcement. According to Zhang et al. (2010), the variation in the cross-sectional areas along a rebar length was the primary cause of the reduced nominal strength of the corroded rebar whereas its shortened yield plateau and reduced ductility mostly resulted from the stress concentration in the pitting corrosion. Another primary mechanical property that is affected by corrosion is the steel-concrete bond. Previous studies (Al-Sulaimani et al. 1990; Cabrera 1996; Auyeung et al. 2000; Fang et al. 2004) determined that the bond strength initially increased with corrosion levels in the pre-cracking stage, suddenly dropped to a low residual strength level due to the corrosion crack, and varied in a small magnitude, even up to a corrosion amount of 80%. Based on a comparison study performed by Sæther (2011), a large scatter of experimental results in the relationship between the corrosion amount and the bond strength was reported due to different test methods (i.e., different specimen and rebar sizes, current densities, compressive strengths and concrete cover).

2.3 Corrosion effects on the structural performance of corroded RC members

Several studies focused on the corrosion effects on the performance of RC structural members. Rodriguez et al. (1997) intensively investigated the effects of different types of corroded reinforcements (i.e., stirrups, tensile, or compression bars) on the structural capacity of corrosion-accelerated RC beams. In addition to the increased deflection and crack width in the service limit state and reduced ultimate loads, they also reported a change in the beam failure modes from bending to abrupt shear failures due to the corrosion pits in the stirrups. According to Castel et al. (2000a, b), the loss in the bending stiffness of the corroded RC beams in the service state was primarily attributed to the

coupling effects of the loss in the steel cross-section and deterioration in the local steel-concrete bond due to the corrosion cracking of concrete. Du et al. (2007) reported that the reinforcement corrosion increased the ductility of the over-reinforced beams and decreased the ductility of the under-reinforced beams; they also noted a risk of tensile rebar rupture for under-reinforced beams that had a corrosion level over 10%.

2.4 Accelerated corrosion test

In nature, it might take decades to for corrosion to initiate on steel rebars in RC structures. Therefore, to study the steel corrosion at a desired corrosion level within a reasonable time, an accelerated corrosion test is used to induce significant corrosion on the steel reinforcement. The impressed current technique is the most common method used to study reinforcement corrosion embedded in concrete although there are other methods available (e.g., impressed voltage technique, artificial climate environment, accelerated AC impedance technique, and accelerated chloride migration test). A large number of researches have been conducted using the impressed current technique to study the corrosion effects on the cracking of concrete cover (Alonso et al. 1998), bond behavior (Al-Sulaimani et al. 1990), and load-bearing capacity (Rodriguez, 1997) of reinforced concrete members.

The impressed current technique is conducted by supplying a constant current from a direct current (DC) power supply to the steel rebars embedded in concrete in order to provide significant corrosion in a short period of time. During the accelerated corrosion test, the reinforcing steel functions as the anode while the counter electrode (e.g., external copper plate and stainless steel plate) serves as the cathode. The current is impressed from the counter electrode to the rebar embedded in concrete with the help of the electrolyte (normally 3% or 5% sodium chloride solution). The applied current is varied on basis of the surface area of anode so that a constant applied current density can be achieved.

Fig. 7 illustrates the test set-up of accelerated corrosion test of reinforcement. The RC beams are partially immersed in a solution contains 5% of NaCl in the tank (Azad et al., 2007). The embedded steel reinforcement in the concrete that serves as anode is connected to the positive charge of DC (direct current) power supply while stainless steel plate that serves as cathode is connected to the negative charge of DC power. Anode, cathode and electrolyte constitute a closed circuit.
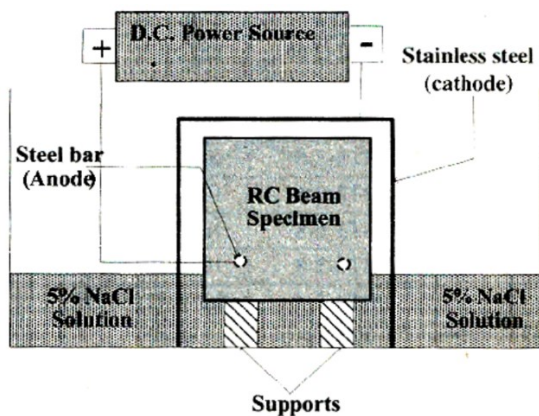
Fig. 7 Test set-up for accelerating corrosion of the steel rebars in the RC beam (Azad et al. 2007).

2.5 Study of spatial steel corrosion: destructive versus non-destructive monitoring method

Recently, more attentions have been paid on the study and modeling of spatial steel corrosion using experimental data obtained from the accelerated-corrosion RC members in the laboratory. It is anticipated that the statistical data of spatial steel corrosion obtained from the experimental tests in the laboratory can be used to together with the inspection or observation data from the in-situ structures in order to improve the accuracy of the estimation of the magnitude and variability of steel corrosion in the real structure and its long-term performance. Hence, it is important to develop monitoring methods which enables the study of how the steel corrosion varies and changes in space and time.

The common methods used in the literatures to study the spatial steel corrosion at different times of corrosion is described as follows. First, RC members were corroded
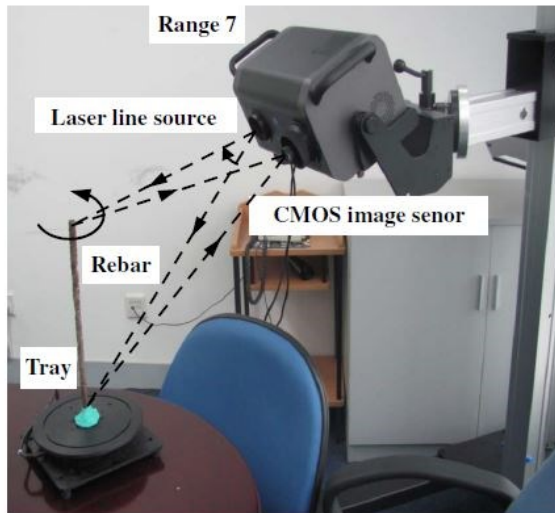
(a) Three-dimensional scanner
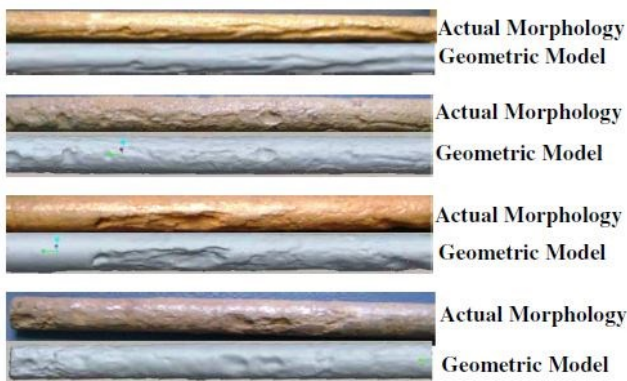
(b) 3D scanned versus actual morphology of corroded rebar

Fig. 8(a) Three-dimensional laser scanner and (b) 3D scanned versus actual morphology of corroded rebar (Zhang et al. 2014).

to obtain a various steel corrosion amounts at different corrosion times. After that, the destructive method is commonly used by severally breaking RC specimens to retrieved samples of corroded rebar for measuring their weight (Kashani et al. 2013a; Alonso et al. 1998; Vidal et al. 2004) or scanning the morphology of the retrieved corroded rebars with a 3D optical scanning tool, see Fig. 8, (Kashani et al. 2013b; Zhang et al. 2014).

However, because these methods require certain specimens to be demolished to study the evolution of steel corrosion, they may be error-prone due to the difficulty in repeating the same experimental conditions and other uncertainties (e.g., different

corrosion cracking patterns and locations of steel corrosion).

In concrete engineering, X-ray technology has been used as a non-destructive method to visualize and investigate steel corrosion in concrete structures. Beck et al. (2010) used X-ray computer tomography to examine the surface of a very small steel cylinder (9 mm in diameter and 10 mm long) at various stages of corrosion inside a mortar specimen. The reported difference between the mass loss, which was determined using the constructed 3D X-ray tomography image, and the actual mass loss after breaking the 40–60%. Akiyama and Frangopol (2013) demonstrated that the X-ray apparatus was a specimen was suitable tool for continuously investigating the weight loss of a corroded rebar that was embedded in a cylinder (100 mm × 200 mm) and a prism (100 mm × 100 mm × 400 mm). A digital image analysis based on the X-ray radiography of the shape of a corroded rebar from different viewing angles was used to determine the steel weight loss. The difference between the calculated steel weight loss based on the digital image analysis of the X-ray photogram and the measured value after damaging the specimen is only about 10%. This monitoring technique allows the study of spatial steel corrosion at different times of corrosion.

Chapter 3: Experimental program

3.1 Overview of experimental plan

An experimental plan is established to study the effects of W/C ratio and stirrups on the spatial steel weight loss and corrosion cracking. To achieve these goals, five RC beams were fabricated and divided into two groups. The details of the specimens are shown in Table 1 and Fig.9. For the first group, specimens I-1, II-1 and II-2 were produced with W/C ratios of 50, 40 and 65%, respectively. The second group consists of specimens I-1, III-1 and III-2. Specimens I-1 and III-2 have stirrup spacings of 100 and 165 mm, respectively, whereas specimen III-1 has no stirrups. For the compressive strength test, six cylinders (100 mm × 200 mm) were also produced for each concrete mixture.

The experimental procedure is as follows. The corrosion of embedded longitudinal rebar was accelerated via the electrochemical technique. At specific time intervals prior to performing the X-ray radiography, the crack widths were recorded by obtaining images of surface cracking on the bottom of the beams. X-ray radiography was performed once before the steel corrosion initiated and several times to capture

Table 1. Details of test specimens

Notation	Cross-section	Span length	Bar diameter	Cover	W/C	Stirrup
	(mm)	(mm)	(mm)	(mm)	(%)	
I-1	140 × 80	1460	13	20	50	DB6@100*
II-1	140 × 80	1460	13	20	40	DB6@100
II-2	140 × 80	1460	13	20	65	DB6@100
III-1	140 × 80	1460	13	20	50	-
III-2	140 × 80	1460	13	20	50	DB6@165

* Deformed bars with a diameter of 6 mm arranged in intervals of 100 mm

(a) Beams I-1, II-1, and II-2

(b) Beam III-1

(c) Beam III-2
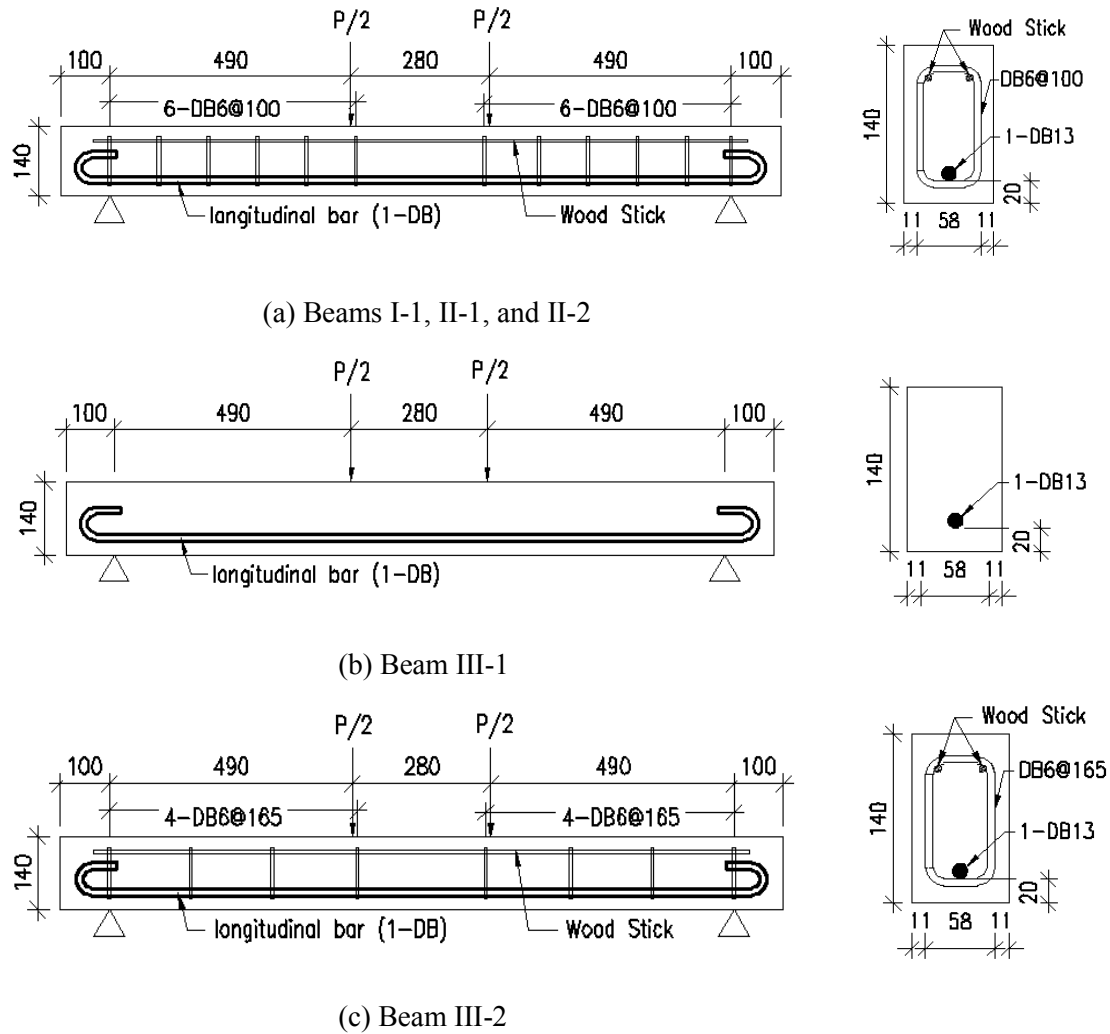
Fig. 9. Details of the test beams

photograms of the developing morphology of the non-corroded and corroded rebars from different viewing angles. These photograms were used in the digital image processing to estimate the steel weight loss.

3.2 Materials and mix-proportion of concrete

All specimens were fabricated using identical material constituents. Ordinary Portland cement with a specific density of 3.16 g/cm^3 was used. The fine aggregate has a fineness modulus of 2.64 and a specific density of 2.60 g/cm^3. The coarse aggregate has a maximum size of 20 mm (Gmax $\leq$ 20 mm) and a specific density of 2.64 g/cm^3.

26

Table 2. Mixing proportion of concrete

Notation	G_{max}	W/C	s/a**	Water	Cement	FA[†]	CA[††]	AE***
	(mm)	(%)	(%)	(kg/m³)	(kg/m³)	(kg/m³)	(kg/m³)	(ml/m³)
I-1	20	50	44.3	181	362	754	961	2715
II-1	20	40	42.3	178	445	694	961	3338
II-2	20	65	47.3	185	285	829	940	2138
III-1 & III-2	20	50	44.3	181	362	754	961	2715

** Fine aggregate ratio

*** Air entranced agent

[†]Fine aggregate

[††]Coarse aggregate

A deformed rebar with a diameter of 13 mm (DB13) was used as the longitudinal rebar, and deformed rebars with a diameter of 6 mm (DB6) were used as stirrups. All rebars were of the same steel quality grade, SD345. The details of the concrete mixing proportions are shown in Table 2.

3.3 Specimen fabrication procedure

The same fabrication procedure was performed for all the specimens. When used, the stirrups were wrapped with vinyl tape to prevent direct contact with the longitudinal rebar. The stirrups were arranged at the shear span to prevent abrupt shear failure during the corrosion process. Before pouring the concrete, electrical wire was tied to one end of the steel reinforcement. Two days after fabrication, the mould was stripped off from the specimens, and the specimens were cured in water in a 23–25 °C room for 28 days.

3.4 Accelerated-corrosion test

After the specimens were cured, the steel corrosion process was initiated using the electrolytic technique. The detailed assembly of the electrolytic experimental test is
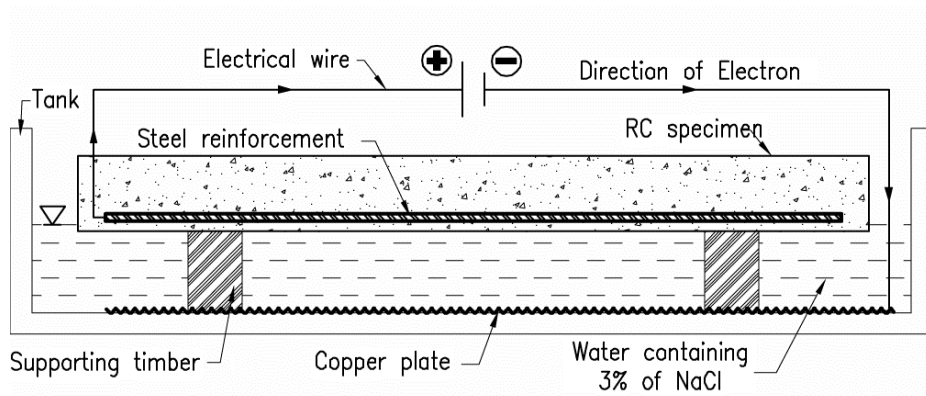
Fig. 10 Electrolytic experimental test setup.

shown in Fig. 10. The RC specimen was placed on two pieces of supporting timber and partially immersed in a 3% sodium chloride (NaCl) solution in a tank in a controlled environment at 23–25 °C. The external copper plate, which is placed under the supporting timbers below the specimen, served as the cathode; the embedded rebar inside the specimen served as the anode. To ensure that the tests could be completed within a reasonable timeframe, the total impressed current was adjusted for each specimen to maintain the same current density (i.e. 1000 $\mu A/cm^2$) to pass over the surface of the rebar. The accelerated corrosion process proceeded until the accumulated current time reached approximately 620 h (i.e. about 25 days).

3.5 Surface crack width measurement

The external surface cracks that occurred along the bottom of the specimens at various steel weight losses were imaged by a digital camera before X-ray radiography was performed. The location of the captured images corresponds to that of the captured X-ray image, i.e. 250–1090 mm from the left side of the specimens. This required seventeen 50-mm-long images to be continuously obtained along the bottom of the specimens. Note that in this experimental study, the visual longitudinal corrosion cracking occurred only at the bottom of the corroded beams. Crack width measurements on the photographs were

continuously performed every 5 mm until a distance of 1090 mm was reached using an advanced image analysis programme.

3.6 X-ray photogram acquisition procedure

Using the X-ray configuration in Fig. 11, images of the non-corroded and corroded areas of the rebar inside the specimen were captured from different viewing angles once before the initiation of corrosion and several times during the corrosion process at various steel
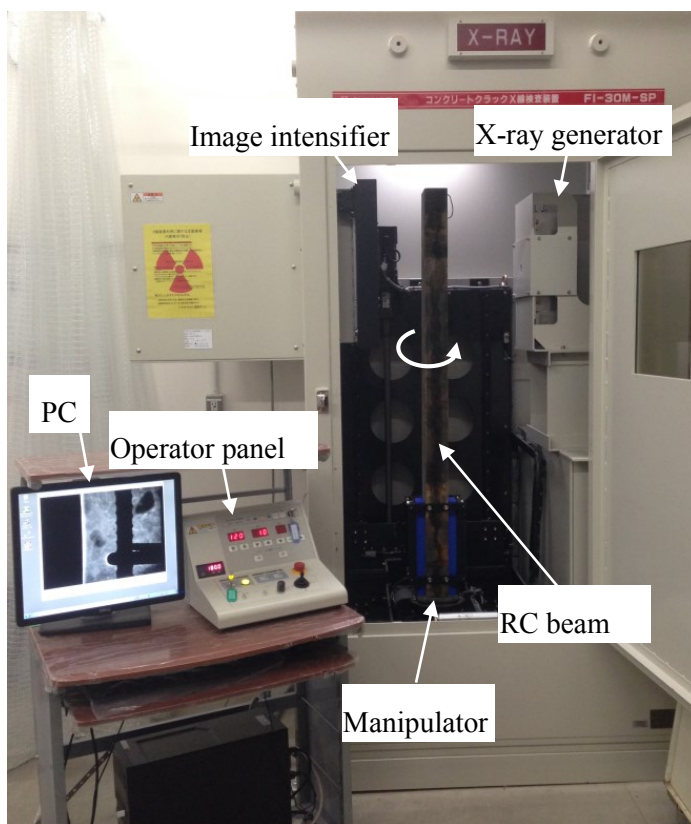
Fig. 11 X-ray imaging setup at Material Engineering Laboratory, Waseda University.
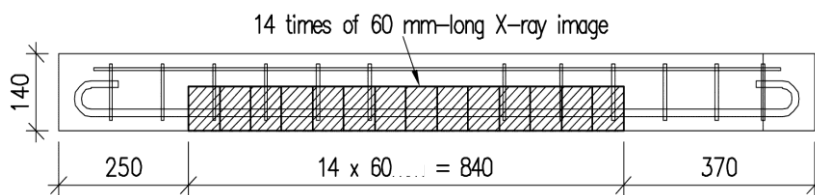
Fig. 12 Total steel bar length captured by the X-ray apparatus (all dimensions are in mm).
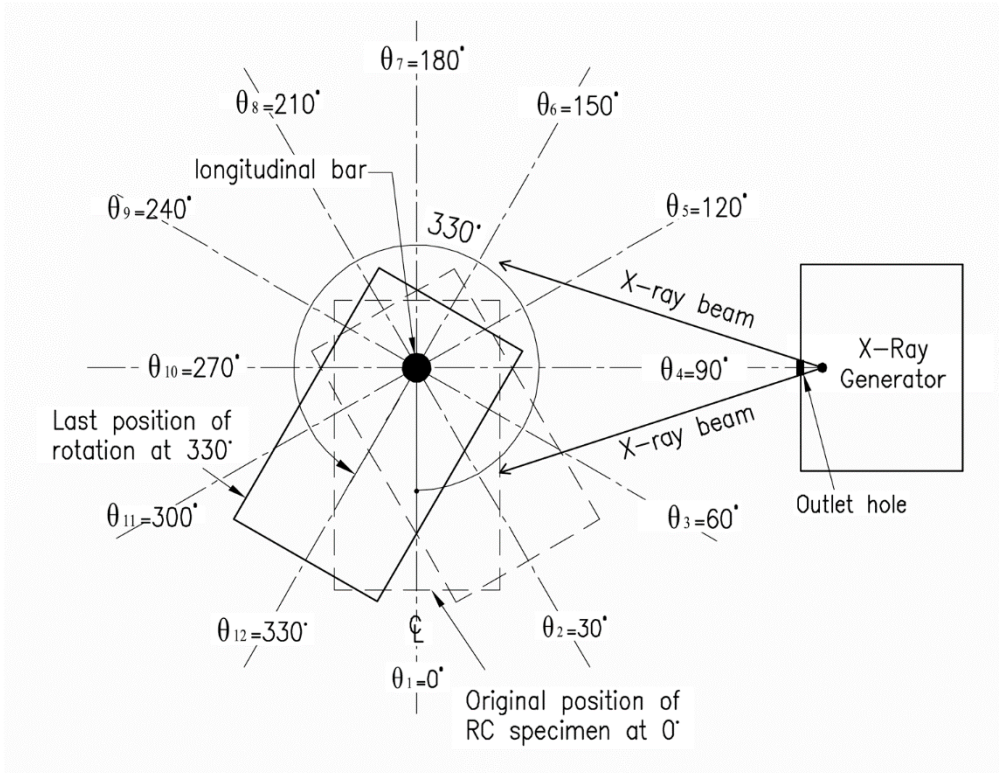
Fig. 13 Top view of the specimen setup and views of the steel bar at different angles associated with the rotation of the RC specimen.

weight losses. Images of the rebar from 12 viewing angles (i.e. 0°, 30°, 60°, 90°,120°, 150°, 180°, 210°, 240°, 270°, 300° and 330°) were recorded. At each angle, the total length of the rebar imaged by the X-ray apparatus was 840 mm. Fourteen 60-mm-long images were consecutively captured (see Fig. 12). The X-ray radiography procedure used to acquire the photograms consists of two main steps, as described below. The first step is setting the specimen in an appropriate position. The specimen was placed on a manipulator located between the X-ray intensifier and generator in the X-ray chamber. This manipulator was used to translate and rotate the specimen into the desired positions via the operation panel. The specimen was first rotated to $\theta_1 = 0°$ and horizontally adjusted into the position where the centre of the embedded rebar was aligned with the middle point of the X-ray source outlet. This setting fixes the centre of the rebar as the centre point of rotation of the specimen, as indicated in Fig. 13. In the vertical direction, the

specimen was then shifted up or down relative to the X-ray radiation source to obtain the starting position of 370 mm from the base of the specimen on the computer screen. After setting up the specimen, radiography images were acquired by attenuating the primary X-ray beam with materials of different densities and thicknesses. The chosen power and current settings for the X-ray radiography are functions of the source-to-specimen distances and concrete thicknesses when the specimen is rotated to different viewing angles: 120 kV, 1.2 mA for viewing angles of 0°, 30°, 60°, 120°, 150°, 180°, 210°, 240°, 300°, and 330° and 145 kV, 1.2 mA for viewing angles of 90° and 270°. Starting from a known position at 370 mm from the base of the specimen and a viewing angle of $\theta_1 = 0°$, the RC specimen is vertically translated 14 times in increments of 60 mm relative to the radiation cone beam supplied by the X-ray generator. The radiation penetrates the RC specimen for visualisation, and the attenuated X-ray radiation detected by the image intensifier reveals the composition details of various densities. After the attenuated X-rays are converted into visible light on a fluorescent screen, an equipped charge-coupled device camera unit, whose capture command is linked to and controlled by a software program, is used to capture and store the light intensity as digital values. These digital values comprise a 1024 × 768-pixel greyscale image. The same process was performed repeatedly to capture images from the remaining viewing angles. The viewing angles of 0°, 30°, 60°, 90°,120°, 150°, 180°, 210°, 240°, 270°, 300° and 330° refer to those rebar views at which the specimen was rotated to angles θ_1, θ_2, θ_3, θ_4, θ_5, θ_6, θ_7, θ_8, θ_9, θ_{10}, θ_{11} and θ_{12}, respectively (see Fig. 13).

3.7 Beam bending test

At the end of the experimental procedure, a four-point beam bending test was conducted by applying loads at two symmetric points on the beam as indicated in Fig. 9. The recorded test items are the applied load P and the mid-span displacement δ which was

measured by a dial gauge placed under the mid-span of the beam. Before the bending test, a system of grid lines was marked on one side surface of the beams. During the test, the load was applied slowly so that the tracing and marking tasks of the cracking paths and the then-measured loads could be conveniently performed on one side surface of the beams. The load was applied until the beam collapsed (e.g., by the concrete being crushed or the reinforcement being ruptured). At several damaging stages, the evolution of the cracking patterns was recorded by photographing the cracking patterns on one side surface of each beam.

3.8 Estimating procedure of steel corrosion

3.8.1 Image enhancement

Some of the 60-mm-long images of the original rebar that were captured using the X-ray apparatus before corrosion are shown in Fig. 14. In general, the original images at 0° and 180° provide the clearest views, followed by images at 30°, 150°, 210° and 330° and then by images at 90° and 270°, respectively. The worst images are those at 60° and 330°. This ordering is a result of the differences in the thickness of the concrete composite penetrated by the X-ray radiation during the image capturing for a particular specimen rotation angle. For example, at 0° and 180°, the specimen is in a favourable position, as the concrete thickness encountered by the X-ray radiation is only 80 mm, providing a notably clear image. In contrast, at 90° and 270°, the angle is unfavourable, as 140 mm of concrete is penetrated by the X-ray radiation.

Furthermore, the post-corrosion image at the viewing angle of 0° in Fig. 15(a) illustrates the shape of the corroded rebar at a mean steel weight loss of 8.79%, which corresponds to that of non-corroded rebar in Fig. 14(a). However, although the image at this angle provides the clearest view, it remains difficult to carefully examine the corrosion products or decayed shape of the rebar. In Fig 15(b), for the image after

enhancement, the corrosion products and decayed shape of the corroded rebar can be more easily identified.

Therefore, it is necessary to enhance the image before the analysis to readily obtain detailed information from the image. In the enhancement process, the fine details of the image were revealed or the blurred regions were reduced using Image-Pro Plus software version 7.0 of Media Cybernetics, Inc. (2012) to accentuate the intensity changes and make the high-contrast edges visible. Visualising the high-contrast edges between the rebar and concrete composite allows the area shapes of the concrete composite and rebar to be easily distinguished, which is important for determining the area of the corroded rebar to estimate the steel weight loss.

(a) Angle 0°   (b) Angle 30°   (c) Angle 60°   (d) Angle 90°   (e) Angle 150°

(f) Angle 180°   (g) Angle 210°   (h) Angle 300°   (i) Angle 270°   (j) Angle 330°
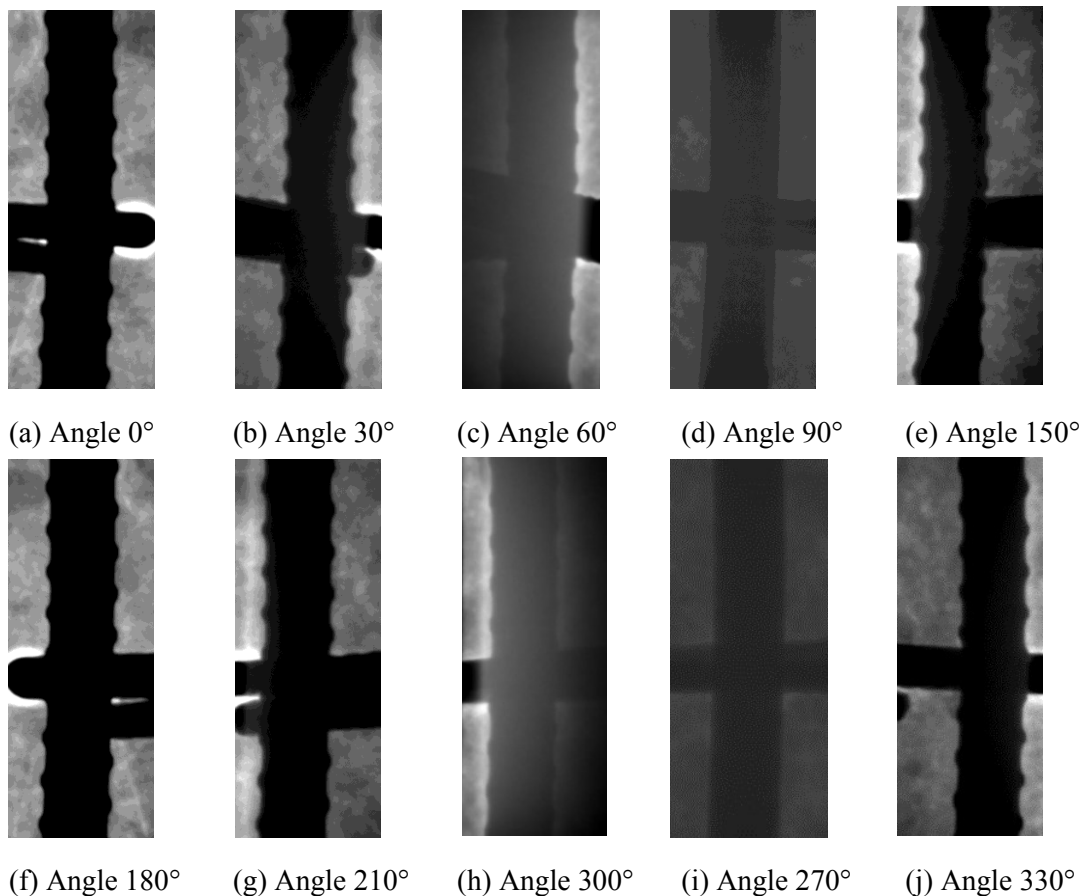
Fig. 14 Ten X-ray images of the original steel bar obtained at different viewing angles.
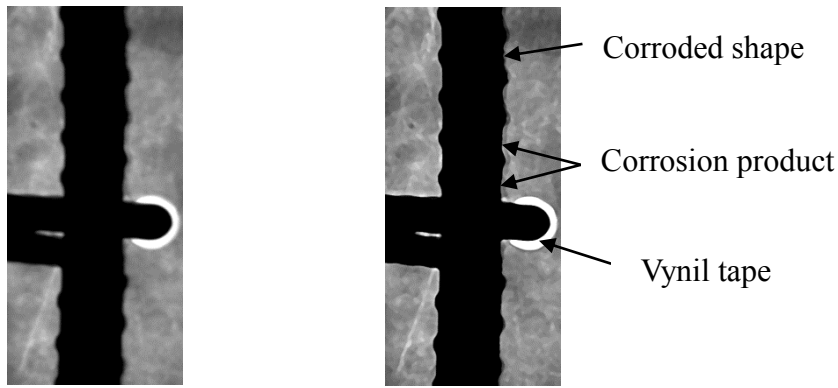
(a) Before enhancement   (b) After enhancement

Fig. 15 X-ray images of a corroded steel bar at 0° with a mean steel weight loss of 8.79% (a) before and (b) after enhancement.

3.8.2 Estimation of steel weight loss by digital image processing

To estimate the steel weight loss using the X-ray photograms, the area of the original rebar before corrosion and that of the corroded rebar at a given time during the corrosion process need to be determined. At each 8 viewing angles, the two types of rebar areas are determined through the digital image analysis of X-ray photograms (i.e., a manipulation of the stored digital data of the image in terms of numerical representations of pixels). Note that only X-ray images from 8 viewing angles (i.e., $\theta_1 = 0°$, $\theta_2 = 30°$, $\theta_4 = 90°$, $\theta_6 =150°$, $\theta_7 = 180°$, $\theta_8 = 210°$, $\theta_{10} = 270°$, and $\theta_{12} = 330°$) were used for estimating the steel weight loss along the corroded bars because: (1) the time-consuming and laborious works involved in digital image analysis of considerably large amount of data and (2) a good accuracy of steel weight loss estimation could be obtained which will be presented in the next section.

In this paper, the acquired X-ray photograms are 8-bit grayscale images with 1024×768 pixels. The grayness levels of the pixels are numerically represented by 256 intensity values ranging from 0 for completely black to 255 for completely white. This numeric representation enables the image software to distinguish pixels of different colors. Because the reinforcing rebar is denser than the concrete composite or corrosion product,

it absorbs the X-ray radiation most efficiently. Thus, the rebar always produces the darkest pixels with the lowest intensity range compared to the concrete composite and corrosion product in the images. Fig. 16 illustrates the profiles of the intensity values for a row of pixels that corresponds to a line drawn on each of the above X-ray photograms. All the profile lines show that the intensity values of the rebar at 0°, 30°, and 90° in the middle part of each graph are always lower than those of the corrosion products located close to the corroded rebar and the concrete in the left- and right-hand sides of the graphs. This finding also holds for the images of other viewing angles, as the X-ray images captured at 0° and 180°; 30°, 150°, 210°, and 330°; and 90° and 270° are very similar (see Fig. 14).

Therefore, by manipulating the intensity values of the pixels of the rebar, the total number of pixels below a minimum threshold of intensity values that represent the area of rebar alone can be selected, counted, and classified using the image processing software. To facilitate the analysis of the digital data of the image, the 60-mm-high image of all viewing angles is sliced into twelve 5-mm-high images (see Figs. 17(a) and (b)). The height of 5 mm of image is chosen since this length is small enough for the human eyes to easily control and perform the area segmentation between the corrosion product and steel rebar in order to obtain a high accuracy of estimated steel weight loss which will be discussed later on in the next Section. Figs. 18(a) and (b) present histograms of the accumulated numbers of pixels classified by intensity values for the 5-mm images of the non-corroded and corroded rebars in Figs. 17 (a) and (b), respectively. The histograms explicitly show that the total number of pixels of a selected intensity threshold of 0-62 is 8,723 for the non-corroded rebar area, greater than the corresponding value of 8,449 pixels of a selected intensity threshold of 0-59 for the corroded rebar area. After the number of pixels of non-corroded and corroded rebar was determined, the total area was obtained by multiplying the number of pixels by the unit area per pixel as follows:

$$A_{\theta n} = P_{\theta_n} \times A_p \tag{13}$$

$$A'_{\theta_n} = P'_{\theta_n} \times A_p \tag{14}$$

where A_{θ_n} and A'_{θ_n} are the areas of the original rebar before corrosion and the corroded rebar at each viewing angles, respectively; θ_n denotes the viewing angles in which the subscript $n = \{1, 2, 4, 6, 7, 8, 10, 12\}$; P_{θ_n} and P'_{θ_n} are the number of pixels of the area of the original rebar and corroded rebar, respectively, at any of n viewing angles; and A_p is the unit area (in millimeter square per pixel) in the image. The volume of the rebar before and after corrosion can then be calculated as follows:

$$V_{\theta n} = \frac{\pi(A_{\theta n})^2}{4L} \tag{15}$$

$$V'_{\theta n} = \frac{\pi(A'_{\theta n})^2}{4L} \tag{16}$$

Where V_{θ_n} and V'_{θ_n} are the volumes of the original and corroded rebars, respectively, at a viewing angle θ_n; and L is the length of the rebar, which is 5 mm herein. The steel weight loss per length L (mm) of the rebar is determined by taking the average of each value of the steel weight loss for each viewing angle as follows:

$$Rw = \frac{1}{k}\sum\frac{(V_{\theta n} - V'_{\theta n})}{V_{\theta n}} \times 100 \tag{17}$$

where Rw is the steel weight loss in percentage (%) per length L (mm) of rebar, θ_n denotes the viewing angles in which $n = \{1, 2, 4, 6, 7, 8, 10, 12\}$, and k is the number of viewing angles ($k = 8$ for the 8 different viewing angles studied here).

It is worth noting that since the 2D projected longitudinal areas of rebars of X-ray images are different along the rebar length at different viewing angles due to the presence and absence of ribs as shown Figs. 16 (a) to 16(c), the rebar weight per unit length of 5 mm along a bar length is not the exactly the same. This problem seems to hinder a good accuracy of this estimation method. Nevertheless, as mentioned earlier, this method focuses on estimating the average steel weight loss per 5 mm for 8 different
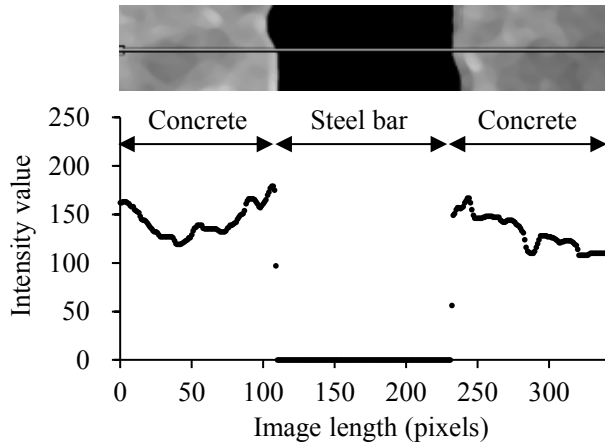
(a) Angle 0°
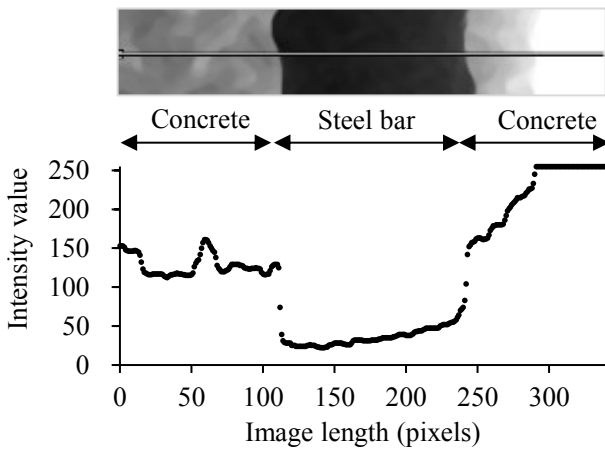
(b) Angle 30°
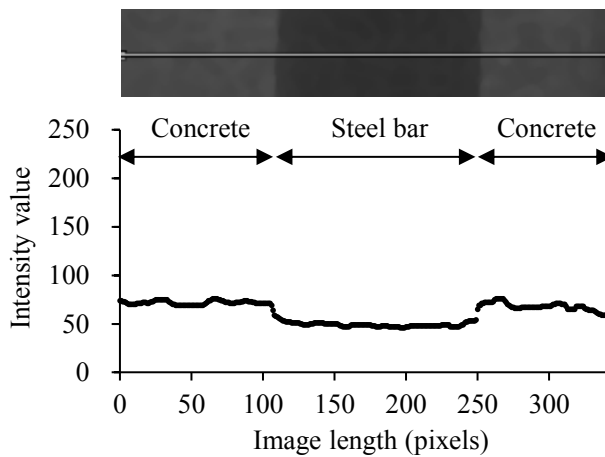
(c) Angle 90°

Fig. 16 Profiles of the intensity values for a row of pixels in the X-ray photograms at three different viewing angles.
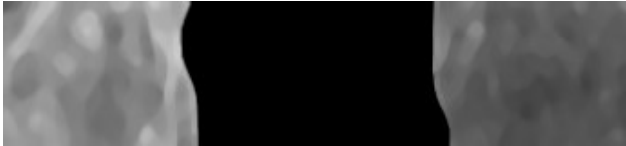
(a) Non-corroded steel bar at *MRw* = 0.00% (*MRw* is the global average steel weight loss)
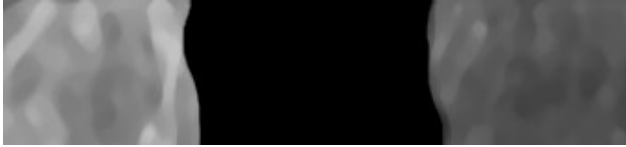
(b) Corroded steel bar at *MRw* = 6.05% (*MRw* is the global average steel weight loss)

Fig. 17 Sliced 5-mm-high X-ray photograms in (a) non-corroded steel bar at *MRw* = 0.00%, and (b) corroded steel bar at *MRw* = 6.05%.
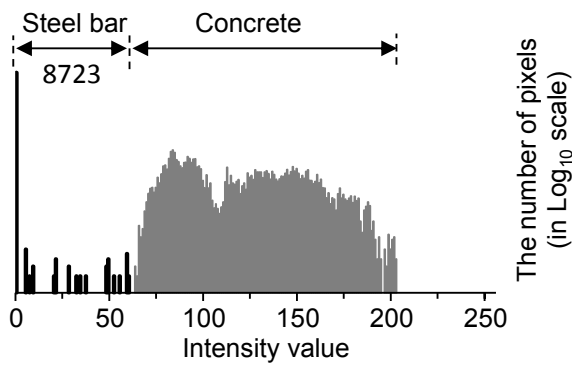
(a) Non-corroded steel bar at *MRw* = 0.0%
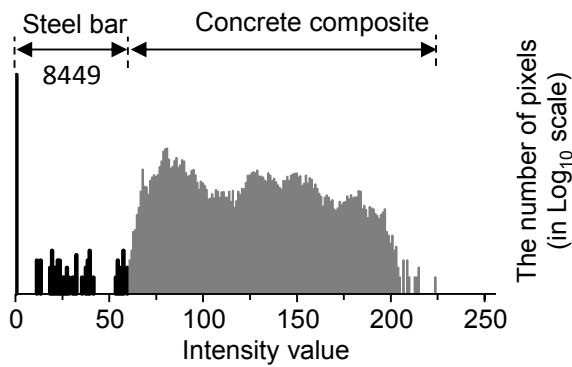
(b) Corroded steel bar at *MRw* = 6.05%

Fig. 18 Histograms of the accumulated number of pixels classified by intensity values for the steel bars in Figs. 17(a) and 17(b).

viewing angles in percentage using the longitudinal areas of corroded and original bars from X-ray image. In the estimation procedure, the longitudinal areas of corroded and original rebars were compared at same viewing angle and location. In this consistent way over the length of rebar, it means the area of corroded rebar with ribs is compared to that of original rebar with ribs at the same location and viewing angle, and the same thing applies to the corroded and original rebars without ribs at other viewing angles and locations; and finally, the result of weight loss is obtained by averaging the weight loss determined form every 8 viewing angles. Therefore, using this consistent way of comparison between original and corroded rebars at the location with rib and without ribs, it can be said the error associated with the ribs is not significant. This can be proved as the high accuracy of the estimated steel weight loss is confirmed, as discussed in the next Section.

Chapter 4: Experimental results

4.1 Accuracy of the estimated steel weight loss using X-ray images

After the completion of all the tests, the concrete specimens were demolished to retrieve the samples of corroded rebars. Next, all the rebars were immersed in a water tank containing 10% diammonium hydrogen citrate solution for 24 hours to remove the corrosion products, and the weights of the corroded rebars were then measured using a laboratory digital scale. Table 3 lists the comparison of estimated and measured steel weight loss.

Table 3. Estimated weight loss versus actual measured weight loss.

Specimens	Estimated weight loss (%)	Actual weight loss (%)	Absolute difference (%)
I-1	19.65	16.63	3.02
II-1	16.97	13.71	3.26
II-2	23.18	20.62	2.56
III-1	27.23	24.48	2.75
III-2	25.54	22.51	3.03

Note that the differences between the steel weight losses estimated using the digital image analysis and the actual measured steel weight losses are approximately 3%. This result demonstrates the good accuracy of the present estimation method for steel weight loss. The weight losses quantified via the X-ray images appear to be higher than the actual measured amounts, indicating that the employed X-ray method marginally overestimates the actual measured weight loss of embedded rebars in RC members. One possible cause of the overestimation is the inability of the projected 2-D X-ray images to provide information about pit corrosion on the rebar surface. Consequently, the estimated

cross-section areas based on the projected areas of the rebar using the X-ray image are slightly higher than those based on the actual areas of rebars embedded in the RC beams.

4.2 Behavior of spatial variability associated with steel weight loss and crack width

Fig. 19 illustrates the continuous spatial growth of the steel corrosion visualized using the X-ray technique and the propagation of longitudinal corrosion cracking at the bottom of the beams at different stages of corrosion. Comparing the X-ray images and photographs, it is found that the steel weight loss Rw occurs gradually and at locations near the areas exacerbated by the longitudinal surface crack widths Cw. These weight loss locations are noticeable at some of the locations of the arranged stirrups and in the center of the span.

Figs. 20-24 show the spatial distribution of the steel weight loss Rw and surface crack width Cw at their corresponding locations along beams I-1, II-1, II-2, III-1, and III-2, at various global average steel weight losses (MR_w). Note that because R_w could not be obtained at the locations of the arranged stirrups, there are regular gaps in the graphs at both of the shear spans, from 250 to 610 mm and from 850 to 1090 mm, except for specimen III-1, which had no stirrups. In general, it can be observed that Cw increases as Rw increases. The distribution of Rw and Cw at various stages of steel corrosion is spatially non-uniform because Rw and Cw fluctuate erratically along the specimens. The non-uniformity of Rw and Cw becomes increasingly prominent with increasing MRw and MCw.

In Fig. 25, the standard deviations of Rw and Cw indicate that the distributions of Rw and Cw increasingly diverge from their means as MRw and MCw increase. This can be interpreted as the spatial variability in Rw and Cw becoming increasingly large as the steel weight loss and crack width increases. Yamamoto et al. (2011) who studied the distribution of steel weight loss along the corroded bar using a great number of corroded
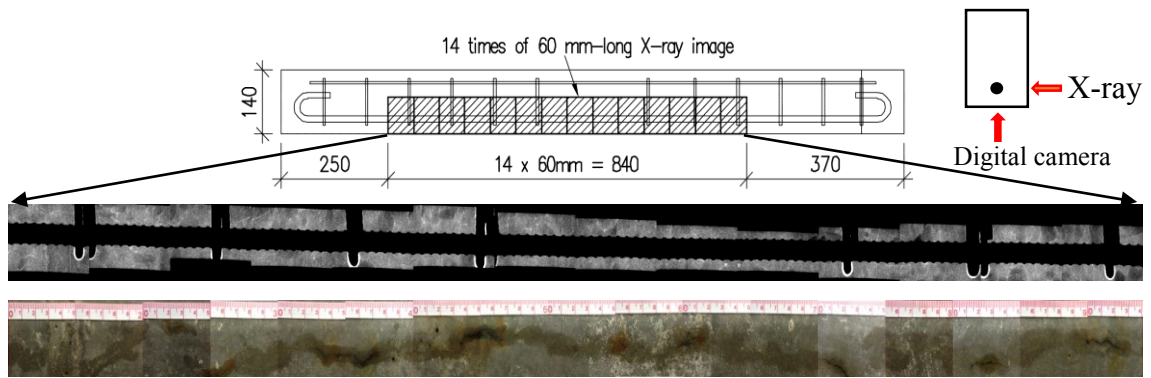
(a) $MRw = 0.68\%$
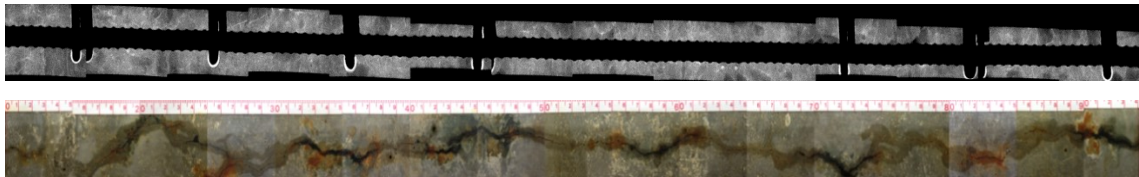
(b) $MRw = 2.60\%$
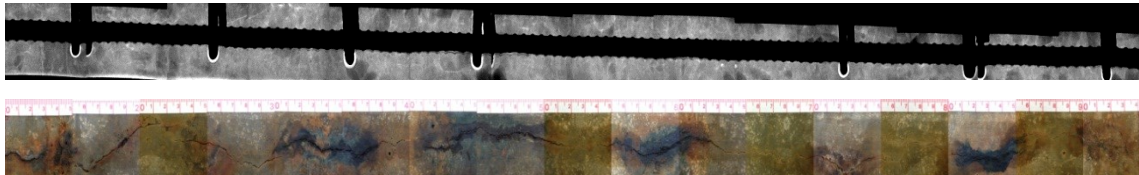
(c) $MR_w = 6.05\%$
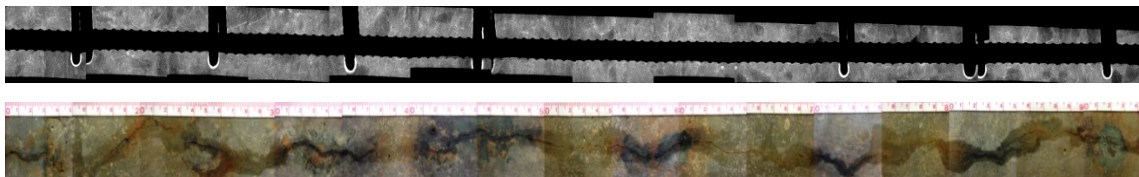
(d) $MR_w = 8.77\%$
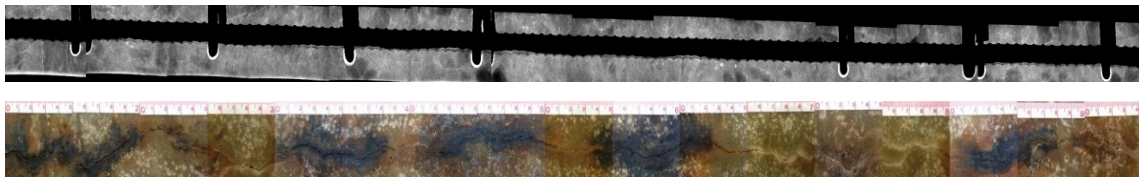
(e) $MR_w = 14.21\%$
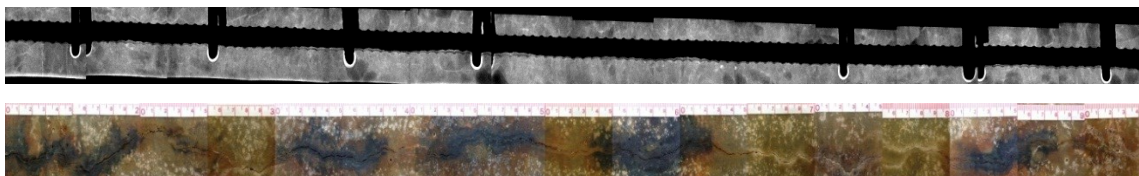
(f) $MRw = 19.68\%$

Fig. 19 Spatial growth of the steel weight loss and corrosion cracking of specimen I-1 for six different values of MRw.

RC beams also reported the same behavior that the non-uniform degree of steel cross-section losses of the corroded reinforcement increases with the corrosion loss. The cause of this larger spatial variability might result from the greater contribution of the larger surface cracks to the increase of Rw. When chloride penetrated from outside, corrosion cracking allowed much higher concentration of chloride to reach the rebar surface more easily, according to Andrade et al. (1993).

On the other hand, the maximum steel weight loss Rw,max and crack width Cw,max, which are denoted by square symbols in the graphs, do not usually occur at the corresponding locations. Several maxima of Rw, denoted by square symbols in the graphs, and other peaks (not maximum points) of Rw occur close to the locations of the stirrups (i.e., approximately at 300 mm, 400 mm, 500 mm, 600 mm, 860 mm, 960 mm, and 1060 mm) for specimens I-1, II-1, and II-2 in Figs. 20(a), 21(a) and 22(a). This is probably due to the fact that the thinner concrete covers at the locations of the installed stirrups expose the longitudinal rebar to chloride and thus cause it to corrode more quickly than the rebar at other locations. As a result, it can be confirmed from Fig. 19 that the locations of initial crack that was induced by the steel corrosion products occur at the locations of stirrups.

The locations of the peaks often shift depending on the mean values. For example, the Rw,max of specimen I-1 is located at approximately 580 mm at MRw of 0.68% and 2.60% but shifts to approximately 490 mm at larger values of MRw. However, Fig. 20(a) and (b) show that some peaks of Rw and Cw also occur at approximately the same locations, namely, 310, 490, 610, and 730 mm. This finding emphasizes the influence of steel weight loss on the increase in crack widths at corresponding locations along the specimen.
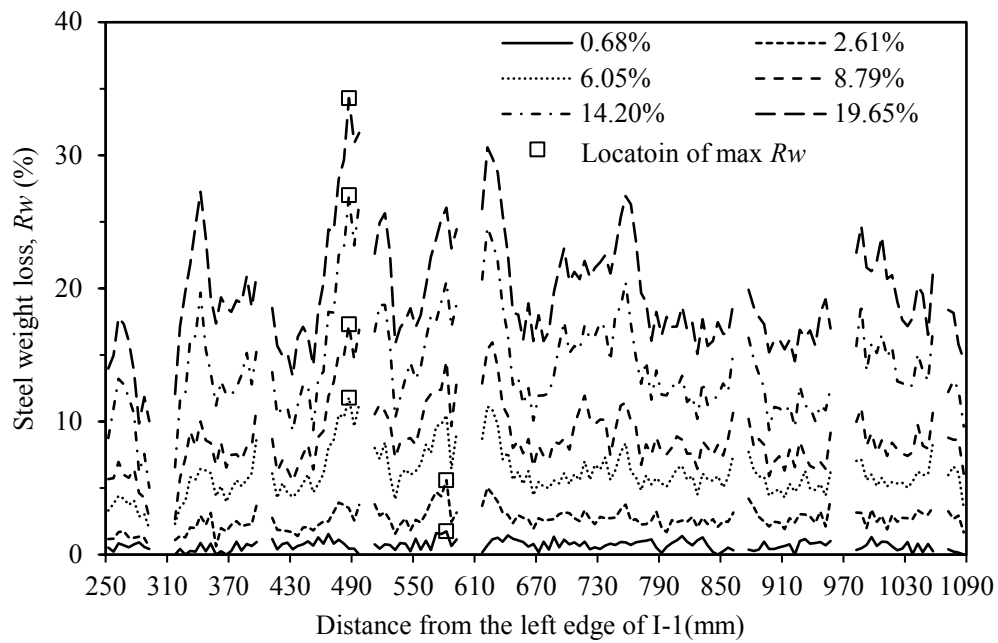
(a)
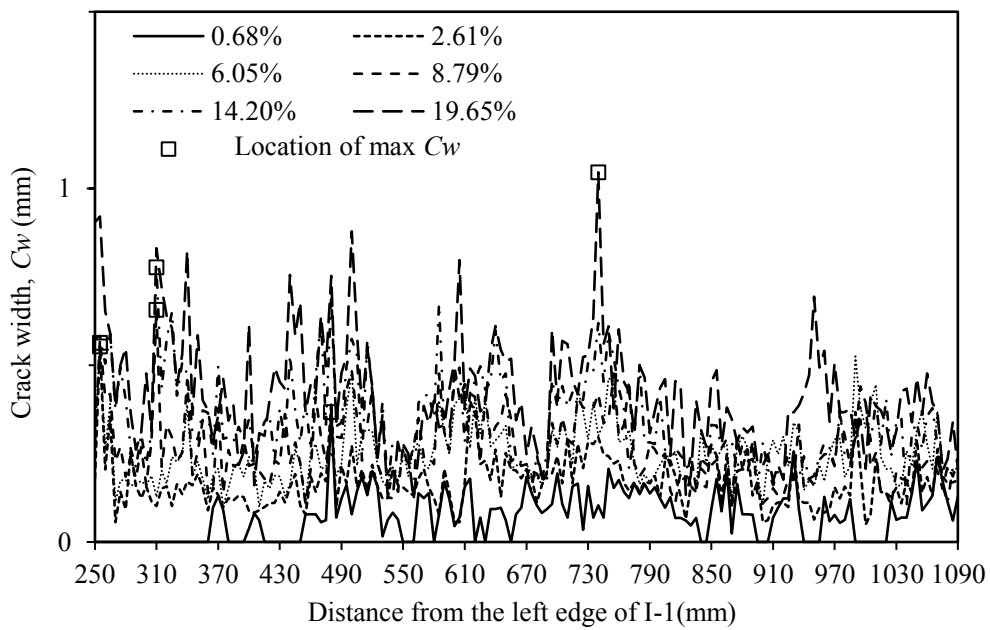
(b)

Fig. 20 Spatial distribution of the (a) steel weight loss and (b) surface crack width of beam I-1.
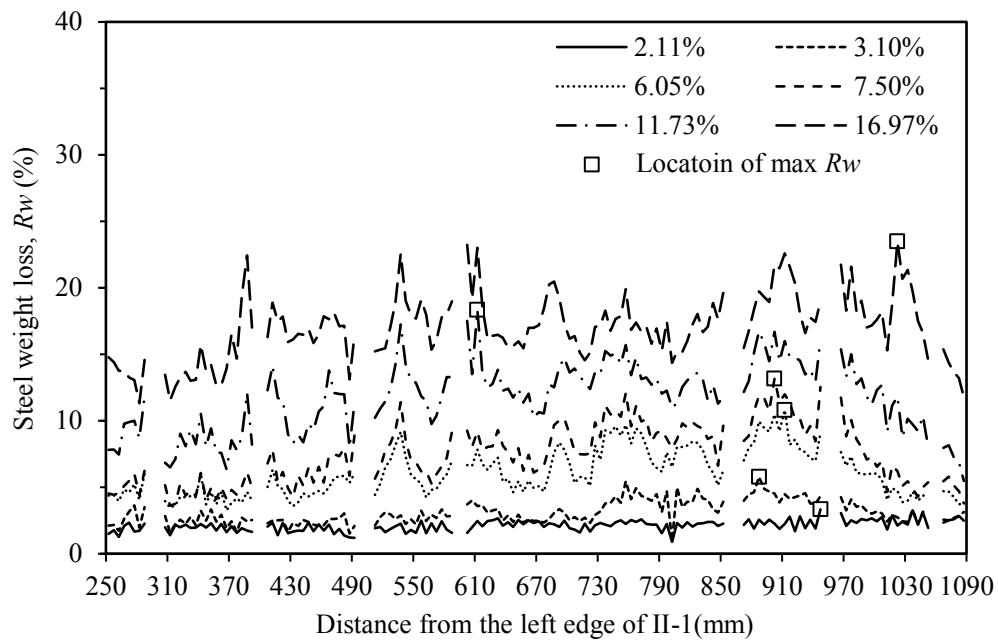
(a)
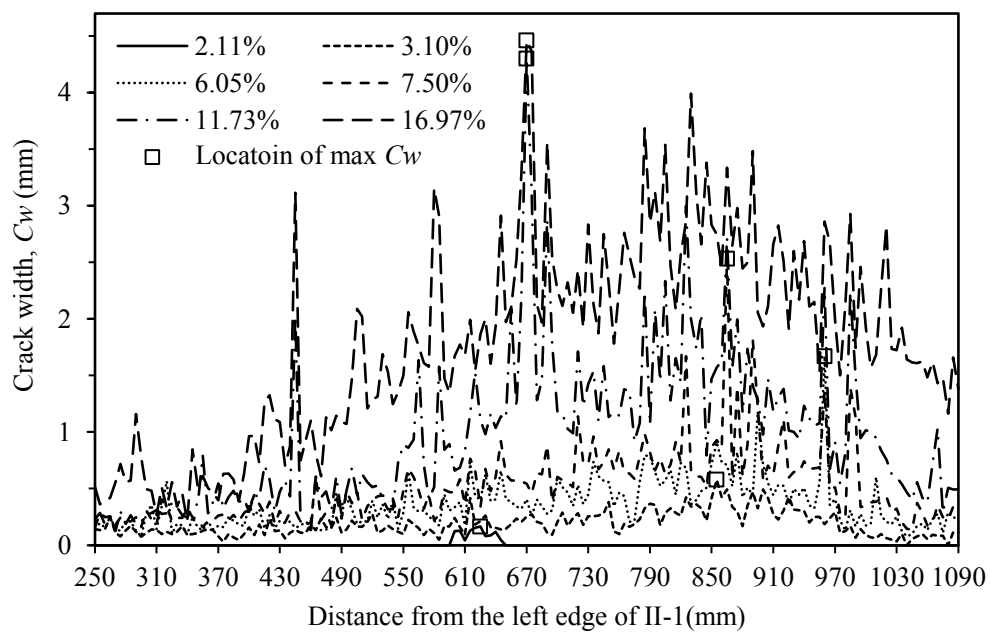
(b)

Fig. 21 Spatial distribution of the (a) steel weight loss and (b) surface crack width of beam II-1.
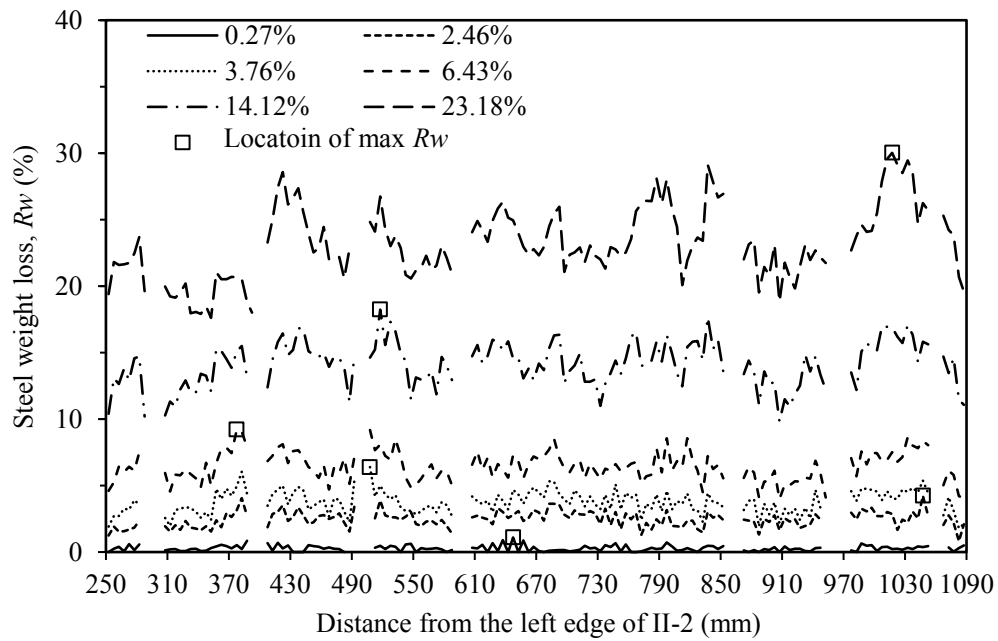
(a)
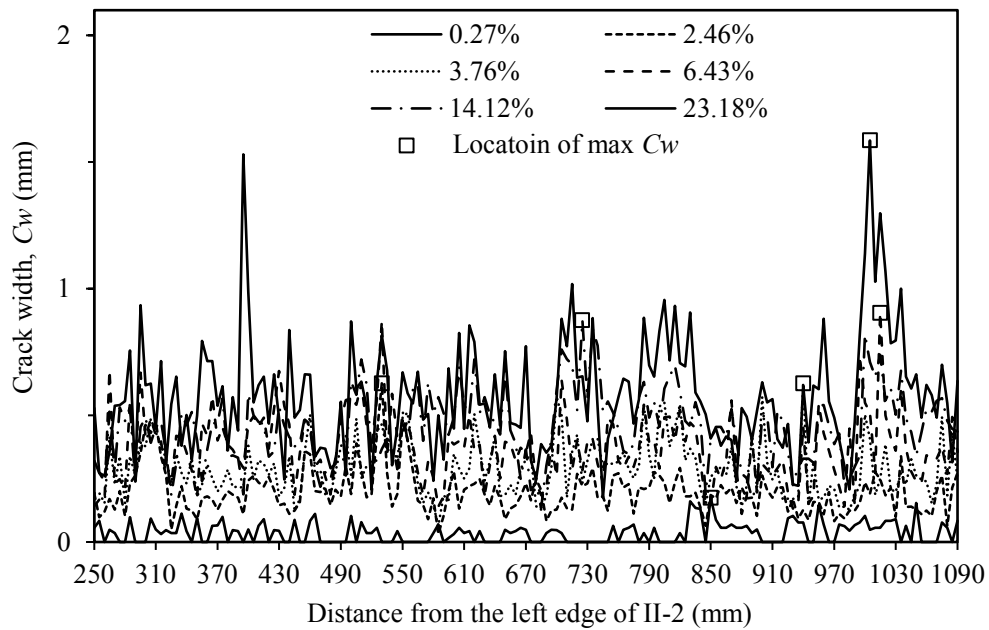
(b)

Fig. 22 Spatial distribution of the (a) steel weight loss and (b) surface crack width of beam II-2.
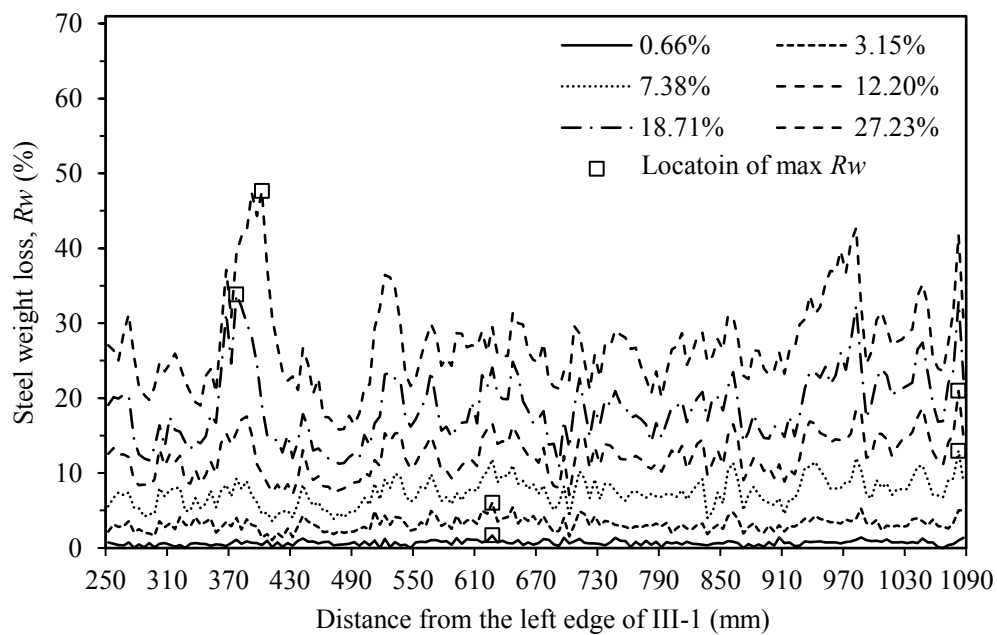
(a)
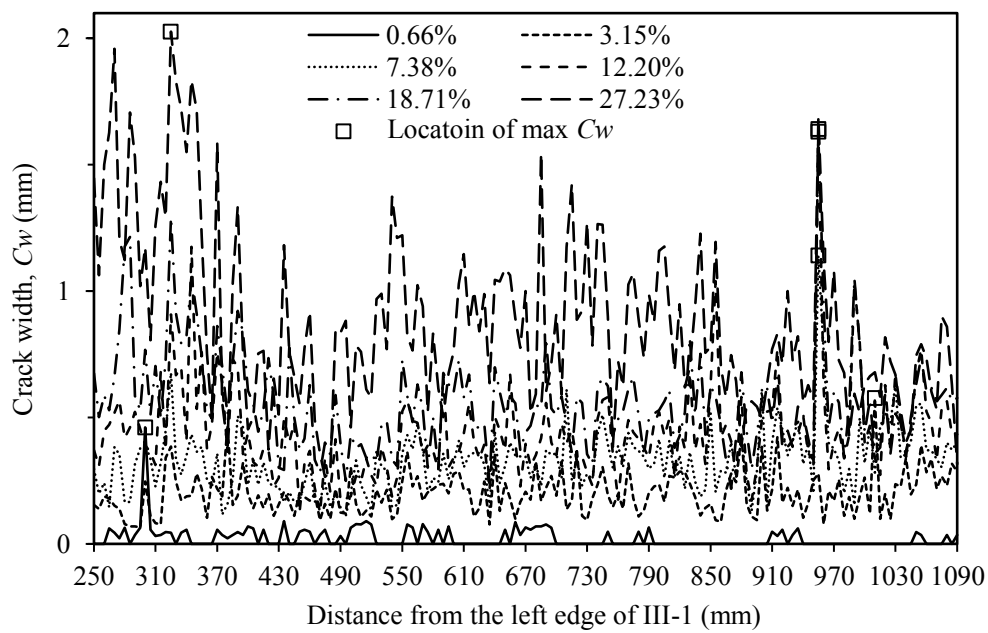
(b)

Fig. 23 Spatial distribution of the (a) steel weight loss and (b) surface crack width of beam III-1.
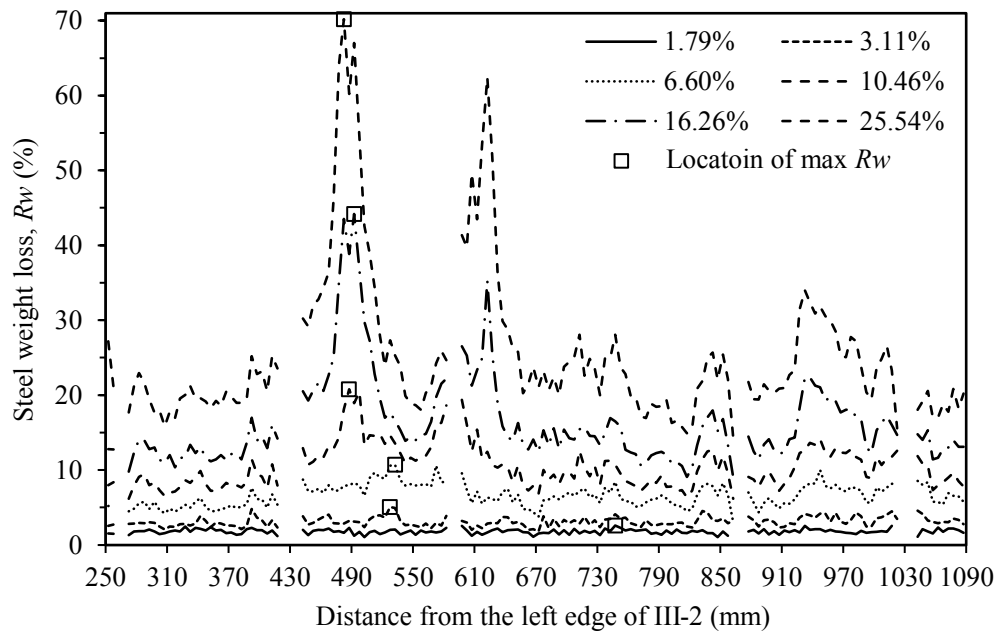
(a)
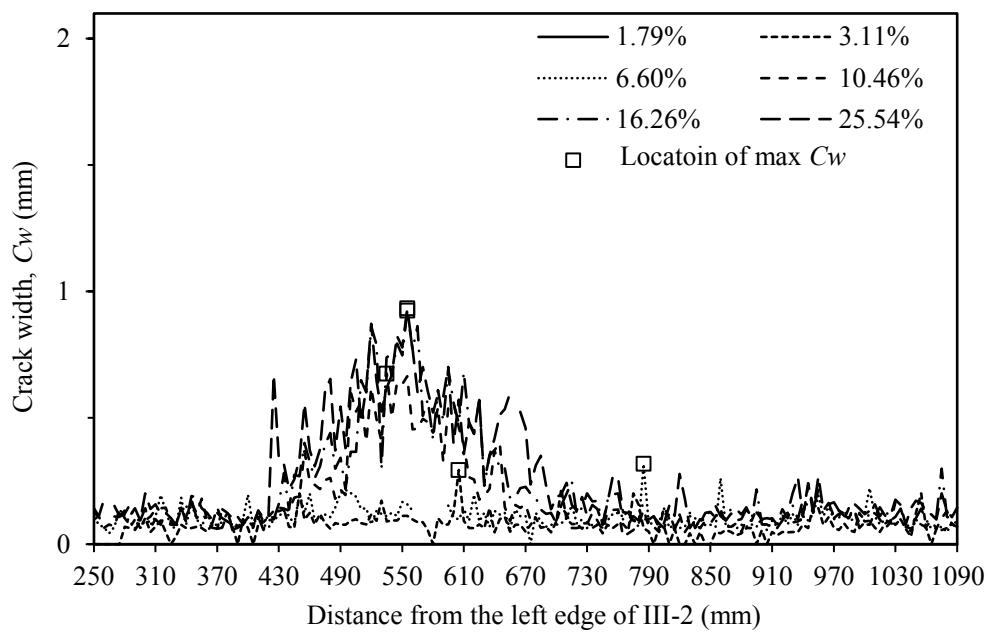
(b)

Fig. 24 Spatial distribution of the (a) steel weight loss and (b) surface crack width of beam III-2.

(a)   (b)
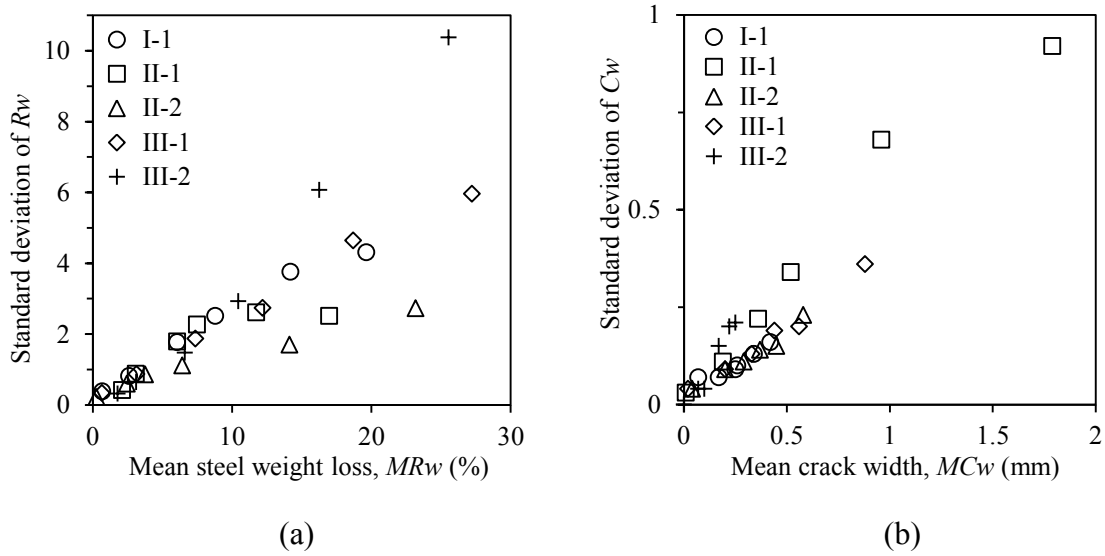
Fig. 25 Relationship between the standard deviations and mean values of *Rw* and *Cw*.

4.3 Trend of steel weight loss and crack widths

In addition to the previously mentioned non-uniform behaviors of the spatial distributions of *Rw* and *Cw*, a trend is consistently observed among the graphs in Figs. 20-24. Although the spatial variabilities of *Rw* and *Cw* increase as their mean values increase, it is worth noting that their erratic shapes tend to have a clear trend as *MRw* exceeds approximately 5%. For example, in Fig. 20(a) for specimen I-1, the spatial distributions of *Rw* at different *MRw* of 8.79%, 14.20%, and 19.65% seem to increase, following a very similar fluctuating pattern to the previous distributions of *Rw* at *MRw* = 6.05%. The spatial distributions of *Rw* in Figs. 21(a), 22(a), 23(a), and 24(a) also exhibit a similar spatial growth behavior as *MRw* increases beyond 5%. Similarly, the fluctuating pattern of the distribution of crack widths in Figs. 20(b), 21(b), 22(b), and 24(b) seems to follow the same trend as *MRw* exceeds 0.5%; however, the trend of the spatial distribution of crack widths appears to be weaker than that of *Rw*.

With respect to this behavior, a strong relationship can be found between the standard deviation and differences between the maximum and minimum values of steel

corrosion (*Rw,max* – *Rw,min*) and crack widths (C*w,max* – C*w,min*), as shown in Figs. 26 and 27. The significant merit of this relationship is that it might be possible to estimate the spatial variability of *Rw* and *Cw* between two different points if the maximum and minimum values of *Rw* or *Cw* between these points can be determined via in situ
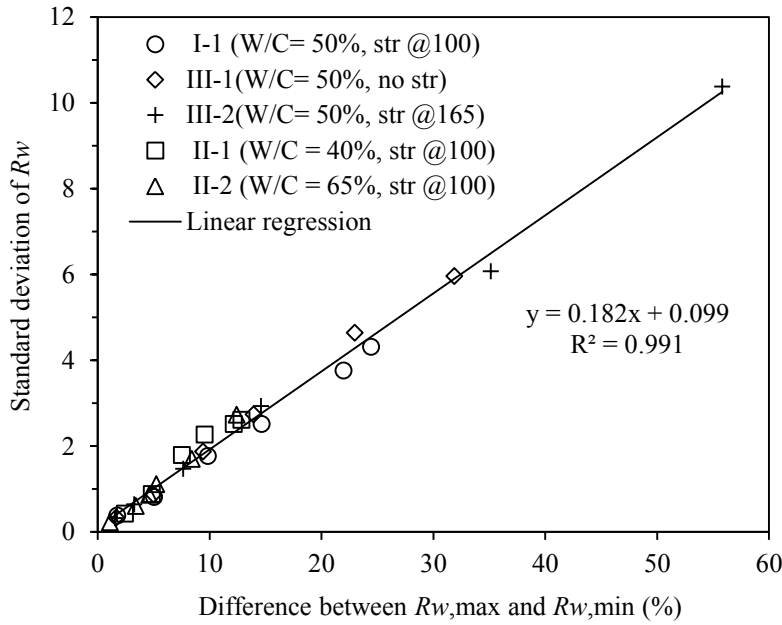
Fig. 26 Relationship between the standard deviation and the difference between *Rw,max* and *Rw,min*.
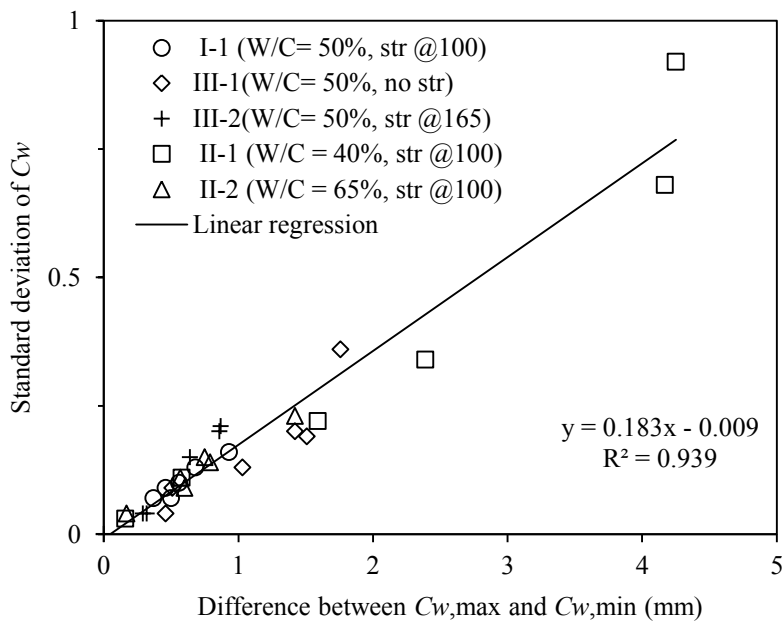
Fig. 27 Relationship between the standard deviation and the difference between *Cw,max* and *Cw,min*.

inspection. Due to this consistent spatial growth trend, it might be preferable to estimate the distribution of steel corrosion of RC members using the inspection results of steel corrosion from the in situ structure when the mean steel weight loss exceeds 5%.

4.4 Effect of water-to-cement ratios on spatial variability in steel corrosion

Fig. 28 shows the increase in the means of Rw and Cw as a function of corrosion time for specimens with different W/C ratios. From Fig. 28(a), because the trend lines of the three specimens exhibit similar behavior, there appears to be no obvious effect of W/C ratios on the growth of steel corrosion. Fig. 28(b) shows the effects of different W/C ratios on the surface crack widths. It can be seen that the crack widths of the specimens with W/C ratios of 40% grew more quickly than those with W/C ratios of 50% and 65%. Therefore, the crack widths of specimens with lower W/C ratios tend to grow more quickly than those with higher W/C ratios. These results are in agreement with the findings of Alonso et al. (1998). There is a delay in the increase of the crack widths for specimens with higher W/C ratios, which have greater porosity to accommodate the corrosion product and reduce the internal pressure.
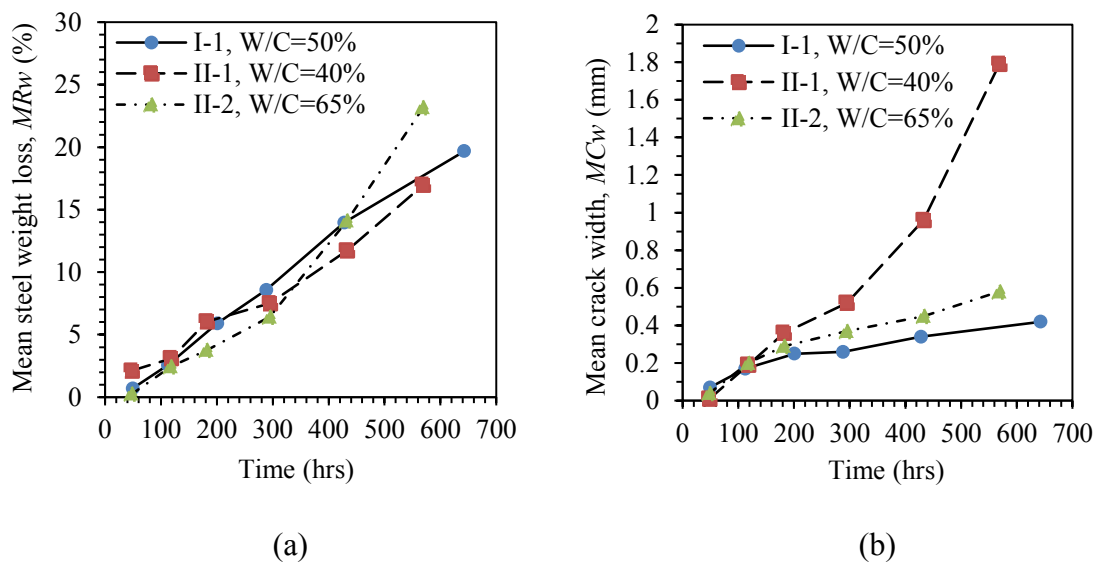
Fig. 28 Effects of W/C ratios on the development of (a) steel corrosion and (b) crack width.
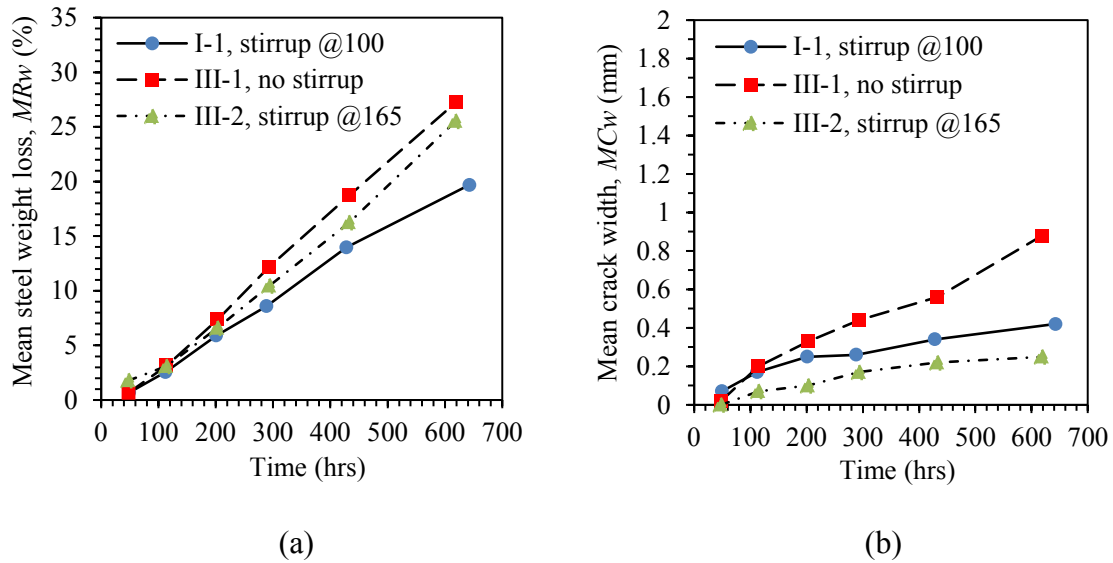
Fig. 29 Effects of stirrups on the development of (a) steel corrosion and (b) crack width.

4.5 Effect of stirrups on spatial variability in steel corrosion

Fig. 29 shows the effects of stirrups on the development of steel corrosion and crack widths for the beams exposed to approximately the same amount of accumulated current. Figs. 29(a) and (b) indicate that the steel corrosion and surface crack width of the specimen having no stirrups (i.e., III-1) increase more quickly than those of other specimens having stirrups (i.e., I-1 and III-2). For the steel corrosion of the specimens having stirrups, Fig. 29(a) shows that the longitudinal rebar of specimen III-1, with a stirrup spacing of 165 mm, is corroded more quickly than that of specimen I-1, with a stirrup spacing of 100 mm. Thus, decreasing the stirrup spacing or increasing the number of stirrups slows the steel corrosion. In Fig. 29(b), because the mean crack width of specimen I-1 increases more quickly than that of specimen III-2, one can conclude that increasing the number of stirrups might accelerate the growth of crack widths.

4.6 Relationship between steel weight loss and corrosion crack width

The graphs in Figs. 30-34 show the relationships between the steel weight loss and the

surface crack widths at their corresponding locations for all the specimens. Generally, the scattered points are increasingly highly dispersed with increasing *MRw*. Therefore, the relationship between *Rw and Cw* weakens significantly at higher *MRw*. However, it is also found that the steel weight loss increases with increasing crack width. Especially in the initial part of the corrosion process, up to a crack width of about 0.3 mm, both the steel weight loss and crack width appear to be linearly related for all the specimens.

This result is inconsistent with previous findings reported in the literature. For example, Vidal et al. (2004) found a linear approximation between the two parameters for the RC specimens with corrosion crack widths of about 1 mm, which is similar to the finding by Alonso et al. (1998) although these authors reported that the scatter of their relationships increased with the corrosion crack width and became significant as the crack width was over 1 mm. This inconsistency might be caused by the differences in the experimental procedure such as the magnitude of current density to corrode the specimens. Further research is needed to investigate the effects of the current densities, structural details, and concrete qualities on the relationship between the steel weight loss and crack width.
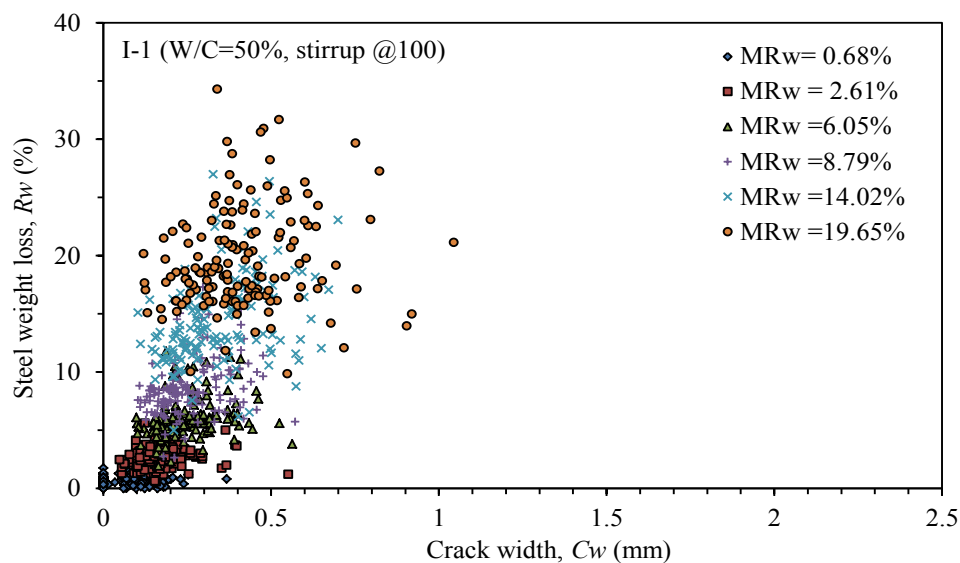
Fig. 30 Relationship between the steel weight loss and crack width of specimen I-1.
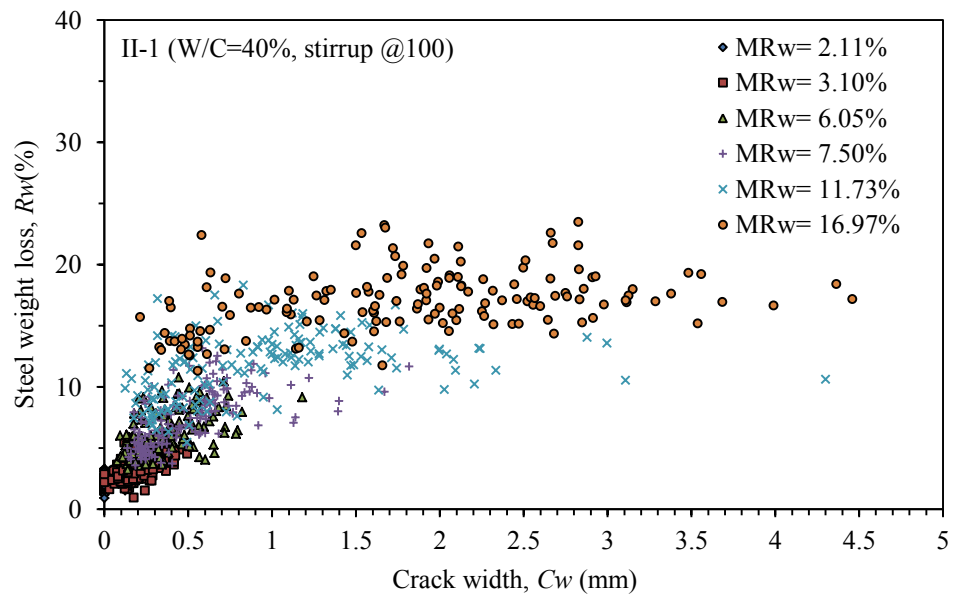
Fig. 31 Relationship between the steel weight loss and crack width of specimen II-1.
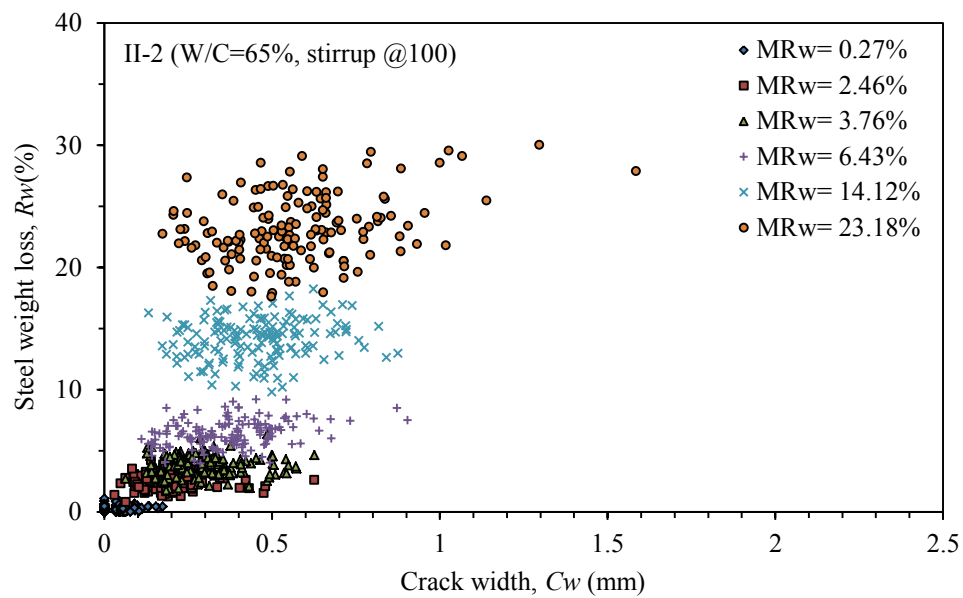
Fig. 32 Relationship between the steel weight loss and crack width of specimen II-2.
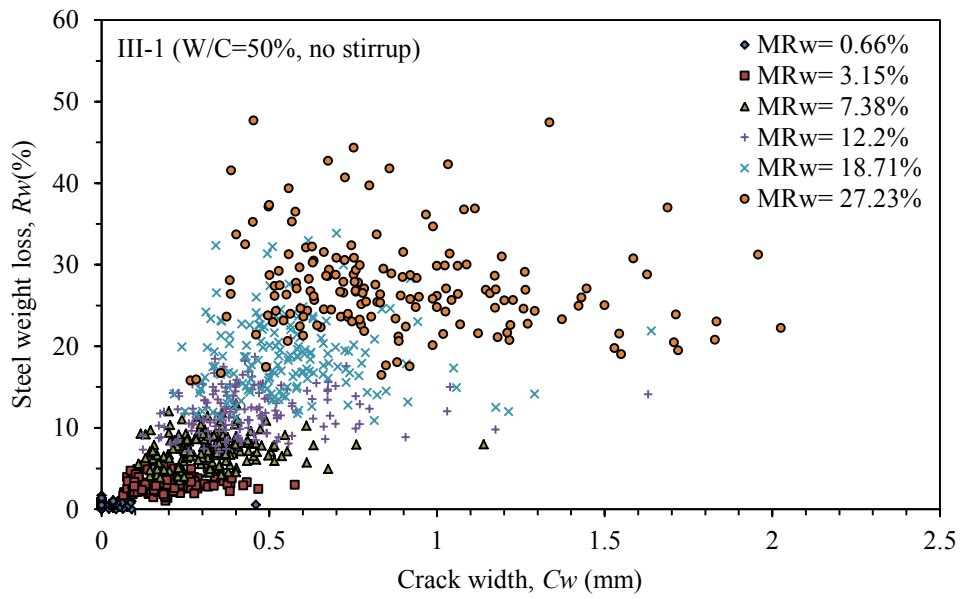
Fig. 33 Relationship between the steel weight loss and crack width of specimen III-1.
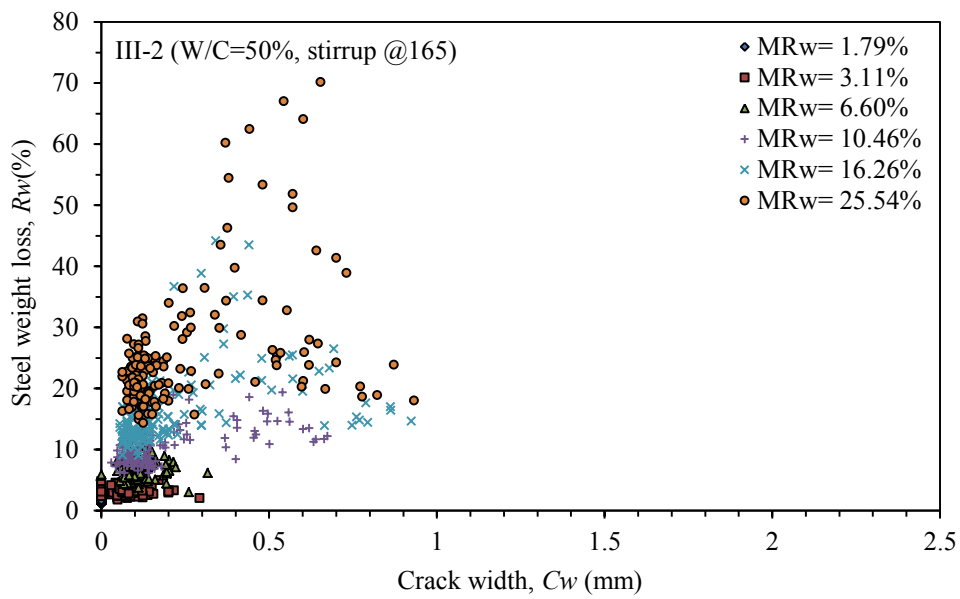
Fig. 34 Relationship between the steel weight loss and crack width of specimen III-2.

4.7 Effect of spatial variability of steel corrosion on cracking behavior of RC beams

Using the grid line system and photographs of the crack growth at several damaging stages, the cracking patterns on one side surface of the beam could be determined. To investigate the structural behavior of each beam with different corrosion damages, graphs of the spatial variability in the steel weight loss and surface crack widths, including the X-ray image of the steel corrosion and photograph of the corrosion cracking, are provided along with an illustration of the cracking pattern in Figs. 35-39. Figs. 35b, 36b, 37b, 38b, and 39b indicate that each beam has a very different spatial distribution of steel weight loss over its rebar length although they were all corroded under similar conditions. It is well-known that the spatial variability of steel corrosion is caused by a number of parameters (e.g., randomness in concrete material and steel reinforcement properties, concrete cover, cracks, workmanships, etc.) which are very difficult to control or measure. Consequently, very different corrosion patterns of the reinforcing rebars were found in the RC structures or members under both exposed conditions of natural corrosion (Palsson and Mirza 2002; Akiyama et al. 2016) and accelerated corrosion (Kashani et al. 2013, Zhang et al. 2014). However, for small-size beams in this controlled experiment, it is more likely that the randomness of concrete properties (e.g., different distributions of voids at the interfacial zones between the steel surface and concrete, as reported in Page (1975) and Page (1982) might be the cause to induce different spatial variability in steel weight loss from one beam to another.

The cracking pattern of the beam I-1 in Fig. 35(a) depicts a flexural failure mode. During the loading test at approximately $P = 13.5$ kN, it was observed that two cracks at 580 mm and 610 mm widened rather quickly, causing the deflection to accelerate. As the load increased to 15.4 kN, another crack widened approximately at 740 mm prior to the concrete being crushed. By comparing Figs. 35(a), 35(b) and 35(c), it can be noted that

these three localized cracks occurred close to the local maxima of the steel weight loss (i.e., Rw of 26.06%, 30.59%, and 26.93% at 580 mm, 620 mm, and 760 mm, respectively) and the corrosion cracks (i.e., Cw of 0.80 mm and 1.05 mm at 600 mm and 740 mm, respectively). These results strongly suggest that the corroded reinforcement had strain localizations and yielded at the corrosion pits of these local maxima, thus causing onset cracks, a rapid shift in the neutral axis to the top, and the crush of concrete.

The cracking behavior of the beam II-1 in Fig. 36(a) indicates that this beam also failed in flexure. It can be noted that the beam only had a few cracks, which were clearly dominated by a large longitudinal splitting crack alongside the embedded rebar in the mid-span. At a load P of approximately 16 kN, the splitting crack widened rather quickly and caused the deflection to accelerate, which suggests that the reinforcement yielded. Then, the concrete was crushed at approximately P = 19 kN. The large splitting crack implies a severe bond loss within the loading span, which is partly due to the lowest confinement of the largest stirrup spacing in this region and partly due to the remarkable loss of the rebar ribs and large cover cracking (i.e., over 1.79 mm) at the bottom side from 650 mm to 1030 mm, as indicated in Figs. 36(b) and 36(c). The effects of the confinement levels and cracking on the bond performance of the corroded RC members have been reported in previous studies (Fang et al. 2006; Lundgren 2007).

The cracking pattern of the beam II-2 is illustrated in Fig. 37(a). When the load increased to approximately 15 kN, the two flexural cracks at 590 mm and 680 mm and another splitting crack at the mid-height become onset and increased in size until the concrete was crushed at approximately P = 17 kN, which suggests the flexural failure mode of the beam. The onset splitting crack at the mid-span implies an impaired steel-concrete bond in the loading span due to the internal concrete damage induced by the expansive corrosion product. Furthermore, by comparing Figs. 37(a) and 37(b), it can be observed that one of the flexural cracks occurred close to the local maxima of the steel

57

weight loss Rw = 25.45% at about 690 mm.

The cracking behavior of the beam III-1 in Fig. 38(a) clearly demonstrates a bond failure mode before the concrete was crushed. After the first crack appeared in the mid-span, several other subsequent cracks developed extensively in the shear spans. The occurrence of these cracks was most likely dependent on the local maxima of the steel weight loss, which occurred out of the loading spans, as indicated in Fig.38(b). When the load reached approximately14 kN, the splitting cracks occurred suddenly and propagated rapidly in the longitudinal direction from the mid-span till the end of the left support, causing a large portion of the concrete to fall down. This long splitting crack suggests that the beam suffered from a severe steel-concrete bond loss, which may be attributed to the large corrosion amount (MRw = 27.23%) and a low confinement of the plain concrete without stirrups. Thereafter, up to a load of 15 kN, the primary cracks at 550 mm, 970 mm, and 1030 mm widened relatively rapidly in the shear span until the top compressed concrete was crushed at 610 mm.

Fig. 39(a) illustrates that the beam III-2 exhibited a shear failure mode in a brittle manner due to the rupture of the longitudinal reinforcement in the shear span. During the test, at a load of approximately 7.2 kN, the primary crack at 520 mm and mid-span deflection increased rather rapidly, which indicated that the corroded rebar yielded. Then, as the load reached 8.7 kN, the rupture of the reinforcement occurred at 490 mm, leading to a sudden collapse of the beam. This rupture of the corroded reinforcement was due to its highly localized corrosion pit in the shear span with Rw = 70.18% at 490 mm, as indicated in Fig. 39(b), and the larger corrosion cracking over 0.25 mm between 443 mm to 660 mm, as indicated in Fig. 39(c).
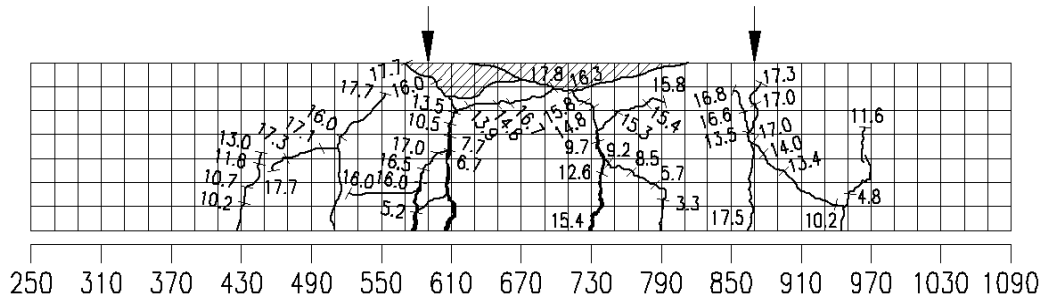
(a) Cracking pattern of beam I-1
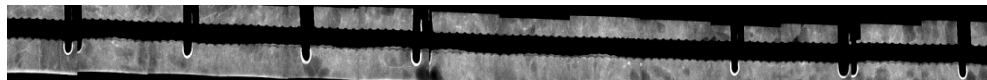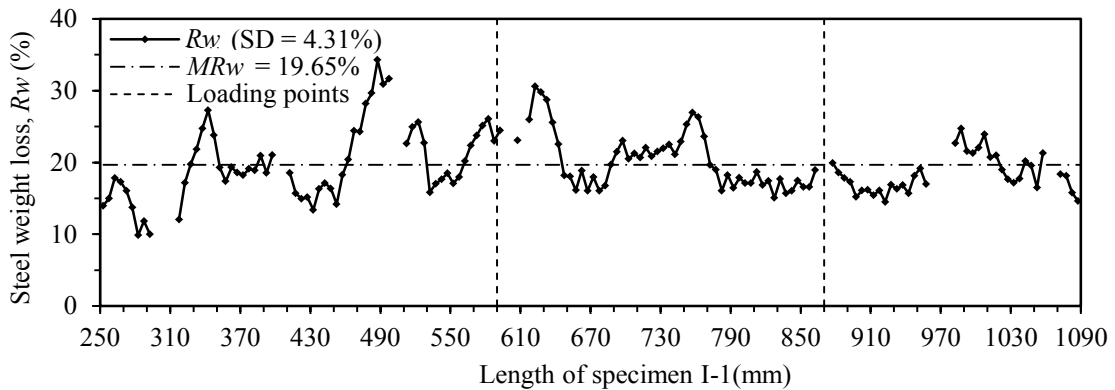
(b) Spatial variability in the steel weight loss and X-ray image of the steel corrosion at 180°
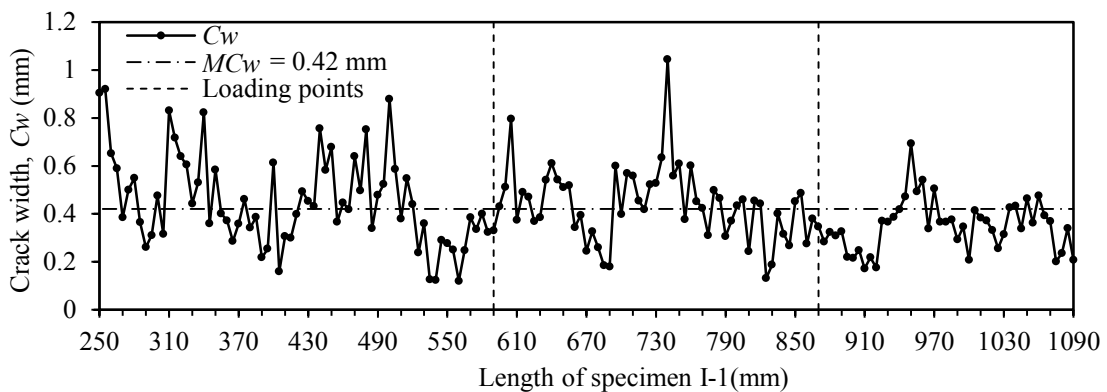
(c) Spatial variability in the surface crack widths and photos of the corrosion cracking

Fig. 35 (a) Cracking pattern; (b) spatial variability in the steel weight loss and X-ray image of the steel corrosion at 180°; and (c) spatial variability in the surface crack widths and photo of the corrosion cracking for beam I-1
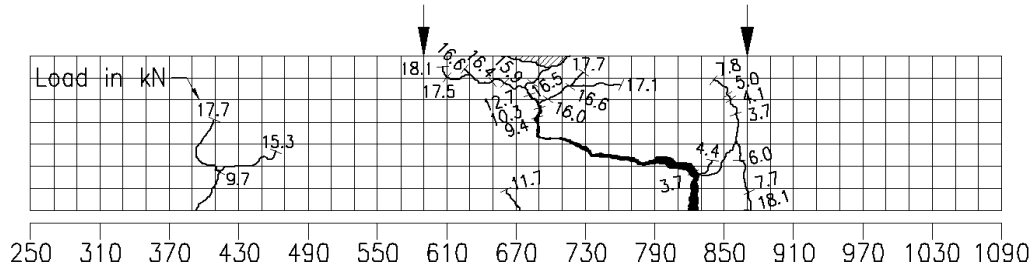
(a) Cracking pattern of beam II-1
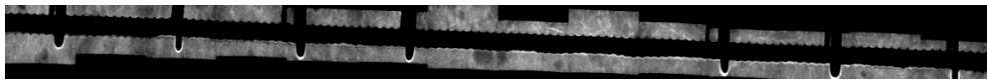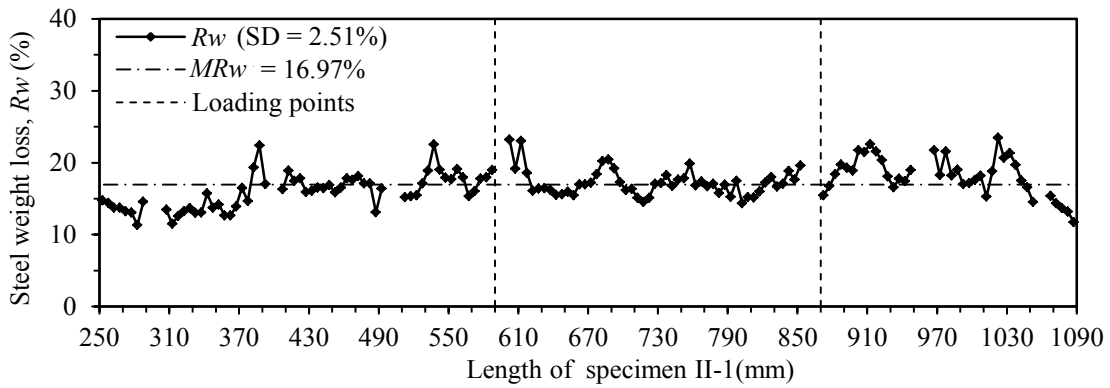
(b) Spatial variability in the steel weight loss and X-ray image of the steel corrosion at 180°
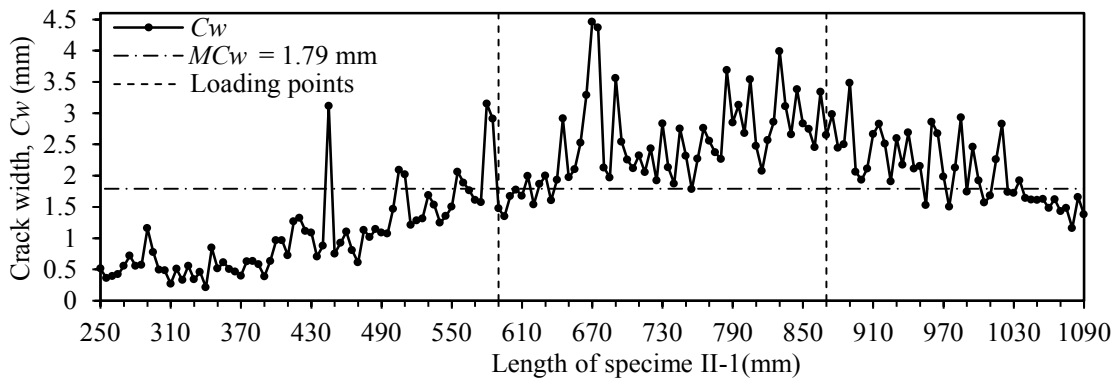
(c) Spatial variability in the surface crack widths and photos of the corrosion cracking

Fig. 36 (a) Cracking pattern; (b) spatial variability in the steel weight loss and X-ray image of the steel corrosion at 180°; and (c) spatial variability in the surface crack width and photo of the corrosion cracking for beam II-1
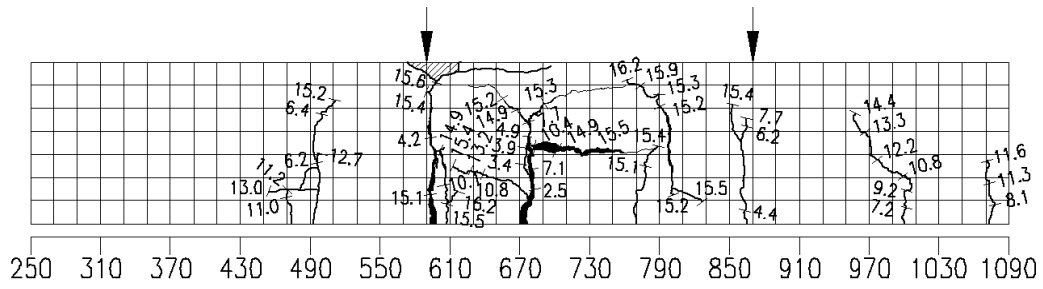
(a) Cracking pattern of beam II-2
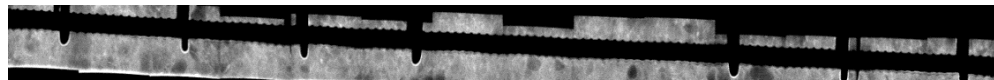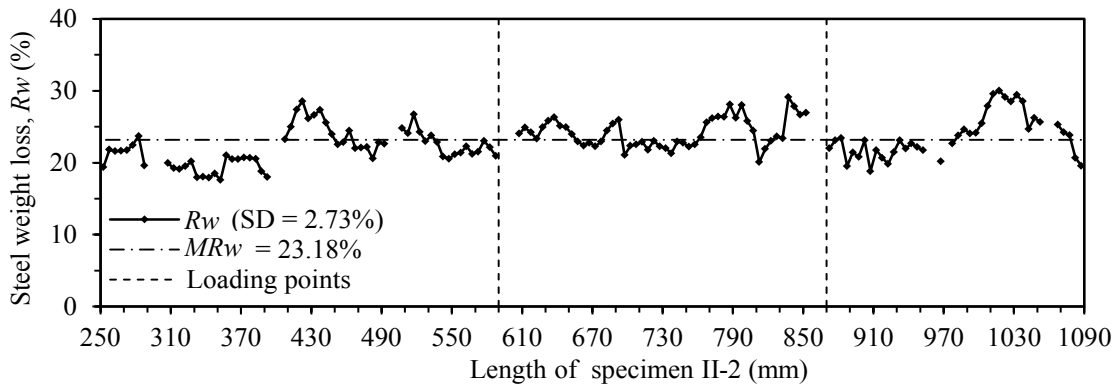
(b) Spatial variability in the steel weight loss and X-ray image of the steel corrosion at 180°
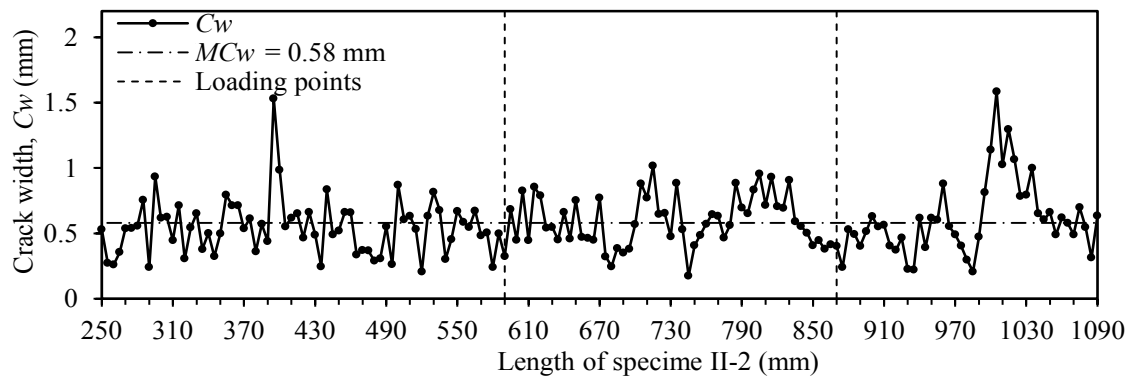
(c) Spatial variability in the surface crack widths and photos of the corrosion cracking

Fig. 37 (a) Cracking pattern; (b) spatial variability in the steel weight loss and X-ray image of the steel corrosion at 180°; and (c) spatial variability in the surface crack widths and photo of the corrosion cracking for beam II-2
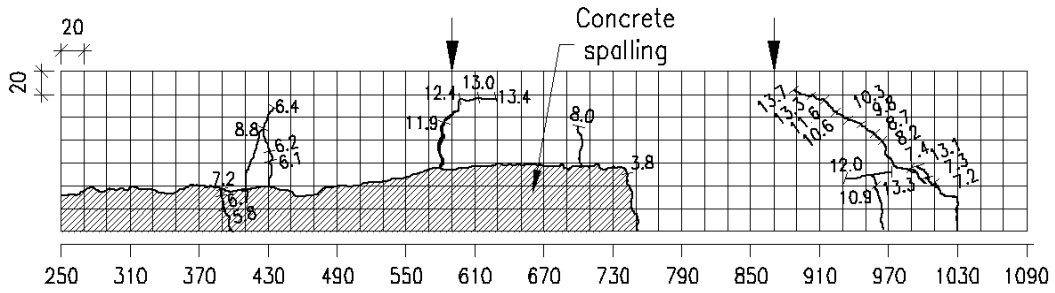
(a) Cracking pattern of the beam III-1
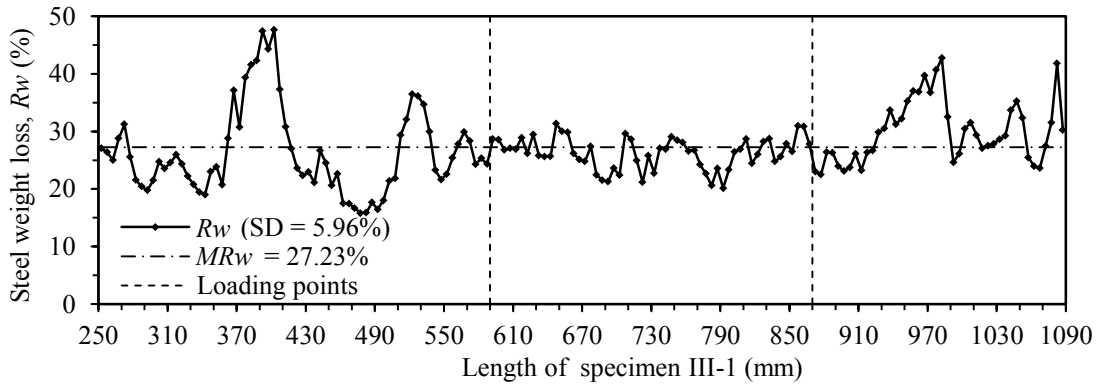
(b) Spatial variability in the steel weight loss and X-ray image of the steel corrosion at 180°
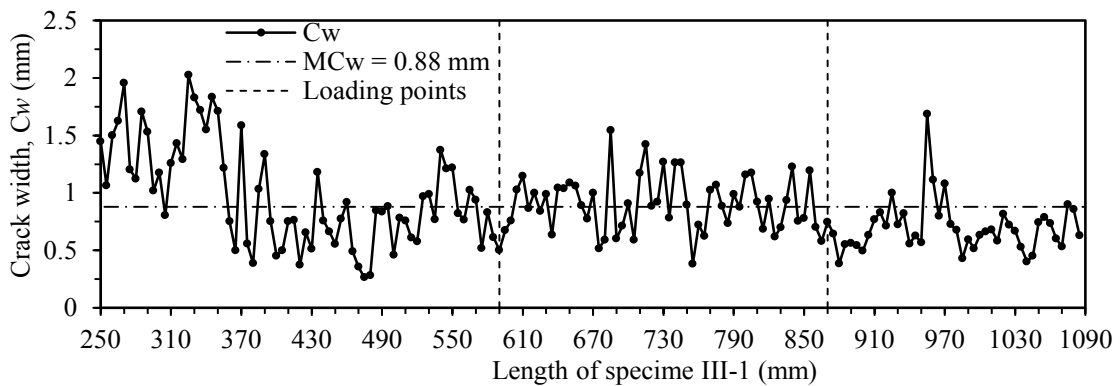
(c) Spatial variability in the surface crack widths and photos of the corrosion cracking

Fig. 38 (a) Cracking pattern; (b) spatial variability in the steel weight loss and X-ray image of the steel corrosion at 180°, and (c) spatial variability in the surface crack widths and photo of the corrosion cracking for beam III-1
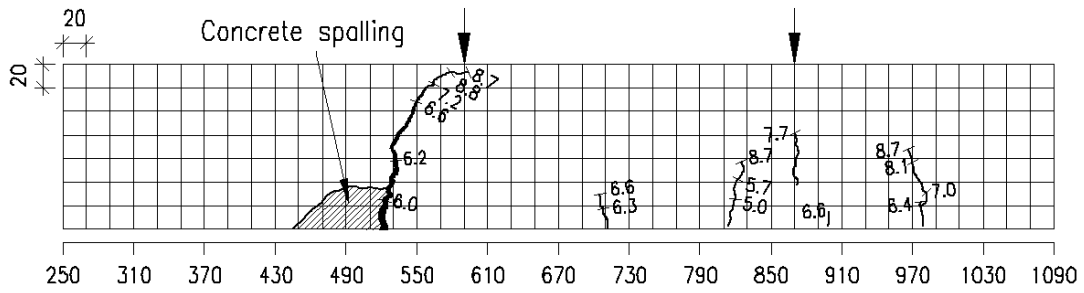
(a) Cracking pattern of beam III-2
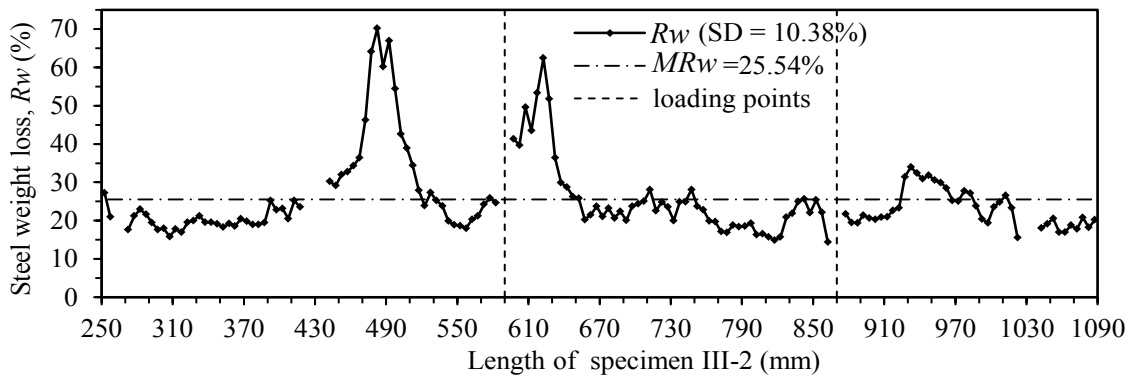
(b) Spatial variability in the steel weight loss and X-ray image of the steel corrosion at 180°
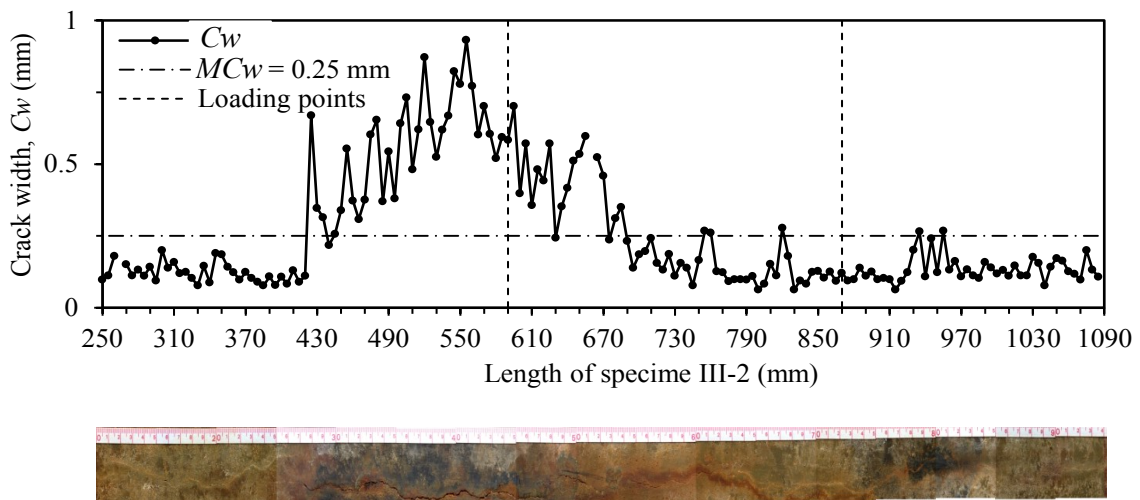
(c) Spatial variability in the surface crack widths and photos of the corrosion cracking

Fig. 39 (a) Cracking pattern; (b) spatial variability in the steel weight loss and X-ray image of the steel corrosion at 180°; and (c) spatial variability in the surface crack widths and photo of the corrosion cracking for beam III-2

4.8 Effect of spatial variability of steel corrosion on flexural responses of RC beams

Figs. 40 and 41 depict the flexural load-deflection P-δ responses for all the corroded beams. The ultimate loads ($P_{u,exp}$) of the test beams are explicitly provided in the tables along with the global mean values (MRw) and standard deviations (SD) of their steel weight loss distributions. It should be noted that the deflection could not be recorded after the occurrence of concrete spalling at the mid-span for certain tests. Due to this reason, the ultimate loads of the P-δ curves in the graphs are occasionally different from those provided in the table, and the effects of variability of steel corrosion on the ductility of the beam is not discussed herein.

Fig. 40 illustrates the flexural responses of the first group of beams, I-1, II-1, and II-2, with different W/C ratios, i.e., 50%, 40%, and 65%, respectively. The overall responses of this group suggest that it is not the concrete strength but the corrosion amount of each beam that has a more significant influence on their load bearing capacities. In the case of a small variability in the steel corrosion (i.e., a SD below 4.3%), the loading capacities (i.e., $P_{u,exp}$ = 19.19 kN, 18.05 kN, and 16.99 kN) of the deteriorated beams II-1, I-1, and II-2 decrease with the increasing global mean steel weight loss (i.e., MRw = 16.97%, 19.65%, and 23.18%, respectively).

Fig. 41 illustrates the flexural reposes of the second group of corroded RC beams, I-1, III-1, and III-2. By comparing the flexural responses of the beam I-1 with stirrups and the beam III-1 without stirrups, it can be inferred that the stirrup confinement has a significant effect on the bond performance of the corroded beams because the bending stiffness of the beam I-1 is larger than that of the beam III-1. For the beams I-1 and III-2 that have stirrups, the beam III-2, which as a larger stirrup spacing, exhibits a significantly larger brittle behavior than the beam I-1, which has a smaller stirrup spacing. Furthermore, it should be noted that the corrosion level of the beam III-1 (MRw = 27.23%) is slightly
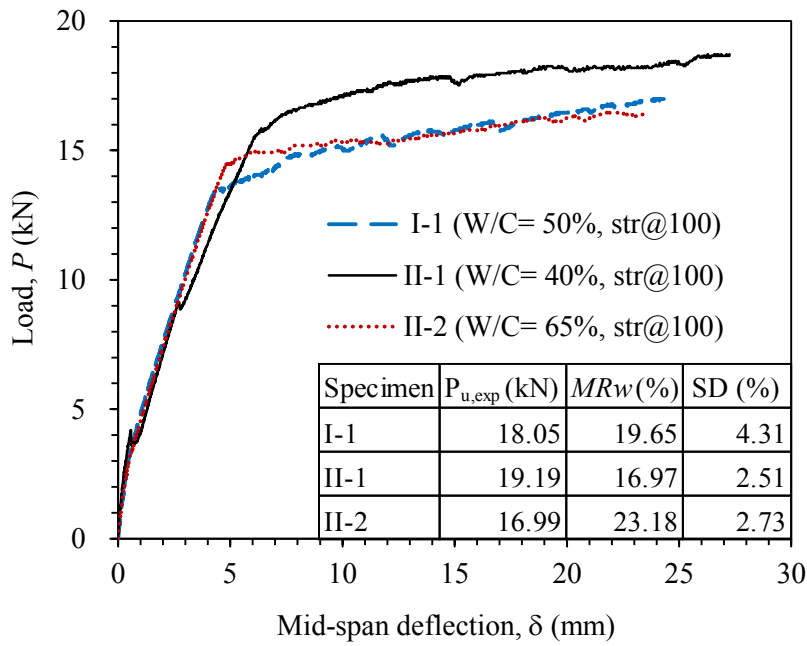
Fig. 40 Load-deflection responses of the corroded beams with different water-cement ratios.
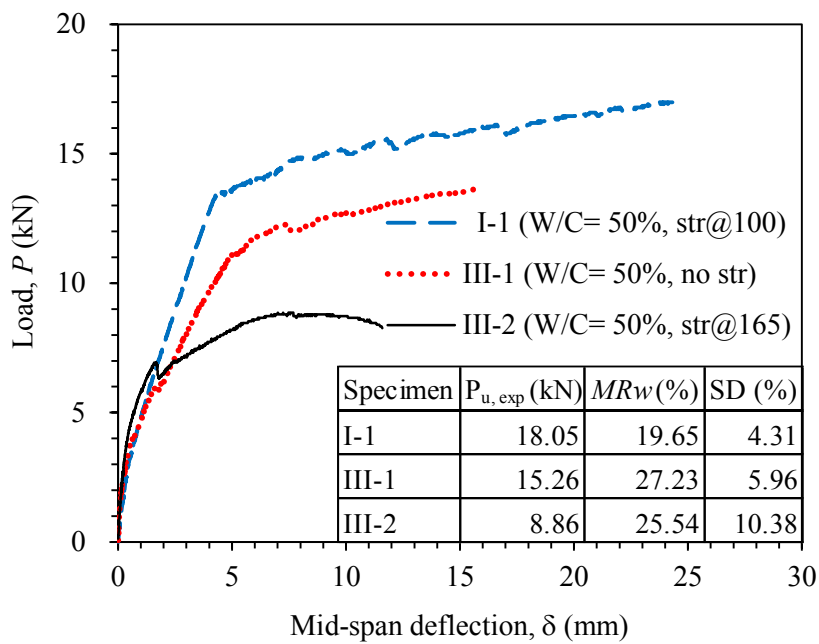
Fig. 41. Load-deflection responses of the corroded beams with different stirrup spacings

greater than that of the beam III-2 (MRw = 25.54%) and considerably larger than that of

the beam I-1 (MRw = 19.65%). However, the loading capacity of the beam III-1 ($P_{u,exp}$ =

15.26 kN) is considerably larger than that of the beam III-2 ($P_{u,exp}$ = 8.86 kN) and only relatively smaller than that of the beam I-1 ($P_{u,exp}$ = 18.05 kN). In fact, the loading capacities of the beams I-1, III-1, and III-2 (i.e., $P_{u,exp}$ = 18.05 kN, 15.26 kN, and 8.86 kN, respectively) decrease as their SD of the steel weight loss increases (i.e., SD = 4.31%, 5.96%, and 10.38%, respectively). Torres-Acosta et al. (2007) also found that the maximum corrosion pits, rather than the average steel-cross section, are the more important parameter that affects the flexural load capacity.

The experimental results in this study suggest that for a small dispersion in the steel weight loss (i.e., a SD below 4.3%), the mean steel weight loss or corrosion level instead of the corrosion pits appear to have a dominant effect on the loading capacity of the corroded beams. However, as the dispersion in the steel cross-section loss increases, the influence of the pitting corrosion on the loading capacity becomes more significant than the corrosion level.

Chapter 5: Assessment of structural performance of corroded RC members

5.1 FE analysis of corrosion-affected RC beams

5.1.1 Two-dimensional FE modeling of corroded RC beams

Fig. 42 illustrates a two-dimensional finite element model used to simulate the responses of the corroded beams via Diana finite element analysis version 9.5 of TNO (2014). The concrete was modeled using four-node plane stress elements with sizes of primarily 10 mm × 10 mm since this mesh size allows a convenient identification of distinct cracks through visualization of the cracked concrete elements without the need to introduce discontinuities to the FE models, according to Kallias and Rafiq (2010). The thickness of all concrete elements are equal to the beam width. The steel reinforcement is modeled as two-node truss bar elements, and the steel-concrete bond is modeled as a line interface element with a zero thickness. The material constitutive of concrete in Fig. 43(a) proposed by Kallias and Rafiq (2010) was used in this study. A total strain-based rotating smeared crack model was used for the incremental stress-strain relationship of concrete. The non-linear tension softening curve of Hordijk was used to represent the tensile behavior of concrete with the combination of the crack bandwidth h and the tensile fracture energy G_f. All of the input parameters, including the concrete tensile strength f_t and the tensile fracture energy of concrete G_f, were derived based on CEB (1993) using the compressive strength of concrete. The compression behavior of concrete was modeled following a parabolic curve, where the linear-elastic relationship was maintained until 30% of the compressive strength and post-peak curve was associated with the compressive fracture energy G_c (Nakamura, 2001). On the other hand, the stress-strain constitutive relation of rebar was expressed by a simplified bilinear shape, as indicated in Fig. 43(b). The perfect

and deteriorated bond slip relations were modeled based on CEB (1993) and Kallias and Rafiq (2010), respectively, as indicated in Fig. 43(c).

5.1.2 Modeling the corrosion damage on the steel reinforcement

Previous studies (Cairns et al. 2005; Du et al. 2005a; Du et al. 2005b) reported that both strength and ductility were affected mainly due to variability in steel cross-section loss over their lengths. Due to the difficulty in implementing the actual variability of steel corrosion in the numerical model, an alternative approach was suggested by modeling the corroded steel rebar over a length based on average cross-section loss together with empirical coefficients. The use of empirical coefficients (whose values are smaller than 1) is to account for the reduction in strength and ductility of corroded rebar attributed to the irregular cross-section loss along the rebar length in addition to the reduction attributed to the average cross-section. However, in this paper, since the local corrosion damage on the rebar is considered in the FE model by reducing the steel cross-sectional

(a) two-dimensional FE model of the half-beam

(b) Assumed cross-sectional area distribution over a half-length corroded rebar
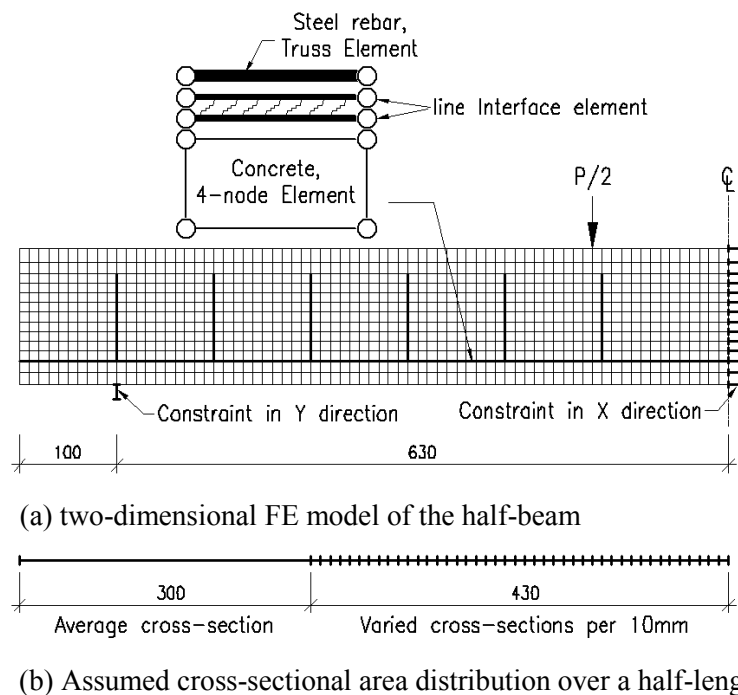
Fig. 42 Details of the FE model: (a) two-dimensional FE model of the half-beam and (b) assumed cross-sectional area distribution over a half-length corroded rebar
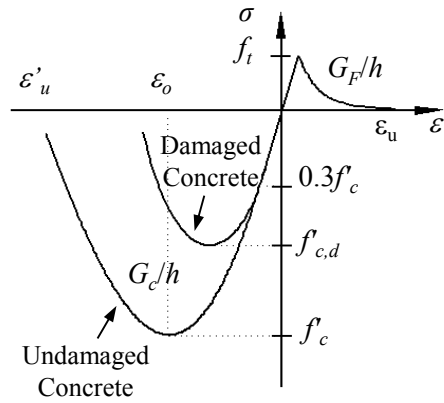
(a) Stress-strain relationship of concrete
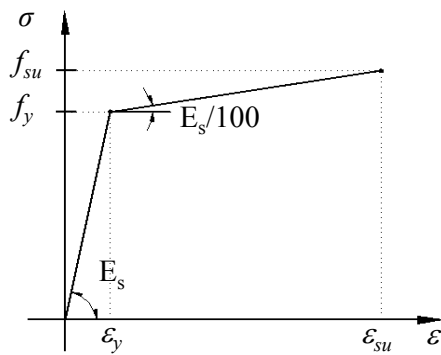
(b) Stress-strain relationship of the steel reinforcement
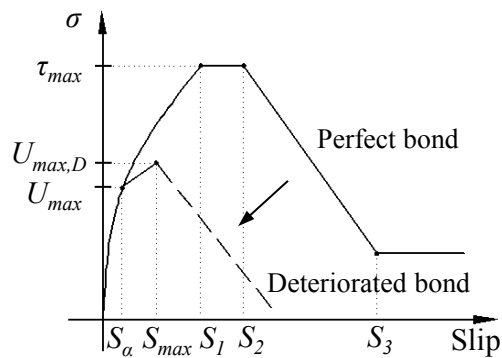
(c) Bond stress-slip relationship

Fig. 43 Material constitutive models of (a) concrete in compression and tension; (b) steel reinforcement; and (c) bond stress-slip relationship

areas over the rebar length according to experimental data of steel weight loss, the simplified bilinear constitutive stress–strain relationship of steel depicted in Fig. 43(b) is

used without empirical coefficients.

To investigate the effects of the distribution of the cross-sectional area over a rebar length on the computational result, non-uniform and uniform cross-sectional areas of the rebar have been used. Fig. 42(b) illustrates the cross-sectional area over the rebar length for the case where the non-uninform cross-sectional area is used. The spatial variability associated with the reduced cross-sectional area of the rebar was modeled by varying the cross-sectional area in each steel truss element with a length of 10 mm (i.e., 300–1080 mm from the left side of the specimen) based on the local steel weight loss Rw estimated from the X-ray photogram; the average cross-sectional area was used for the remaining truss bar elements at other locations (i.e., 0 mm to 300 mm from the left side of the specimen) where the X-ray photogram was not taken. For the FE analysis with the uniform cross-sectional area of the rebar, all of the rebar elements have the same average cross-sectional area.

5.1.3 Modeling the corrosion damage on concrete

The expansion of the corrosion products caused the cracking and spalling of concrete. Consequently, the concrete region that was damaged by corrosion exhibited a reduced performance compared to that of the undamaged concrete regions. The corrosion damage on the concrete cover was considered in the FE model by modifying the stress–strain relationship of the concrete, as suggested by Coronelli and Gambarova (2004). The deterioration of the concrete's compressive strength can be expressed:

$$f'_{c,d} = f'_c / [1 + k'(\varepsilon_1 / \varepsilon_o)] \tag{18}$$

where $f'_{c,d}$ is the compressive strength of the corroded concrete; f'_c is the compressive strength of the non-corroded concrete, $k' = 0.1$; ε_o is the strain at the compressive strength; f'_c and ε_1 is the average smeared tensile strain in the transverse direction. The strain ε_1 can

be estimated as:

$$\varepsilon_1 = (b_f - b_o)/b_o \tag{19}$$

where b_o is the section width in the virgin state (no corrosion cracks); and b_f is the beam width increased by corrosion cracking.

$$(b_f - b_o) = n_{bars} w_{cr} \tag{20}$$

where n_{bars} is the number of rebars; and w_{cr} is the total crack width at a given corrosion level. The total crack width w_{cr} can be determined by Molina et al. (1993) as:

$$w_{cr} = 2\pi(v_{rs} - 1)X_d \tag{21}$$

where v_{rs} is the ratio between the specific volumes of rust and steel; and X_d is the depth of the penetration attack. In this study, v_{rs} is assumed to be 2 (Monila et al. 1993).

5.1.4 Modeling the corrosion damage on bond

The residual bond stress-slip curve, as proposed by Kallias and Rafiq (2010), is used herein for the deteriorated steel-concrete bond interface element, and the well-known bond stress-slip relation in CEB (1993) is used to model the perfect bond between steel and concrete, as indicated in Fig. 43(c). The residual bond-slip relationship can be described as:

$$U = U_1(S/S_1)^{0.3} \tag{22}$$

$$S_\alpha = S_1(\alpha' U_{max}/U_1)^{1/0.3} \tag{23}$$

$$S_{max} = S_1 \exp[(1/0.3)Ln(U_{max,D}/U_1)] + S_o Ln(U_1/U_{max,D}) \tag{24}$$

where $\alpha' = 0.7$; $U_1 = 2.57(f'_c)^{0.5}$, $S_1 = 0.15c_o$ where $c_o = 8.9$ mm is the spacing between the

ribs of the steel bar; $S_2 = 0.35c_o$; and $S_o = 0.15$ or 0.4 mm for plain concrete or steel confined concrete, respectively. $U_{max,D}$ is the residual bond strength, which can be determined according to Maaddawy et al. (2005):

$$U_{\max,D} = R[0.55 + 0.24(c/d_b)]\sqrt{f'_c} + 0.191(A_{st}f_{yt}/S_s d_b) \tag{25}$$

$$R = A_1 + A_2 m_L \tag{26}$$

where c is the concrete cover; d_b is the diameter of the longitudinal bar; A_{st} is the cross-section area of the stirrup; f_{yt} is the yield strength of the stirrup; S_s is the stirrup spacing; R is the factor accountable for the residual contribution of concrete towards the bond strength as a function of $A_1 = 0.861$ and $A_2 = -0.014$, which is related to the corrosion current used in the accelerated corrosion test; and m_L is the amount of steel weight loss in percentage, which is equivalent to MRw herein. Eq. (25) consists of two separate terms: the first and second terms are attributed to the concrete and stirrup contributions to the bond strength, respectively. The effectiveness of this equation is that the level of confinement can be varied with the changes in the stirrup spacing and concrete compressive strength for different specimens.

5.1.5 Computational results of FE analysis

To verify the accuracy of the FE model used in this paper, the flexural P-δ responses of the simulated beams are compared to those of the test beams, as indicated in Figs. 44–47. Generally, the flexural P-δ responses obtained from the FE method using both the mean and varied cross-sections as inputs overestimate the flexural responses of the experimental tests in all cases. The stiffness of the simulated beams is larger than those of the test beams throughout the evolution of damaging stages because their slopes of the P-δ curves are steeper than those of the test beams in both the pre- and post-peak regions. Nevertheless, regardless of the different input parameters, Figs. 44–47 demonstrate that

the FE method provides better predictions of the flexural responses for those corroded RC beams that have a smaller variability in the local steel cross-section loss. The differences in the bending stiffness between the numerical and test results for the beams
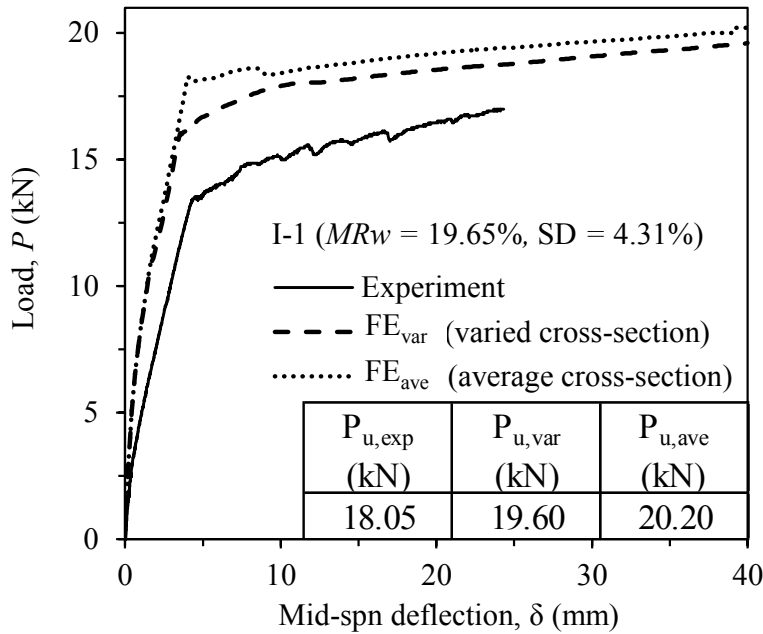
Fig. 44 Experimental versus FEM results for the flexural responses of beam I-1.
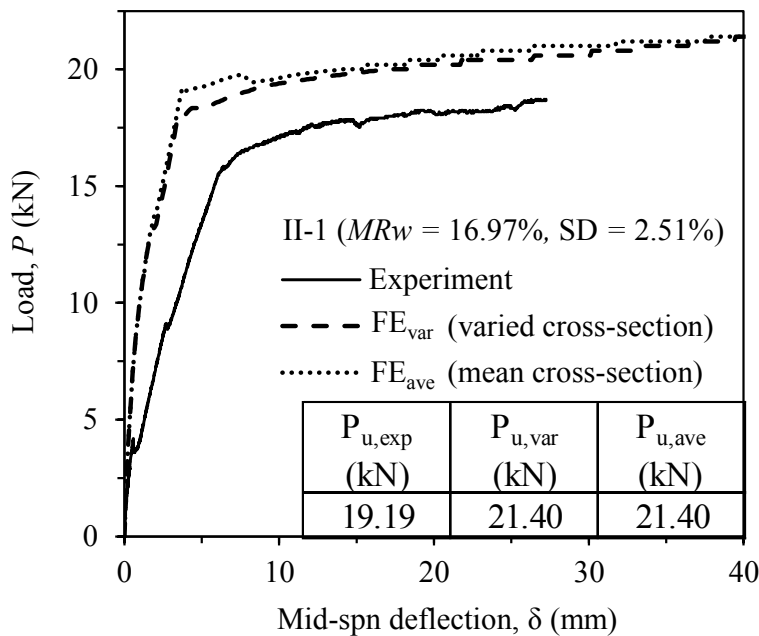
Fig. 45 Experimental versus FE results for the flexural responses of beam II-1.
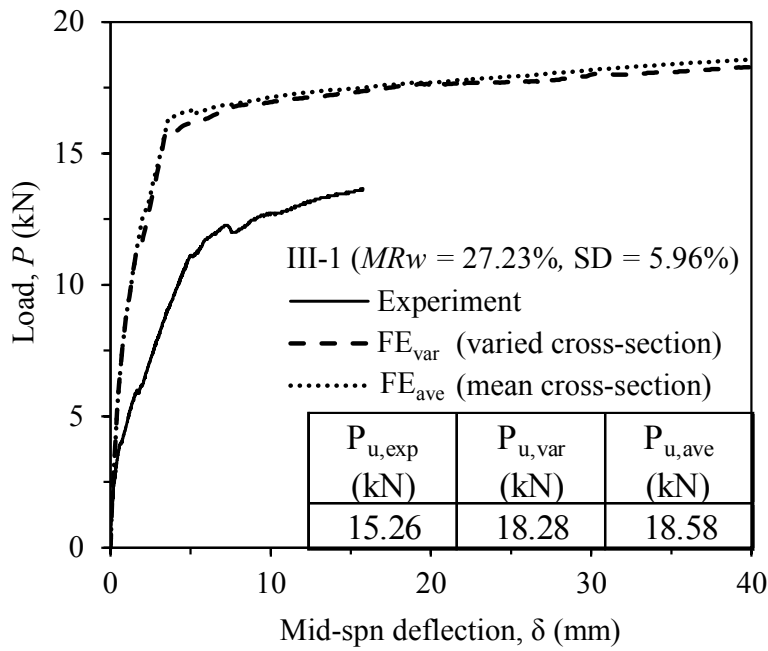
Fig. 46 Experimental versus FE results for the flexural responses of beam III-1.
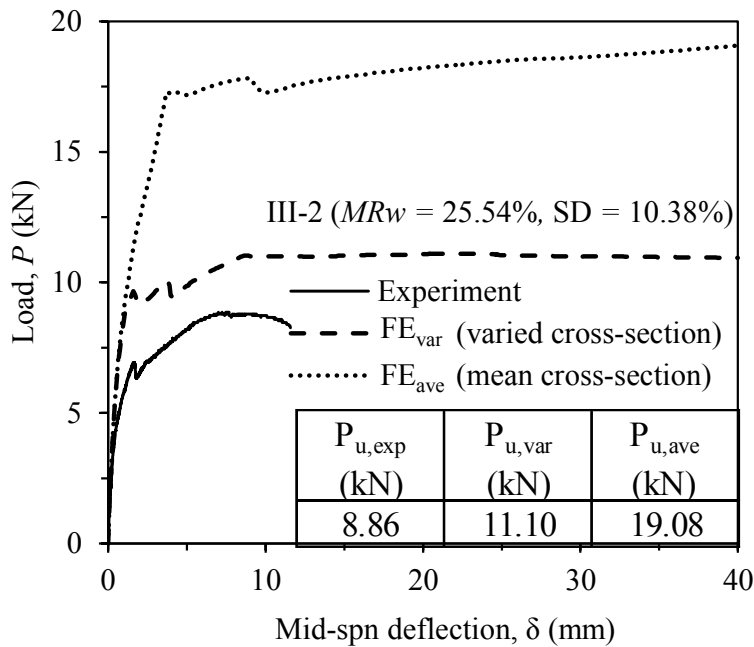
Fig. 47 Experimental versus FE results for the flexural responses of beam III-2

I-1, II-1, and II-2, which have a SD below 4.5%, are not as large as those of the beams

III-1 and III-2, which have a SD greater than approximately 6%. Moreover, the predicted ultimate loads of the beams are in good agreement with those of the test beams, except for those of beams III-1 and III-2 (with a SD over about 6%), which are quite different from the results of the test beam. In terms of different input parameters, it should be noted that the FE model using an input of varied steel cross-sectional areas Avar provides better predicted results compared to other models using an input of only the mean steel cross-sectional loss A_{ave}, especially for the case of beam III-2, whose variability in the steel weight loss is rather larger (i.e., SD over 10%). For the beams I-1, II-1, II-2, and III-1, which have a SD below 6%, the differences between the results of the simulated beam with inputs of A_{var} and A_{ave} are slightly different, as indicated in Figs. 44–47. However, for the beam III-2 whose SD is over 10%, Fig. 47 indicates that there is a large difference between the simulated responses of the beams when using the inputs of A_{var} and A_{ave}. The simulated beam that uses the varied steel cross-sectional areas A_{var} provided a considerably better prediction of the flexural response than the other beam, which used only the mean value of the steel cross-sectional areas A_{ave}.

Hence, the results of the FE model suggest that it is necessary to consider the effects of the spatial variability in the steel weight loss to assess the structural behavior of RC corroded beams if the variability in the steel cross-section reduction becomes larger (e.g., for a SD between 6% and 10% in this study). Although the FE model overestimates the bending stiffness for all of the cases, it still provides a good estimation of the loading capacity for corroded beams. The overestimation of the bending stiffness in both the pre- and post-peak regions may occur because the spatial variability in the bond deterioration was not considered in the FE model. More studies on this topic are needed for further improvements in FE modeling.

5.2 Reliability analysis of corroded RC beams considering spatial variability of steel corrosion

5.2.1 Gumbel statistics of extreme values

To assess the long-term structural performance of the corroded RC members, it is necessary to consider the spatial variability in the steel corrosion along the corroded RC members. Ignoring the effects of the spatial variability can lead to an overestimation of the probability of failure (Stewart 2004; Stewart and Al-Harthy 2008; Val 2007; Stewart 2009; Stewart and Suo 2009). Therefore, modeling the spatially varied cross-sectional areas over the length of the corroded RC members is important for evaluating a long-term structural performance precisely.

Chloride iron, by nature, causes local breakdowns on the passive film at the rebar surface if its concentration reaches a critical threshold at the rebar depth. Consequently, it generates localized or pitting steel corrosion with highly varied cross-sectional areas over the rebar length. Due to this characteristic of highly localized steel cross-section loss, which might result in a risk of a sudden failure of the structures, several researchers have used Gumbel statistics of extreme values to model spatial variability of steel corrosion. One research group (Stewart 2004; Stewart and Al-Harthy 2008; Val 2007; Stewart 2009; Stewart and Suo 2009) proposed the Gumbel distribution of a pitting factor $R_p = p_{max}/p_{av}$, where p_{max} and p_{av} are the maximum and the average pitting depths, respectively. However, another group (Zhang et al. 2014) suggested the use of a cross-sectional area spatial heterogeneity factor $R_A = A_{ave}/A_{min}$, where A_{ave} and A_{min} are the average and the minimum cross-sectional areas, respectively. The former group assumed that R_p is time-invariant, thus ignoring the effects of the corrosion amount on its distribution while mentioning that the distribution parameters of R_p should be used carefully because R_p was observed to decrease with time. Conversely, the second group (Zhang et al. 2014) determined that the Gumbel distribution parameters μ and α increase linearly with the corrosion amounts.

Therefore, the manner in which the amount of corrosion affects the Gumbel parameters has not been well established. Furthermore, it should be noted that several studies (e.g., Zhang et al. 2014), which model the spatial variability in the steel corrosion based on the amount of corrosion, used the data on steel corrosion from different corroded rebars subjected to various amounts of corrosion rather than from the same corroded rebars.

Due to time consumption and difficulty in estimating geometrical shapes of residual cross-sectional area, the spatial steel corrosion is modeled in this research using the Gumbel distribution of the maximum steel weight loss ratio $R_{swl} = W_{max}/MRw$, where W_{max} is the local maximum steel weight loss per 50-mm intervals of a corroded rebar and MRw is the global mean steel weight loss at a given time of corrosion. Additionally, the effects of the amount of corrosion on the Gumbel distribution parameters for the same corroded rebar of five corroded beams is investigated. First, at six different corrosion amounts or MRw values, the W_{max} values were extracted from the variation in the steel weight loss data along the length of each beam at every 50 mm. Then, the R_{swl} values for each corroded rebar were determined and grouped based on the MRw values and sorted in ascending ith orders. The probability of the occurrence F_i that corresponds to the ith value of R_{swl} can be determined as follows:

$$F_i = i/(N+1) \tag{27}$$

where $i = 1,2,3,\ldots, N$ (N is the total number of R_{swl} per single corroded rebar). The probability density function (PDF) of the random variable $X = R_{swl}$ can be expressed according to Zhang et al. (2014) as follows:

$$f(x) = (1/\alpha)e^{-(x-\mu)/\alpha} \exp(-e^{-(x-\mu)/\alpha}) \tag{28}$$

where X is the random variable, and μ and α are the location and scale parameters of the Gumbel distribution, respectively. The parameters μ and α can be determined via the

expectation and variance of R_{swl} (i.e., $E(R_{swl})$ and $D(R_{swl})$) as follows:

$$E(R_{swl}) = \mu + \gamma\alpha \tag{29}$$

$$D(R_{swl}) = \pi^2\alpha^2 / 6 \tag{30}$$

where $\gamma = 0.5772$ is Euler's constant.

(a) Beam I-1

(b) Beam II-1

(c) Beam II-2

(d) Beam III-1

(e) Beam III-2
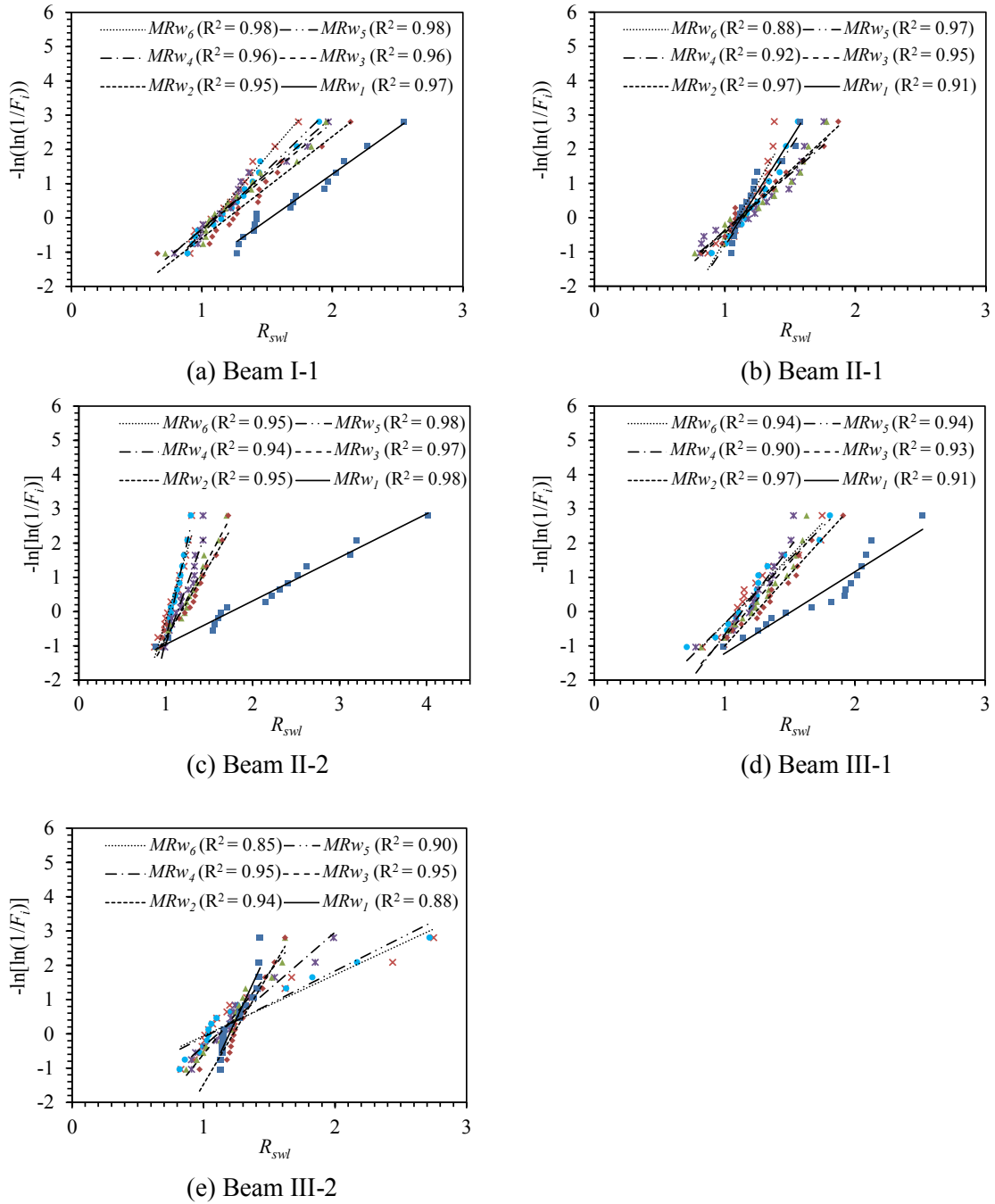
Fig. 48 Fitting the values of $-\ln[\ln(1/Fi)]$ with R_{swl}

To verify if R_{swl} can be characterized by the Gumbel distribution, the scattering plot of R_{swl} versus its corresponding values of $-\ln[\ln(1/F_i)]$ was constructed in Fig. 48 for all of the corroded beams. The Gumbel distribution fits extremely well to the R_{swl} values.

(a) Beam I-1

(b) Beam II-1

(c) Beam II-2

(d) Beam III-1

(e) Beam III-2
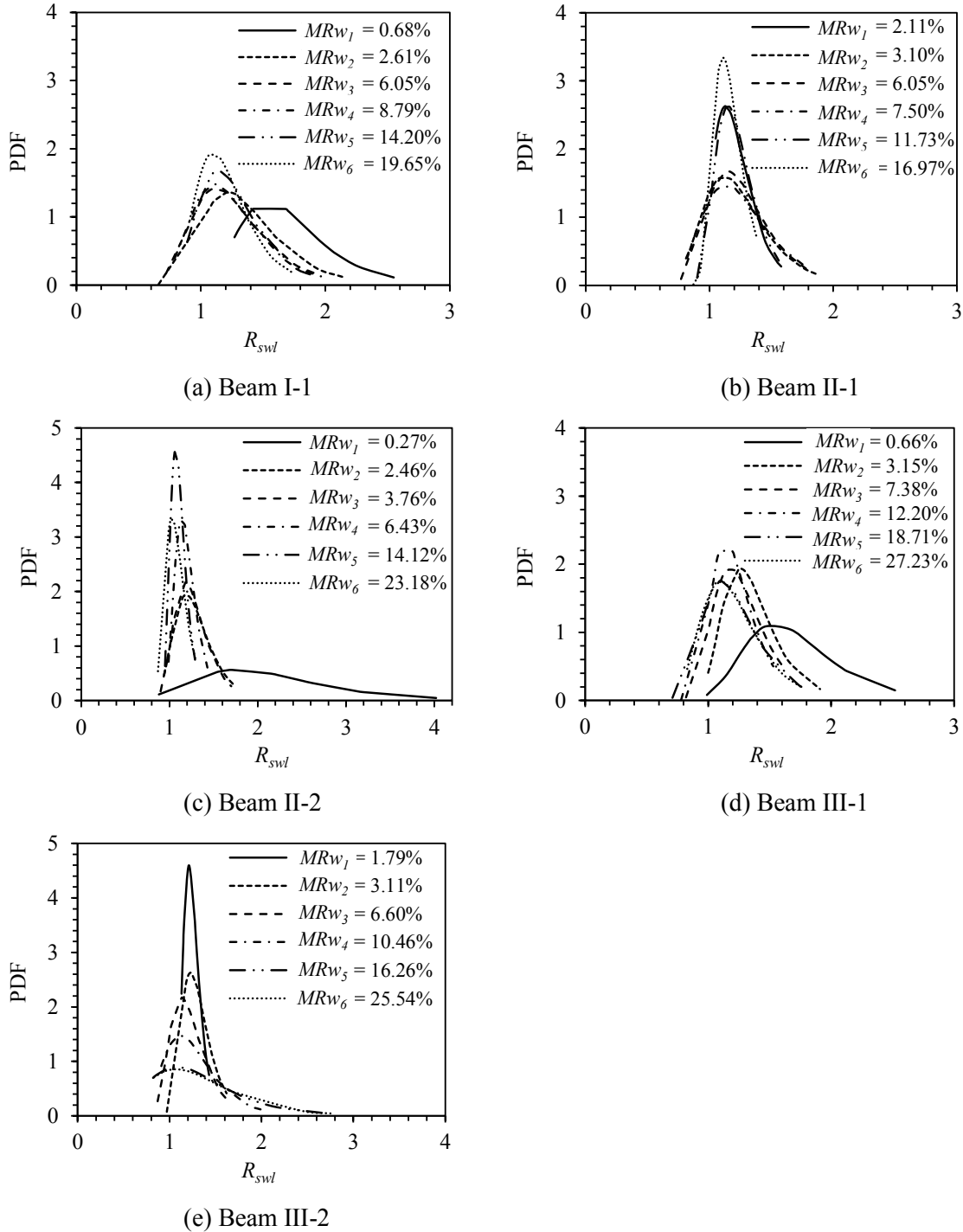
Fig. 49 Probability density function of R_{swl} at different global mean steel weight steel losses MRw.

These results prove that the Gumbel distribution parameters can be used to estimate the R_{swl} values. Therefore, the PDFs of R_{swl} for various amounts of corrosion (specified by the MRw values) for all of the beams are plotted in Fig. 49 to study the range over which the data of R_{swl} spreads. The PDFs of R_{swl} in Fig. 49 indicates that the R_{swl} data spreads in a range of approximately from 0.6 to 2.0.

5.2.2 Relationships between the average steel corrosion and Gumbel parameters

To study the effects of the amount of corrosion on the Gumbel parameters μ and α, scattering plots between the values of MRw and μ or α for all of the beams are illustrated in Figs. 50(a) and 50(b), respectively. Fig. 50(a) depicts a strong relationship between the Gumbel location parameter μ and the amount of corrosion, in which μ gradually decreases as MRw increases. For the relationship between the Gumbel scale parameter α and the amount of corrosion, Fig. 50(b) indicates a weak relationship due to a large scattering of the data points. Nevertheless, the scattering data points that accumulate below $\alpha = 0.30$ in Fig. 50 (b) suggest a good trend in their relationship, in which the Gumbel scale parameter α decreases as MRw decreases, and since the scattering data points are within a small range ($0.10 < \alpha < 0.30$), it can be reasonable to use the average line of the regression analysis provided in Fig. 50(b) to estimate the value of α.

(a)   (b)
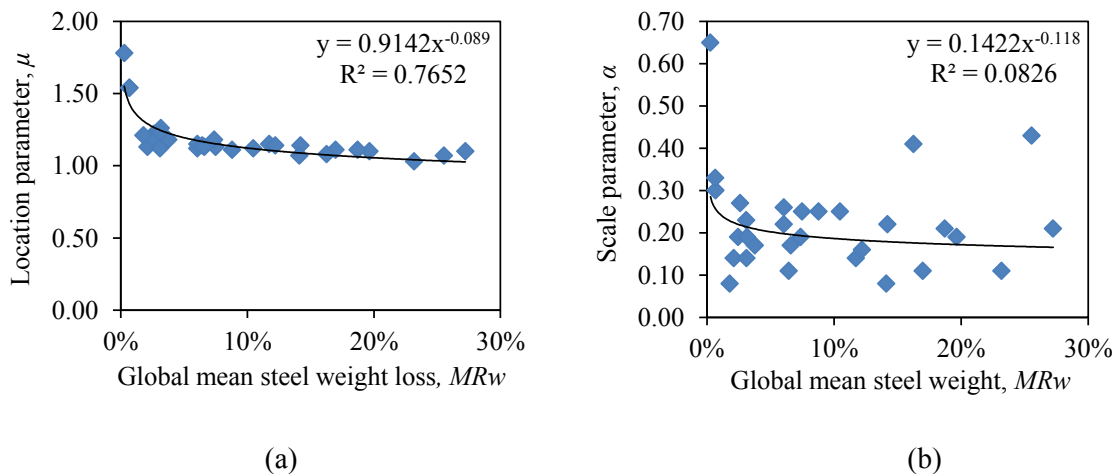
Fig. 50 Relationships between the Gumbel parameters of R_{swl} and MRw.

5.2.3 Illustrative example for application of *Rswl*

In this section, an example is illustrated to study the effects of the spatial and non-spatial steel corrosion on the failure probability of a corroded RC beam under flexure. Fig. 51 shows the configuration of the RC beam in question and its discretization into a series of elements along the beam length. The RC beam was singly reinforced with four deformed bars that have a diameter of 19 mm and simply supported with an effective span length of 6 m. The rebar has a grade of 60 with the yield strength of 420 MPa.

For the model of spatial steel corrosion, it is assumed that the middle part of the steel reinforcements in each element suffers from corrosion attack and their reduced cross-sectional areas are characterized by Gumble distribution. In the case that the spatial distribution is not considered, the failure probability is estimated by assuming that the magnitude of steel weight loss is spatially invariant over the entire beam length. Table 4 shows the statistics associated with other random variables (i.e., f'_c, f_y, d, and Q) which are used in Monte Carlo simulation (MCS) assuming that they are not spatially distributed. Since f_y is treated as a random variable following normal distribution, there is a possibility that certain random values of the yield strength of rebar f_y are smaller than the minimum yield strength 420 MPa according to the standard specification for deformed bars ASTM A615. In order to avoid this problem, a condition is set in the Monte Carlo algorithm such that the value of yield strength f_y in each sample is not smaller than or equal to 420 MPa.

Moreover, as mentioned in Section 5.2.2, since there is a large scatter of data points for between Gumbel scale parameter (α) and global mean steel weight loss (*MRw*) due to the fact that these two parameters are obtained from the corroded rebars of specimens which were made under different conditions (i.e., different water-cement ratios and stirrup spacing). Under these different conditions, it is very difficult to reduce the large scatter of the data points. To study the effect of the scale parameter on the probability failure of the corroded beam, the sensitivity analysis is conducted by considering
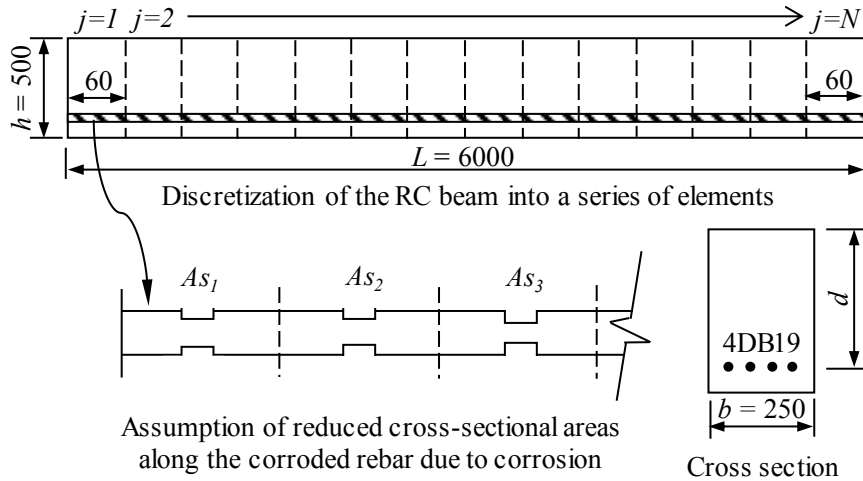
Fig. 51 Configuration of the RC beam and its discretization of into a series of elements along the beam length.

Table 4 Statistics of Random Variables

Random variables	Design value	Mean	COV	Distribution
Cross Section A_S (cm^2)	11.34	-	-	Gumbel
Compressive strength f'_c (MPa)	38.04	45.27	0.10	Normal
Yield strength, f_y (MPa)	413.42	465.10	0.04	Normal
Effective depth, d (mm)	417	417	0.05	Normal
Uniform loading, Q (kN/m)	30	30	0.05	Lognormal

Note: COV = coefficient of variation
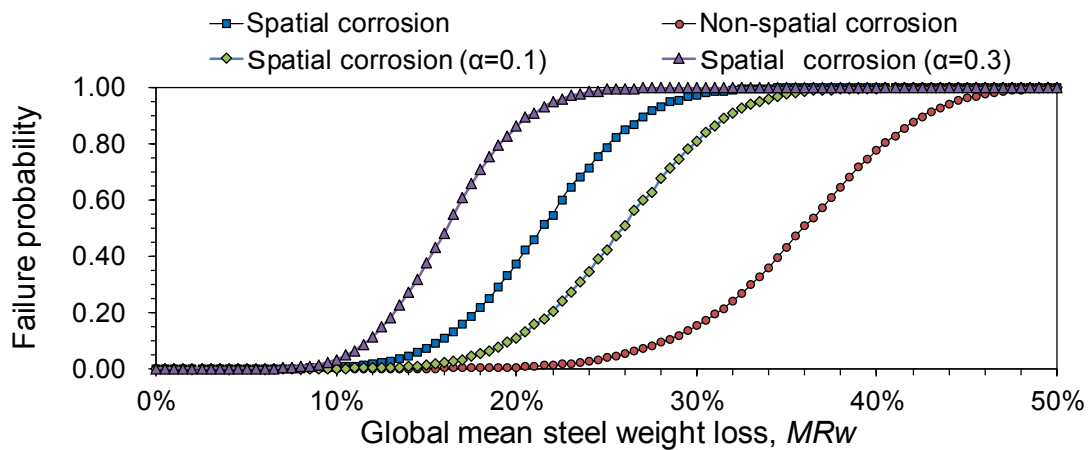
Fig. 52 Effect of the modeling of spatial distribution associated with the steel corrosion on the failure probability of the corroding RC beam.

the maximum value ($\alpha = 0.3$) and minimum value ($\alpha = 0.1$) of Gumbel scale parameter for the flexural capacity estimation of the corroded beams.

Therefore, the critical flexural performance function at any element for a given global average steel corrosion can be determined as:

$$g(MRw_i) = \min_{j=1,N}(M_{r,j}(MRw_i) - M_{s,j}(MRw_i))$$
(31)

where $M_{s,j}(MRw_i)$ and $M_{r,j}(MRw_i)$ are the bending moment caused by the loading and flexural resistance at the mid-point of any element j, respectively, which occur at a global average steel weight loss i.

Fig. 52 illustrates the effect of the modeling of spatial distribution associated with the steel corrosion on the reliability of the corroding RC beam. It can be seen that the failure probability of the corroding RC beam with the spatial variability of reduced steel cross-sectional areas over the beam is much higher than the other one with the non-spatial variability of reduced steel cross-sectional areas. This result indicates that an assumption of non-spatial steel corrosion (i.e., uniformly reduced steel cross-sectional areas over the beam length) is an oversimplification and it is necessary to consider the spatial variability associated with steel corrosion in the reliability assessment of corroding RC beams. Furthermore, the results from sensitivity analysis shows the changes in scale parameters in between 0.3 and 0.1 causes a big difference in the probability of failure. Therefore, it can be said that the scale parameter has a substantial effect on the probability failure of the corroded beam.

Chapter 6: Conclusions and future works

In this research, the effects of the spatial variability in the steel corrosion on the structural performances of five accelerated-corrosion RC beams have been experimentally investigated and discussed. Furthermore, an FE analysis method has been provided to simulate the structural responses of the corroded beams when considering two different inputs (i.e., uniform and non-uniform cross-sections along the reinforcement). The accuracy of the FE model is presented by comparing the numerical results of the flexural responses of the simulated beams to those of the test beams in the experimental study. Moreover, the relation of the Gumbel parameters and corrosion amounts established in this study can be used to produce the stochastic field associated with the steel corrosion in RC structures. This in turn can facilitate the life-cycle performance assessment and management of deteriorated RC structures (Thanapol et al. 2016; Akiyama et al. 2016; Akiyama et al. 2010) by incorporating the spatial variability of steel corrosion. The main conclusions are summarized as follows:

1) The rebar weight loss estimated by using the digital image analysis of X-ray photograms was found to be only 3% higher than that of the actual measured steel weight loss. This demonstrated the good accuracy of the present application of the X-ray technique for investigating the spatial growth of corroded rebars in RC members.

2) The distributions of the steel weight loss and crack width are spatially non-uniform, and their degree of non-uniformity significantly increases as the steel weight loss and corrosion cracking increases. The cause of this larger spatial variability might result from the greater contribution of the larger surface cracks to the increase of steel weight loss (i.e., the larger corrosion cracking allows the much higher chloride

concentration to penetrate through and reach the reinforcement more easily).

3) The maximum steel weight loss usually does not occur at the locations corresponding to the maximum crack width and often occurs close to the stirrups. Additionally, these locations vary depending on the mean steel weight loss.

4) A strong relationship was found between the standard deviations of the steel weight loss or crack width and the differences between their maximum and minimum values when the mean steel weight loss exceeded 5%. This relationship may allow the estimation of the variability between two points after data from the in situ inspection of steel corrosion are obtained.

5) Effect of W/C ratio on the increased steel weight loss is not obvious. Meanwhile, the crack width of the specimens with low W/C ratios increased faster than those with high W/C ratios.

6) The crack width and steel corrosion of the specimen without stirrups increased more quickly than those of specimens with stirrups. Increasing the number of stirrups slows the steel corrosion but accelerates the growth of the crack widths.

7) A comparison between the cracking patterns of corroded beams after the flexural bending test and their individual non-uniform distribution of the steel weight loss along the beam length reveals the primary localized cracks, which leads to the beam collapse occurring approximately at the local maxima of the steel weight loss. It can be inferred that the local damages of the corroded RC beams can be physically captured if the non-uniform steel weight loss along the reinforcement is adequately assessed.

8) For a small dispersion in the steel corrosion (i.e., with a standard deviation of steel

weight loss below approximately 4.5%), the experimental results suggest that the structural capacity of the corroded beams is governed by the corrosion levels (as specified by the mean steel weight loss) rather than the local dispersion in the steel cross-section loss.

9) As the dispersion in the steel cross-section loss increases, the influence of the pitting corrosion or the local variability in the steel cross-section loss on the structural capacity of the corroded beams becomes more significant than the corrosion level. However, with limited experimental data, it is difficult to specify the exact value of dispersion at which the pitting corrosion becomes the dominant parameter. Further experimental studies are required for additional verification.

10) The relationship between the Gumbel distribution parameters of the maximum steel weight loss ratio and the corrosion amounts has been established. This relationship can be used for modeling the spatial variability in the steel corrosion and incorporated with the probabilistic model to predict the long-term structural performance of corroded RC structures.

11) Both results from the FE and probabilistic methods suggest that an assumption of the non-spatial (uniform) steel corrosion is not conservative for the reliability assessment of corroding RC members, and it is necessary to consider the spatial steel corrosion when evaluating the life-cycle structural performance of corrosion-affected RC structures.

The limitations of the experimental, numerical, and probabilistic methods are provided herein; and some recommendations are also suggested for improvements in the future research. According to the previous studies (Cairns et al. 2005; Du et al. 2005; Zhu et al. 2013), the rebars affected by corrosion was reported to suffer a greater loss in its ductility rather than strength. Therefore, the experimental methods in the future shall be improved so that the deflection of the corroded beam can be measured until the beam

collapses, and the steel corrosion effect on ductility reduction of the corroded beams has to be addressed and quantified.

The statistical data of spatial variability associated with steel weight loss in this research is obtained from rebars that were corroded using acceleration-corrosion tests with a quite large impressed current density of 1000 μA/cm^2. This current density was selected in this study since the corrosion test of multiple beams must be completed within a time frame with a few corrosion devices. Moreover, the experiment also involves taking X-ray images and analyzing a large amount of data. It is reported the spatial variability of steel corrosion might become larger as the applied current density is increased. Therefore, more researches are needed for studying the effects of different current densities on the spatial variability of steel corrosion.

Furthermore, it has been reported in the literature that macro corrosion cell can occur in the RC structure in which corrosion of one bar might be influenced by the other neighboring bars. In this study, all RC beams were reinforced with only one bar. This feature of experiment allows an easy interpretation of the effect of corrosion on the cracking width. However, it has a limitation in that it does not take into account of the corrosion effect of other neighboring bars. Hence, experiments using RC beams or slabs with multiple rebars shall be further investigated in the future.

For the numerical FE method, the constitutive materials of concrete and bond were adopted from the previous studies (Kallias and Rafiq, 2010). Although this FE method is capable of providing good predicted results for the loading capacity, it overestimates the stiffness of the beam throughout all the damaging stages. It was verified in Kallias and Rafiq (2010) that this bond-slip model could be used to estimate the effect of bond deterioration on the decrease in stiffness of the corroded beam by comparing the flexural response of simulated beams by FE models to those of test corroded beams. However, it seems that although the bond-slip model that provided good estimation result

in comparison to the test beams of other experimental research it cannot give adequate accuracy for estimating the effect of bond damage for corroded beams in this research. Further FE computational studies are needed for refining the bond constitutive model in order to simulate bond deterioration effect more precisely.

For the reliability analysis of structural performance of corroding RC structures, the probabilistic method used herein only considers a simple cross-section analysis. It does not consider the bond deterioration between steel and concrete and damage of surrounding concrete due to corrosion. In the future research, the method of integrated approach using the FE numerical analysis and probabilistic method might be a good option for considering the effects spatial steel corrosion on the bond interface and damaged concrete.

References

ACI 211.1-91. Standard practice for selecting proportions for normal, heavyweight, and mass concrete. (Reapproved 2002).

Ahmad, S. (2003). Reinforcement corrosion in concrete structures, its monitoring and service life prediction—a review. *Cem Concr Com*; 25:459‑471.

Akiyama, M., and Frangopol, D.M. (2013). Estimation of steel weight loss due to corrosion in RC members used on digital image processing of X-ray photogram. In: Strauss A, Frangopol DM, Bergmeister K, editors. Proceedings of the third international symposium on life-cycle civil engineering; Life-cycle and sustainability of civil infrastructure systems. CRC Press/Balkema, Taylor & Francis Group plc, London; 885–1891.

Akiyama, M., and Frangopol, D.M. (2014). Long-term seismic performance of RC structures in an aggressive environment: emphasis on bridge piers. *Struct Infrastruct Eng*; 10(7):865–879.

Akiyama, M., Frangopol, D.M., and Takenaka, K. (2016). Reliability-based durability design and service life assessment of reinforced concrete deck slab of jetty structures. *Struct Infrastruct Eng*. http://dx.doi.org/10.1080/15732479.2016.1164725 [published online on 12 April].

Akiyama, M., Frangopol, D.M., and Yoshida, I. (2010). Time-dependent reliability analysis of existing RC structures in marine environment using hazard associated with airborne chlorides. *Eng Struct*; 32:3768–3779.

Akiyama, M., and Frangopol, D.M. (2014). Long-term seismic performance of RC structures in an aggressive environment: Emphasis on bridge piers. *Struct Infrastruct Eng*; 10:865–879.

Akiyama, M., Frangopol, D.M., and Yoshida, I. (2010). Time-dependent reliability analysis of existing RC structures in a marine environment using hazard associated with airborne chlorides. *Eng Struct*; 32:3768–3779.

Almusallam, A.A. (2001). Effect of degree of corrosion on the properties of reinforcing steel bars. *Constr Build Mater*; 15:361–368.

Alonso, C., Andrade, C., and Gonzales, J.A. (1988). Relation between resistivity and corrosion rate of reinforcements in carbonated mortar made with several cement types. *Cem Concr Res*; 18:687–698.

Alonso, C., Rodriguez, J., and Diez, J.M. (1998). Factors controlling cracking of concrete affected by reinforcement corrosion. *Mater Struct*; 31:435–441.

Al-Sulaimani, G.J., Kaleemullah, M., Basunbul, I.A., and Rasheeduzzafar. (1990). Influence of corrosion and cracking on bond behaviour and strength of reinforced concrete members. *ACI Struct J*; 87(2):220–231.

Andrade, C., Alonso, C., and Molina, F.J. (1993). Cover cracking as a function of bar corrosion: Part I – Experimental test. *Mater Struct*; 26:453–464.

Angst, U. Chloride induced reinforcement corrosion in concrete: Concept of critical chloride content – methods and mechanisms. Ph.D. thesis; 2011.

Angst, U.M., Elsener, B., Larsen, C.K., and Vennesland, Ø. (2011). Chloride induced reinforcement corrosion: Electrochemical monitoring of initiation stage and chloride threshold values. *Corros Sci*; 5:1451–1464.

Ann, K.Y., and Song, H.-W. (2007). Chloride threshold level for corrosion of steel in concrete. *Corros Sci*; 49:4113–4133.

ASCE (2013). 2013 report card for America's infrastructure. Retrieved on Jan 28, 2016 from http://www.infrastructurereportcard.org.

Auyeung, Y., Balaguru, P., and Chung, L. (2000). Bond behaviour of corroded reinforcement bars. *ACI Mater J*; 97(2):214–220.

Azad, A.K., Ahmad, S., and Azher, S.A. (2007). Residual Strength of Corrosion-Damaged Reinforced Concrete Members. *ACI Mater. J.*, 104(1), 42–47.

Beck, M., Goebbels, J., Burkert, A., Isecke, B., and Babler, R. (2010). Monitoring of corrosion processes in chloride contaminated mortar by electrochemical measurement and X-ray tomography. *Mater Corros*; 61:475–479.

Bertolini, L. (2008). Steel corrosion and service life of reinforced concrete structures. *Struct Infrastruct Eng*; 4(2):123–137.

Cabrera, J.G. (1996). Deterioration of concrete due to reinforcement steel corrosion. *Cem Concr Com*; 18:47–59.

Cairns, J., Plizzari, G.A., Du, Y.G., Law, D.W., and Franzoni, C. (2005). Mechanical Properties of Corrosion-Damaged Reinforcement. *ACI Mater J*; 102(4): 256–264.

Castel, A., Francois, R., and Arliguie, G. (2000a). Mechanical behavior of corroded reinforced concrete beams-Part 1: Experimental study of corroded beams. *Mater Struct*; 33:539–544.

Castel, A., Francois, R., and Arliguie, G. (2000b). Mechanical behavior of corroded reinforced concrete beams-Part 2: Bond and notch effects. *Mater Struct*; 33:545–551.

CEB-FIP model code 1990. Bulletin d'Information 213/214. Lausanne (Switzerland); 1993.

Committee on Cost of Corrosion in Japan. Survey of corrosion cost in Japan. Japan Society of Corrosion Engineering and Japan Association of Corrosion Control, Tokyo 1997; 1–33.

Coronelli, D., and Gambarova, P. (2004). Structural assessment of corroded reinforced concrete beams: modelling guidelines. *J Struct Eng, ASCE*; 130(8):1214–1224.

Diamond, S. (2004). The microstructure of cement paste and concrete—a visual primer. *Cem Concr Com*; 26:919-933.

Du, Y.G., Clark, L.A., and Chan, A.H.C. (2005). Effect of corrosion on ductility of reinforcing bars. *Mag Concr Res*; 57(7):407–419.

Du, Y.G., Clark, L.A., and Chan, A.H.C. (2005). Residual capacity of corroded reinforcing bars. *Mag Concr Res*; 57(3):135–147.

Du, Y.G., Clark, L.A., and Chan, A.H.C. (2007). Impact of reinforcement corrosion on ductile behaviour of reinforced concrete beams. *ACI Struct J*; 104(3):285–293.

Duffó, G.S., Reinoso, M., Ramos, C.P., and Farina, S.B. (2012). Characterization of steel rebars embedded in a 70-year old concrete structure. *Cem Concr Res*; 42:111–117.

Fang, C., Lundgren, K., Chen, L., and Zhu, C. (2004). Corrosion influence on bond in reinforced concrete. *Cem Concr Res*; 34(11):2159–2167.

Fang, C., Lundgren, K., Plos, M., and Gylltoft, K. (2006). Bond behaviour of corroded reinforcing steel bars in concrete. *Cem Concr Res*; 36(10): 1931–1938.

Fazio, R. and Mirza, M.S. (1999). In-situ assessment of corrosion induced damage of the Dickson bridge deck. In: Lacasse MA, Vanier DJ, editors. Proceedings of the eighth international conference on durability of building materials and components; Service life and durability of materials and components. Canada: NRC Research Press:269–279.

Federal Highway Administration (FHWA) (2002). Corrosion cost and preventive strategies in the United States. FHWA-RD-01-156, U.S. Dept. of Transportation, McLean, VA.

Frangopol, D.M. (2011). Life-cycle performance, management, and optimisation of structural systems under uncertainty: accomplishments and challenges. *Struct Infrastruct Eng*; 7(6):389–413.

Glass, G.K., and Buenfeld, N.R. (1997). The presentation of the chloride threshold level for corrosion of steel in concrete. *Corros Sci*; 5(39):1001–1013.

Gonzalez, J.A., Andrade, C., Alonso, C., and Feliu, S. (1995). Comparison of rates of general corrosion and maximum pitting penetration on concrete embedded steel reinforcement. *Cem Concr Res*; 25(2): 257–264.

Heiyantuduwa1, R., Alexander, M.G., and Mackechnie, J.R. (2006). Performance of a penetrating corrosion inhibitor in concrete affected by carbonation-induced corrosion. *J Mater Civ Eng*; 18(6): 842–850.

Kallias, A.N., and Rafiq M.I. (2010). Finite element investigation of the structural response of corroded RC beams. *Eng Struct*; 32:2984–2994.

Kanno, R. (2016). Advances in steel materials for innovative and elegant steel structures in Japan—A review. *Struc Eng Inter*; 26(3):242-253.

Kashani, M.M., Crewe, A.J., and Alexander, N.A. (2013a). Nonlinear stress–strain behaviour of corrosion-damaged reinforcing bars including inelastic buckling. *Eng Struct*; 48:417–429.

Kashani, M.M., Crewe, A.J., and Alexander, N.A. (2013b). Use of a 3D optical measurement technique for stochastic corrosion pattern analysis of reinforcing bars subjected to accelerated corrosion. *Corros Sci*; 73:208–221.

Lee, H.S., Kage, T., Noguchi, T., and Tomosawa, F. (1999). The evaluation of flexural strength of RC beams damaged by rebar corrosion. In: Lacasse MA, Vanier DJ, editors. Proceedings of the eighth international conference on durability of building materials and components; Service life and durability of materials and components. Canada: NRC Research Press:320–330.

Lim, S., Akiyama, M., Frangopol, D.M., and Jiang, H. (2017). Experimental investigation of the spatial variability of the steel weight loss and corrosion cracking of RC members: Novel X-ray and digital image processing techniques. *Struct Infrastruct Eng*; 13(1):118–134.

Lim, S., Akiyama, M., and Frangopol, D.M. (2016). Assessment of the structural performance of corrosion-affected RC members based on experimental study and probabilistic modeling. *Eng Struct*; 127:189–205.

Lundgren, K. (2007). Effect of corrosion on the bond between steel and concrete: an overview. *Mag Concr Res*; 59(6):447–461.

Maaddawy, T.E., Soudki, K., and Topper, T. (2005). Analytical model to predict nonlinear flexural behaviour of corroded reinforced concrete beams. *ACI Struct J*; 102: 550–509.

Marsh, P.S., and Frangopol D.M. (2008). Reinforced concrete bridge deck reliability model incorporating temporal and spatial variations of probabilistic corrosion rate sensor data. *Reliab Eng Syst Saf*; 93(3):394–409.

Marsh, P.S., and Frangopol, D.M. (2008). Reinforced concrete bridge deck reliability model incorporating temporal and spatial variations of probabilistic corrosion rate sensor data. *Reliab Eng Syst Saf;* 93: 394–409.

Media Cybernetics, Inc. Image-Pro Plus version 7.0 for Windows, start-up guide. Rockville, MD: Media Cybernetics; 2012.

Mehta, P.K., and Monteiro P.J.M. Concrete: microstructure, properties, and materials. McGraw-Hill Companies, Inc; 2006.

Molina, F.J., Alonso, C., and Andrade, C. (1993). Cover cracking as a function of rebar corrosion: part 2–Numerical model. *Mater Struct*; 26:532–548.

Mori, Y., and Ellingwood, B.R. (1993). Reliability-based service life assessment of aging concrete structures. *J Struct Eng*; 119(5):1600–1621.

Nakamura, H., and Higai, T. (2001). Compressive fracture energy and fracture zone length of concrete. In: Shing P, Tanabe T, editors. Modelling of inelastic behaviour of RC structures under seismic loads. American Society of Civil Engineering; 471–487.

Ollivier, J.P., Maso, J.C., and Bourdette, B. (1995). Interficial transition zone in concrete. *Advn Cem Bas Mat*; 2:30–38.

Page, C.L. (1975). Mechanism of corrosion protection in reinforced concrete marine structures. *Nature*; 258:514–515.

Page, C.L., and Treadaway, K.W.J. (1982). Aspects of the electrochemistry of steel in concrete. *Nature*; 297:109–116.

Palsson, R., and Mirza, M.S. (2002). Mechanical response of corroded steel reinforcement of abandoned concrete bridge. *ACI Struct J*; 99(2):157–162.

Papadakis, V.G., Vayenas, C.G., and Fardis, M.N. (1989). A reaction engineering approach to the problem of concrete carbonation. *AIChE J.*; 35(10):1639–1650.

Rodriguez, J., Ortega, L.M., and Casal, J. (1997). Load carrying capacity of concrete structures with corroded reinforcement. *Constr Build Mater*; 11(4):239–248.

Scrivener, K.L. (2004). Backscattered electron imaging of cementitious microstructures: understanding and quantification. *Cem Concr Com*; 26(8): 935–945.

Shimomura, T., Shigehiko, S., Ryosuke, T., and Akihiro, S. (2011). Modelling and nonlinear FE analysis of deteriorated existing concrete structures based on inspection. In: Andrade C, Mancini G, editors. Proceedings of the Joint fib-RILEM Work-shop; Modelling of corroding concrete structures. Springer Dordrecht Heidelberg London New York: RILEM book series; 5:281-304.

Smith, J.C. Structural Steel Design: LRFD approach. Canada: John Willey & Sons, Inc.; 1996.

Stewart, M.G. (2004). Spatial variability of pitting corrosion and its influence on structural fragility and reliability of RC beams in flexure. *Struct Saf*; 26:453–470.

Stewart, M.G. (2009). Mechanical behaviour of pitting corrosion of flexural and shear reinforcement and its effect on structural reliability of corroding beams. *Struct Saf*; 31:19–30.

Stewart, M.G., and Al-Harthy, A. (2008). Pitting corrosion and structural reliability of corroding RC structures: experimental data and probabilistic analysis. *Reliab Eng Syst Safety*; 93(3):373–382.

Stewart, M.G., and Mullard, J.A. (2007). Spatial time-dependent reliability analysis of corrosion damage and the timing of first repair for RC structures. *Eng Struct*; 29(6): 1457–1464.

Stewart, M.G., and Suo, Q. (2009). Extent of spatially variable corrosion damage as an indicator of strength and time-dependent reliability of RC beams. *Eng Struct*; 31:198–207.

Suda, K., Misra, S., and Motohashi, K. (1993). Corrosion products of reinforcing bars embedded in concrete. *Corros Sci*; 35:1543–1549.

Sæther, I. (2011). Bond deterioration of corroded steel bars in concrete. *Struct Infrastruct Eng*; 7(6):415–429.

Thanapol, Y., Akiyama, M., and Frangopol, D.M. (2016). Updating the seismic reliability of existing RC structures in a marine environment by incorporating the spatial steel corrosion distribution: application to bridge piers. *J Bridge Eng*; 21(7):04016031-1–04016031-17.

TNO. DIANA Finite Element Analysis, User's Manual release 9.5. The Netherlands: TNO DIANA BV, 2014.

Torres-Acosta A.A., Navarro-Gutierrez S., and Teran-Guillen J. (2007). Residual flexure capacity of corroded reinforced concrete beams. *Eng Struct*; 29:1145–1152.

U.S. Bureau of Reclamation. A manual for control of construction. Wasington: United States Government Printing Office; 1975.

Val, D.V. (2007). Deterioration of strength of RC beams due to corrosion and its influence on beam reliability. *J Struct Eng*; 133(9):1297–306.

Vidal, T., Castel, A., and Francois, R. (2004). Analyzing crack width to predict corrosion in reinforced concrete. *Cem Concr Res*; 34:165–174.

Watanabe, E., Furuta, H., Yamaguchi, T., and Kano, M. (2014). On longevity and monitoring technologies of bridges: a survey study by the Japanese Society of Steel Construction. *Struct Infrastruct Eng*; 10(4):471–491.

Yamamoto, T., Oyado, M., Mikata, Y., Kobayashi, K., and Shimomura, T. (2011). Systematic laboratory test on structural performance of corroded reinforced concrete and its utilization in practice. In: An-drade C, Mancini G, editors. Proceedings of the Joint fib-RILEM Work-shop; Modelling of corroding concrete structures. Springer Dordrecht Heidelberg London New York: RILEM book ; 5:113-124.

Zhang, W., Dai, H., Gu, X., and Wu, S. (2010). Effects of corrosion pits on mechanical properties of corroded steel bars. *Earth and Space*; 3504–3511. doi: 10.1061/41096(366)334.

Zhang, W., Zhou, B., Gu, X., and Dai, H. (2014). Probability Distribution model for cross-sectional area of corroded reinforcing steel bars. *J Mater Civ Eng*; 26(5):822–832. doi: 10.1061/(ASCE)MT.1943-5533.0000888.

Zhao, Y., Ren, H., Dai, H., and Jin, W. (2011). Composition and expansion coefficient of rust based on X-ray diffraction and thermal analysis. *Corros Sci*; 53:1646–1658.

Zhou, Y., Gencturk, B., Willam, K., and Attar, A. (2015). Carbonation-induced and chloride-induced corrosion in reinforced concrete structures. *J Mater Civ Eng*; 27(9):040142451-17. doi:10.1061/(ASCE)MT.1943-5533.0001209.

List of Published Papers

Academic papers:

Sopokhem Lim, Mitsuyoshi Akiyama, and Dan M. Frangopol. Assessment of the structural performance of corrosion-affected RC members based on experimental study and probabilistic modeling. *Engineering Structures*, 2016; 127:189–205.

Sopokhem Lim, Mitsuyoshi Akiyama, Dan M. Frangopol, and Haitao Jiang. Experimental investigation of the spatial variability of the steel weight loss and corrosion cracking of RC members: Novel X-ray and digital image processing techniques. *Structure and Infrastructure Engineering*, 2017;13(1):118–134.

Sopokhem Lim, Mitsuhiro Matsuda, Ramiz Ahmed Raju, and Mitsuyoshi Akiyama. Flexural behavior prediction of SFRC beams using finite element method and X-ray image. *Proceedings of the Japan Concrete Institute*, 2017; 39(2):1099–1104.

Sopokhem Lim, Takehiro Okamoto, Mitsuhiro Matsuda, and Mitsuyoshi Akiyama. Flexural behavior prediction of SFRC beams: a novel X-ray technique. *Proceedings of the Japan Concrete Institute*, 2016; 38(2):1351–1356.

Sopokhem Lim, Haitao Jiang, Takehiro Okamoto, and Mitsuyoshi Akiyama. Visualization of corroded steel bars in RC beams using digital image processing of X-ray photograms. *Proceedings of the Japan Concrete Institute*, 2015; 37(2):1327–1332.

松田充弘，岡本健弘，Lim Sopokhem，秋山充良：鋼繊維の X 線撮影結果を用いた SFRC はりの曲げ挙動解析に関する基礎的研究，構造工学論文集, 2017; 63A: 847–858.

Conference papers (peer review):

Sopokhem Lim, Huijuan Song, Lei Nie, and Mitsuyoshi Akiyama. Structural performance assessment of aging RC beams considering the spatial variability of steel corrosion: experimental study and probabilistic model. *The Fifteenth East Asia-Pacific on Structural Engineering and Construction Conference* (*EASEC-15*); Oct. 2017, Xi'an, China.

Sopokhem Lim, Huijuan Song, Lei Nie, and Mitsuyoshi Akiyama. Effect of spatial variability associated with steel corrosion on the reliability of corroded RC beams. *The 8th Asia and Pacific Young Researchers and Graduates Symposium* (*YRGS2017*); Sept. 2017, Tokyo, Japan.

Sopokhem Lim, Mitsuyoshi Akiyama, and Dan M. Frangopol. Assessment of the structural behavior of corrosion-affected RC beams: Experimental study and modeling. *Proceedings of the Fifth International Symposium on the Life-Cycle Engineering* (*IALCCE2016*); 379–384, Sept. 2016, Delft, the Netherlands.

Sopokhem Lim, Haitao Jiang, and Mitsuyoshi Akiyama. Investigation of the spatial variability of steel weight loss and corrosion cracking: A novel X-ray technique. *Proceedings of the Fifth International Conference on Durability of Concrete Structures* (*ICDCS2016*); 265–269, June 2016, Shenzhen, China.

Sopokhem Lim, Takehiro Okamoto, and Mitsuyoshi Akiyama. Flexural behavior prediction of SFRC beams using X-ray photograms. *The Fourteenth East Asia-Pacific on Structural Engineering and Construction Conference (EASEC-14)*; 1254–1257, Jan. 2016, Ho Chi Min, Vietnam.

Sopokhem Lim, Haitao Jiang, Mitsuyoshi Akiyama, and Dan M. Frangopol. Experimental investigation on the relationship between the spatial variation of steel weight loss and the cracking width of RC members using X-ray photograms. *Proceedings of the Fourth International Symposium on Life-Cycle Civil Engineering (IALLCCE2014)*; 429–436, Nov. 2014, Tokyo, Japan.

Conference papers (non-peer review):

Sopokhem Lim, Ramiz Ahmed Raju, Mitsuhiro Matsuda, and Mitsuyoshi Akiyama. Pediction method of SFRC beams in bending using FE analysis and X-ray images. *72nd Japan Society of Civil Engineers 2017 Annual Meeting*; Sept. 2017; Fukuoka, Japan.

Sopokhem Lim, Takehiro Okamoto, Mitsuhiro Matsuda, and Mitsuyoshi Akiyama. Flexural behavior prediction of SFRC beams using X-ray images and FEM analysis. *71th Japan Society of Civil Engineers 2016 Annual Meeting*; Sept. 2016, Sendai, Japan.

Sopokhem Lim, Takehiro Okamoto, and Mitsuyoshi Akiyama. Estimation of flexural post

cracking behavior of SFRC beams using X-ray photograms. *70th Japan Society of Civil Engineers 2015 Annual Meeting*; Sept. 2015, Okayama, Japan.

Sopokhem Lim, Takehiro Okamoto, Mitsuyoshi Akiyama, and Atsuchi Koizumi. Correlation between fiber density distribution and flexural capacity of SFRC beams using optical density analysis of X-ray image. *69th Japan Society of Civil Engineers 2014 Annual Meeting*; Sept. 2014, Osaka, Japan.